SURFACE STRAIN BEHAVIOR OF 18650 CYLINDRICAL LITHIUM-ION BATTERIES UNDER NORMAL AND OVERCHARGE CYCLING: EXPERIMENTS AND FINITE ELEMENT ANALYSIS

Ву

Igor Igorevich Bezsonov

A DISSERTATION

Submitted to
Michigan State University
in partial fulfillment of the requirements
for the degree of

Mechanical Engineering – Doctor of Philosophy

2024

ABSTRACT

Modern technology, from portable electronics to electric vehicles, is becoming increasingly reliant on lithium-ion (Li-ion) batteries for energy storage. This chemistry possesses a desirable combination of high power and high energy densities and is therefore widely used, but safety is still a significant issue. The risk of thermal runaway (TR) is a major roadblock to the widespread use of this technology. TR is a self-sustaining exothermic reaction which can be triggered by mechanical or electrical damage to a cell, overheating, or by latent defects from manufacturing. The volumetric changes within a cell's electrodes and internal gas generation can be detected by strain measurements on the surface of the casing, which can complement the electrical and thermal data used by battery management systems (BMS) and even provide insight into the state of a battery when electrical contact has been lost. This research project demonstrates the utility of strain measurements to detect abnormal Li-ion cell behavior and precursors to TR. First, a baseline was established to identify the strain response of Li-ion cells under normal operating conditions, accounting for temperature and cycling rate (or C-rate) effects. Then, the cells were cycled under abuse conditions to identify signs of damage and identify signs of TR onset through strain measurements. The final step was to develop a model which used fundamental data and electrochemical input to predict the mechanical behavior of individual electrodes and full 18650 cells.

The samples used in this research were commercial 18650 format (18 mm in diameter, 65 mm tall) cylindrical cells with graphite-silicon anodes and nickel cobalt aluminum oxide (NCA) cathodes. Strain data was collected using strain gages bonded to the cell casing and was used to characterize their mechanical behavior during both normal and abuse cycling conditions. During a charge-discharge cycle at normal conditions, the surface strain was found to be nearly reversible – that is, the strain states at the beginning of charge and the end of discharge were almost the same. The strain profile of the cells was analyzed and found to be directly related to electrochemical reactions occurring within the electrodes, as evidenced by dQ/dV and d ϵ /dV plots. The fact that the d ϵ /dV peaks coincide with – and sometimes precede – the peaks in the dQ/dV plots shows that the electrochemical reactions occurring within the electrodes during charge and discharge can be sensed through strain measurements on the surfaces of cell casings.

With the baseline established, cells were then subjected to several abuse scenarios. During the first abuse scenario cells were overcharged to failure, which came in the form of current interrupt device (CID) activation. During overcharge (past 4.2V) the cell potential was seen to increase quickly and reached a plateau at approximately 5V, shortly after which the CID activated, and the cell became electrically inaccessible (0V). The cells' surface strain also increased dramatically during this abuse scenario, reaching a value that was more than double the peak strain during normal cycling. The CID-activated cells were then heated to TR, during which two events were identified from the strain signature as signs/precursors to TR which could be used for prediction and prevention purposes. Cells were also repeatedly overcharged to 105% and 110% nominal capacity, named 5% and 10% overcharge (OC), respectively. Maximum strain, potential, and temperature were seen to increase slowly during the 5% OC experiments, and quickly during 10% OC, during which the CID activated after an average of 11 cycles. Strain at full discharge (referred to as residual strain) reached a progressively higher value after each OC cycle and was found to closely correlate to the pressure needed to activate the CID. Electrochemical impedance spectroscopy, dQ/dV, and dɛ/dV analyses confirmed that the degradation modes present were mostly caused by loss of lithium inventory processes. The insights gained from stress measurement, including the ability to predict CID activation, are discussed.

A finite element analysis modeling approach to predict the mechanical behavior of individual electrodes and full cells was developed. Electrochemistry was solved in COMSOL Multiphysics using a pseudo 4-dimensional (P4D) model to predict the cell potential and the state of charge of the active material within electrodes. Mechanics were coupled to electrochemistry through volumetric changes of the active material and a thermal strain analogy. The effective mechanical properties of the electrodes were calculated using the Mori-Tanaka homogenization scheme, with the development and assumptions explained fully in this work. The homogenized properties were compared to experimental and published results and were found to be in good agreement. Simulations for stress in graphite anode and nickel manganese cobalt oxide cathode were in agreement with published data. Predictions were also made for graphite-silicon anodes and NMC cathode and a geometry representative of an 18650 format battery. The limitations and future improvements for this model are discussed.

Copyright by IGOR IGOREVICH BEZSONOV 2024

This dissertation is dedicated to my amazing wife, Yiran Li.
Thank you for all your love and support.

ACKNOWLEDGEMENTS

I would like to thank my advisor, Professor Siva Nadimpalli, for the substantial support and guidance during my graduate school career. I am also grateful to my Navy mentors, Dr. Gordon Waller and Dr. Jonathan Ko, who have also provided their valuable expertise and insights.

This research was sponsored by the Office of Naval Research and was accomplished under Grant Number N00014-21-1-2499. The views and conclusions contained in this document are those of the author and should not be interpreted as representing the official policies, either expressed or implied, of the Office of Naval Research or the U.S. Government.

TABLE OF CONTENTS

LIST OF TABLES	ix
LIST OF FIGURES	x
LIST OF SYMBOLS	xiv
LIST OF ABBREVIATIONS	xix
CHAPTER 1: INTRODUCTION	1
1.1: History of Lithium-ion Battery Components	1
1.2: Thermal Runaway of Lithium-Ion Batteries	5
1.3: Strain Measurements for Battery Health Monitoring and Thermal Runaway Prevention	7
1.4: Cell Degradation During Repeated Overcharge and Strain	
1.5: Electrochemical Modeling and Mechanical Predictions	
1.6: Objectives of the Dissertation	
1.0. Objectives of the Dissertation	10
CHAPTER 2: BASELINE STRAIN BEHAVIOR	12
2.1: Experimental Setup for Baseline Strain Measurements	12
2.2: Electrochemical Cycling Procedure	
2.3: Electrode Characterization	16
2.4: Electrode Strain Measurements	20
2.5: Differential Capacity Analysis	27
2.6: Effects of C-Rate on Cell Behavior	30
CHAPTER 3: STRAIN BEHAVIOR DURING OVERCHARGE AND HEATING TO THERMAL	
RUNAWAY	34
3.1: Overcharge to CID Activation Experiments	34
3.2: Repeated Overcharge Experiments	41
CHAPTER 4: BATTERY MODELING AND SIMULATIONS	56
4.1: Electrochemical Model	56
4.2: Mori-Tanaka (M-T) Homogenization Scheme with Eshelby Formulation	59
4.3: Application of M-T Homogenization to Composite Electrodes	72
4.4: Volumetric Expansion of Active Material and Porosity Reduction	77
4.5: COMSOL Finite Element Analysis (FEA) Setup	81
4.6: Simulations Results and Comparison to Published Data	85
CHAPTER 5: CONCLUSION	91
5.1: Baseline Strain Behavior	91
5.2: Strain Behavior During Overcharge	
5.3: Battery Modeling and Simulations	94
F. A. Futuro Work	ΩE

BIBLIOGRAPHY	98
APPENDIX A: ELECTRODE STRESS MEASUREMENTS	110
APPENDIX B: ANALYTICAL MODELING EFFORTS	121

LIST OF TABLES

Table 1: EDS spectrum of anode, averaged over 3 locations
Table 2: EDS spectrum of cathode, averaged over 3 locations
Table 3: Maximum strain locations at various cell discharge rates and corresponding temperatures
Table 4: Strain and temperature points of interest during thermal runaway experiments 40
Table 5: Strain comparison between baseline and the first overcharge cycle
Table 6: 10% OC test results for all 4 samples
Table 7: Estimated parameters for the equivalent circuit model
Table 8: Elastic properties of active materials
Table 9: Volume fractions of composite electrode constituents
Table 10: Comparison of effective elastic properties calculated using M-T homogenization with experimental and published results
Table 11: Variables used for COMSOL simulation
Table 12: Half-cell layer thicknesses
Table 13: Details of the tested 18650 cell parameters, as measured from the CT images 84
Table 14: Material properties and thicknesses of battery electrode samples 115

LIST OF FIGURES

Figure 1: Schematic of (a) a cylindrical battery [1] and (b) a full cell
Figure 2: Approximate ranges of average discharge potentials and specific capacities of (a) intercalation-type cathodes and (b) conversion-type anodes [6]
Figure 3: Photos and CAD model of battery cap from literature [10], CT scan image of battery cap from a sample
Figure 4: (a) Nyquist plot showing the components of a usual EIS data set from a Li-ion battery and (b) the DMs associated with the changes in each arc/region of the EIS spectrum [58] 8
Figure 5: Schematic of strain measurement and battery cycling setup
Figure 6: (a) Schematic of an instrumented cell and (b) a picture of a cell instrumented with strain gages and a thermocouple in a cell holder
Figure 7: CT cross-section images of the 18650 cylindrical cell showing (a) side (full cell), (b) side (zoomed-in), and (c) top views
Figure 8: The EDS analysis of (a) the negative electrode confirms the presence of silicon (in yellow), and in (b) the positive electrode the presence of nickel (in yellow)
Figure 9: Strain drift during a 7-day period
Figure 10: Middle hoop strain during thermal cycling at 0, 50, and 100% SoC as (a) strain and temperature vs. time and (b) strain vs. temperature
Figure 11: Strain measurement from all three rosettes (i.e., the three gages shown in Figure 6) during three C/5 cycles
Figure 12: (a) Strain measurement from all three rosettes (i.e., the three gages shown in Figure 6) during three C/5 cycles. (b) The hoop strain signal (from Gage 2) for several cycles is plotted showing how it evolves with cycles before reaching steady state behavior. (c) Cycle efficiency, discharge capacity, and maximum strain during a given cycle is plotted as a function of cycle number
Figure 13: a) Strain, potential, and temperature vs. time during a typical C/10 charge/discharge cycle with a 2 hr rest step in between, b) strain and potential vs. time for 3 cycles showing consistent cycling behavior
Figure 14: Typical strain (normalized with the peak strain at 100% SoC) response during a C/5 charge/discharge cycle from three different cells confirming that the strain signature observed is a function of anode and cathode chemistry and electrode and cell fabrication/processing parameters

Figure 15: Differential capacity (dQ/dV) and strain vs. cell potential (V) during (a) charge and (b) discharge
Figure 16: Differential capacity (dQ/dV) and differential strain (dε/dV) vs. cell potential (V) during (a) charge and (b) discharge process
Figure 17: Strain (με) vs. cell potential (V) for discharge rate experiments during (a) charge and (b) discharge
Figure 18: Differential capacity (dQ/dV) vs. cell potential (V) for discharge rate experiments during (a) charge and (b) discharge
Figure 19: Differential strain (dɛ/dV) vs. cell potential (V) for discharge rate experiments during (a) charge and (b) discharge
Figure 20: Wiring schematic for bridge completion modules and strain gages
Figure 21: Strain and potential during a C/5 cycle for a cell at (a) MSU and (b) NSWC Carderock
Figure 22: Hoop strain (from Gage2), cell potential, and temperature behaviors during overcharge abuse test
Figure 23: Strain and temperature behavior of an overcharged cell during heating to thermal runaway
Figure 24: Equivalent circuit model of a cell
Figure 25: Hoop strain (compensated to transverse effects), temperature change, and cell potential during galvanostatic cycling with (a) normal 4.2V cutoff, and (b) 5% OC cutoff 45
Figure 26: Hoop strain (compensated to transverse effects), temperature change, and cell potential during galvanostatic cycling with (a) normal 4.2V cutoff, and (b) 10% OC cutoff. Both strain and potential reach a higher maximum value than during 5% OC
Figure 27: Hoop strain (compensated for transverse effects), temperature change, and potential during (a) repeated 5% OC and (b) repeated 10% OC cycling. Maximum potential, strain, and temperature change increase slightly during every 5% OC cycle, and significantly during every 10% OC cycle, with CID activation during the 9 th 10% OC cycle
Figure 28: (a) Hoop strain vs. time profile for each 10% OC cycle, showing a similar trend between cycles with a steady increase in magnitude. The residual strain at the end of each cycle is also seen to increase. (b) Maximum hoop strain, potential, and cycle efficiency for each 10% OC cycle, showing a steady increase in both maximum strain and potential, and a drastic decrease in cycle efficiency, especially after the 4 th cycle. The magenta "X" marks in both figures indicate the CID activation event, which occurred during the 10 th cycle for this sample

Figure 29: (a) Incremental capacity analysis (ICA) showing dQ/dV peaks and (b) incremental strain analysis (ISA) plots show dɛ/dV peaks during the charge step for every 10% OC cycle. Both ICA and ISA show peak shifts towards a higher potential with an increasing cycle number
Figure 30: Electrochemical impedance spectra of a cell before OC cycling (pristine), after three, and six 10% OC cycles
Figure 31: EIS spectrum compared to a parameterized L-R-RC-RC-W circuit for a cell (a) before OC cycling (pristine), (b) after three 10% OC cycles, and (c) after six 10% OC cycles. A good agreement can be seen between the equivalent circuits and the obtained spectra
Figure 32: P2D model of an electrode from Jokar et al. [95]
Figure 33: Composite material homogenized into one with effective properties 60
Figure 34: RVE representing an infinite medium with an ellipsoidal inclusion
Figure 35: Homogenization RVE showing the inclusion region (Ω) and the matrix (V- Ω) 61
Figure 36: Secondary NMC active material particles with (top) randomly distributed primary particles and (bottom) aligned elongated particles by Park et al. [102]74
Figure 37: Graphite volume change as a function of lithium content from Schweidler et al. [93]
Figure 38: NCA volume change as a function of lithium content calculated using data from Robert et al. [113]
Figure 39: Volume change as a function of lithium content for various NMC chemistries from Iqbal et al. [114]
Figure 40: Assumed trend of 25% porosity reduction in a graphite anode
Figure 41: Volume change of a graphite anode with a 22% reduction in porosity
Figure 42: 2D Axissymmetric model of a half-cell.
Figure 43: Cell cross section from Nadimpalli et al. [31] and 2D axisymmetric COMSOL model with a mandrel at the cell's center and steel casing on the outside of the jellyroll
Figure 44: Experimental [31] and simulated cell potential for (a) graphite anode and (b) NMC cathode half cells
Figure 45: Experimental [30,31] and simulated anode stress response as a function of half-cell capacity.

Figure 46: Experimental [31] and simulated results for published NMC cathode stress compared with simulated (a) NMC111 and (b) NCA cathode stresses
Figure 47: Predicted strain on the surface of an 18650 cell for a graphite - NMC111 and graphite/Si – NCA chemistries, compared to measured strain
Figure 48: Electrode stress measurement sample
Figure 49: (a) Prepared cathode specimen with a current collector for electrical connection. (b) Schematic of the cathode specimen layers
Figure 50: Beaker cell CAD model with cutaway
Figure 51: Curvature measurement schematic with laser dot spacing
Figure 52: (a) Spot spacing and potential vs. time and (b) calculated stress and potential vs. time for graphite-silicon anodes from NEI
Figure 53: (a) Spot spacing and potential vs. time and (b) calculated stress and potential vs. time for graphite-silicon (5 wt.%) anodes from NEI
Figure 54: (a) Spot spacing and potential vs. time and (b) calculated stress and potential vs. time for graphite-silicon (20 wt.%) anodes from MTI
Figure 55: Stress recorded for an NMC811 sample during a CV
Figure 56: Stress recorded for an NCA sample during galvanostatic cycling
Figure 57: Schematic showing internal layers of a hollow 18650 cell, with electrodes approximated as concentric rings
Figure 58: Strain and potential vs. time during a usual C/10 cycle showing that the analytical model could predict an accurate stress response with stress data

LIST OF SYMBOLS

Å	Angstrom
α	Coefficient of thermal expansion
$lpha_{\text{e}}$	Specific surface area of the electrode
B_{pqkl}	Inverse of the localization tensor
°C	Degrees Celsius
Cs	Concentration of lithium in the electrode's solid phase
c _s max	Maximum Li+ concentration in electrode particle
c _s urf	Concentration of Li+ on a particle's surface
Ce	Concentration of lithium in the electrode's liquid (electrolyte) phase
C_{ijkl}	Stiffness tensor of the matrix material
C_{ijkl}^{Ω}	Stiffness tensor of the inclusion material
\overline{C}_{ijkl}	Effective stiffness tensor for the entire composite
Ds	Diffusion coefficient of Li ⁺ in the solid electrode phase
D_{eff}	Effective diffusion coefficient of Li ⁺ in the electrolyte phase
δ	Kronecker delta
Δ	Delta
∇	Nabla operator
dL	Change in length (thermal strain)
dV	Volume change
$dV_{\scriptscriptstyle AM}$	Change of the active material's volume
dV_{P}	Change of the porosity / void space volume
$dV_{\text{AM,Ma}}$	Maximum change of the active material's volume
dV	Maximum change of the norosity / void space volume

- Σ Summation
- E Young's modulus
- **E** Effective Young's modulus for the entire composite
- E₀ Young's modulus in the longitudinal direction
- E₉₀ Young's modulus in the transverse direction
- F Faraday's constant
- F_j Body force
- G Green's function
- h Half-cell component layer thickness
- I_a Applied current density
- I₁ First shape integral
- I_{II} Second shape integral
- II_{pqkl} Fourth order identity tensor
- J_{II} Third shape integral
- J Wall flux of Li⁺ on electrode particles
- Φ_s Potential of the electrode's solid phase
- Φ_e Potential of the electrode's liquid (electrolyte) phase
- φ Angle of reflectance
- ϕ^{α} Volume fraction of constituent α in the composite
- ϕ_{AM1} Volume fraction of the primary active material in the electrode
- ϕ_{AM2} Volume fraction of the additional active material in the electrode
- ϕ_B Volume fraction of the binder in the electrode
- ϕ_{CA} Volume fraction of the conductive additive in the electrode
- Φ_P Volume fraction of the porosity / void space in the electrode

Curvature of the silicon substrate Κ Bulk modulus of the matrix k k Effective bulk modulus for the entire composite \mathbf{k}^{Ω} Bulk modulus of the inclusion Reaction rate constant of electrode K_c K_b Transverse sensitivity in the hoop direction Effective ionic conductivity of electrolyte $\mathbf{k}_{\mathsf{eff}}$ Λ_{iikl}^{H} Hydrostatic component of the fourth order identity tensor Λ_{iikl}^{S} Shear component of the fourth order identity tensor M Mol Ω Volume of inclusion μ Shear modulus of the matrix $\bar{\mu}$ Effective shear modulus for the entire composite μ^{Ω} Shear modulus of the inclusion Overpotential of electrode μ_s Poisson's Ratio $\bar{\nu}$ Effective Poisson's Ratio for the entire composite Localization tensor P_H^{Ω} Hydrostatic component of the localization tensor P_S^{Ω} Shear component of the localization tensor R Universal gas constant R_1 Inclusion's radius in the 1 (x) direction

Inclusion's radius in the 2 (y) direction

Inclusion's radius in the 3 (z) direction

 R_2

R₃

$R_{\text{G,0}}$	Nominal strain gage resistance
σ	Stress
σ_{ij}	Stress in the composite
$\langle \sigma_{ij} \rangle$	Approximated stress tensor of the composite
σ_{eff}	Effective electric conductivity of the solid electrode phase
σ_{ij}^o	Defect-free (far field) stress
$\sigma_{ij}^{\boldsymbol{d}}$	Stress contribution of the inclusion
ε	Strain
ϵ_{ij}	Strain in the composite
$\langle \epsilon_{ij}^{\alpha} \rangle$	Approximated strain tensor of the constituent $\boldsymbol{\alpha}$ in the composite
$\langle \epsilon_{ij} \rangle$	Approximated strain tensor for the entire composite
ϵ_{kl}^{o}	Defect-free (far field) strain
ϵ_{kl}^{d}	Strain contribution of the inclusion
ϵ^{r}_{kl}	Eigenstrain
$\hat{\epsilon}_a$	Measured strain in the axial direction
$\boldsymbol{\hat{\epsilon}_b}$	Measured strain in the hoop direction
ϵ_{b}	Hoop strain compensated for transverse effects
ϵ_{p}	Electrode porosity
€ Therm	Strain due to a cell's temperature change
\mathbf{r}_{p}	Radius of an active material particle
$T_{ijkl}^{\Omega} \\$	Eshelby tensor
t.	Li ⁺ transference number in the electrolyte
U_{k}	Open circuit potential of electrode
	V 1

٧

Volume of RVE

 $V_{\text{\tiny cell}} \qquad \text{Voltage of cell}$

 Z_{Re} Resistance

 $Z_{\text{Img}} \qquad \text{Capacitance/Inductance}$

LIST OF ABBREVIATIONS

1D 1-Dimensional

3D 3-Dimensional

Ah Ampere-hour

Al Aluminum

AM Active Material

ARC Accelerating Rate Calorimetry

BCM Bridge Completion Module

BMS Battery Management System

CAD Computer Aided Design

C Carbon

CA Conductive Additive

CC Constant Current

CC-CV Constant Current - Constant Voltage

CID Current Interrupt Device

CMC Carboxymethyl Cellulose

CO Carbon monoxide

CT X-ray Computed Tomography

Cu Copper

CV Constant Voltage

DAQ Data Acquisition

DC Diethyl Carbonate

DM Degradation Mode

DMC Dimethyl Carbonate

EC Ethyl Carbonate

EDS Energy Dispersive x-ray Spectrometry

EIS Electrochemical Impedance Spectroscopy

F Fluoride

FEA Finite Element Analysis

Ge Germanium

GF Gage Factor

H₂ Hydrogen gas

H1 Hexagonal 1 (phase)

H2 Hexagonal 2 (phase)

H3 Hexagonal 3 (phase)

HF Hydrofluoric Acid

Hz Hertz

ICA Incremental Capacity Analysis

ISA Incremental Strain Analysis

ISC Internal Short Circuit

LAM Loss of Active Material

LCO Lithium Cobalt Oxide

LFP Lithium Iron Phosphate (LiFePO₄)

Li Lithium

LiPF₆ Lithium hexafluorophosphate

LLI Loss of Lithium Inventory

LoC Loss of Conductivity

M Monoclinic

MOS Multibeam Optical Sensor

MSU Michigan State University

M-T Mori-Tanaka

Mn Manganese

NCA Nickel Cobalt Aluminum

Ni Nickel

NI National Instruments

NMC Nickel Manganese Cobalt

NSWC Naval Surface Warfare Center

O Oxygen

OC Overcharge

OCP Open Circuit Potential

P Porosity

P2D Pseudo 2-Dimensional

P4D Pseudo 4-Dimensional

Pa Pascal

PAA Polyacrylic Acid

PC Personal Computer

PE Polyethylene

PP Polypropylene

PVdF Polyvinylidene (di)Fluoride

Q Capacity

RVE Representative Volume Element

SBR Styrene-Butadiene Rubber

SEI Solid Electrolyte Interphase

SEM Scanning Electron Microscope

Si Silicon

Sn Tin

SoC State of Charge

SS Stainless Steel

T Temperature

Ti Titanium

TJR Tenney Jr

TR Thermal Runaway

VI Virtual Instrument

XRD X-Ray Diffraction

CHAPTER 1: INTRODUCTION

1.1: History of Lithium-ion Battery Components

A battery is, essentially, an energy storage device. For more than a century, lead-acid was the go-to chemistry for batteries. However, as modern technology continues to develop, the demand for portable power sources with increasingly higher power and energy densities continues to increase. Lithium-ion chemistry possesses an unmatched combination of power and energy density, and therefore became the desirable choice to power portable electronics, power tools, electric vehicles, and more.

A common format for commercial lithium-ion batteries is a cylindrical 18650 size, in which the diameter is 18 mm, and the height is 65 mm. A schematic of a cylindrical cell is shown in Figure 1a below. Internally the cell consists of a jelly roll, which is a spiral structure comprised of the positive and negative electrodes, kept electrically insulated from one another by a separator. The entire jelly roll is wetted with an electrolyte which is ionically conductive but electrically insulative. The jellyroll consists of a series of "full cells," a schematic for which is shown in Figure 1b. In full cells both of the electrodes are composites, as compared to half cells where one of the electrodes is lithium metal.

Batteries utilize chemical reactions to store and release energy. During a discharge reaction, as shown in Figure 1b, lithium ions travel from the negative electrode (e.g., graphite) through the electrolyte and separator to the positive electrode (e.g., LiCoO₂). The electrons travel in the same direction, but through the current collectors and any loads within the electrical circuit. During charging of a battery, the process is similar but occurs in the opposite direction.

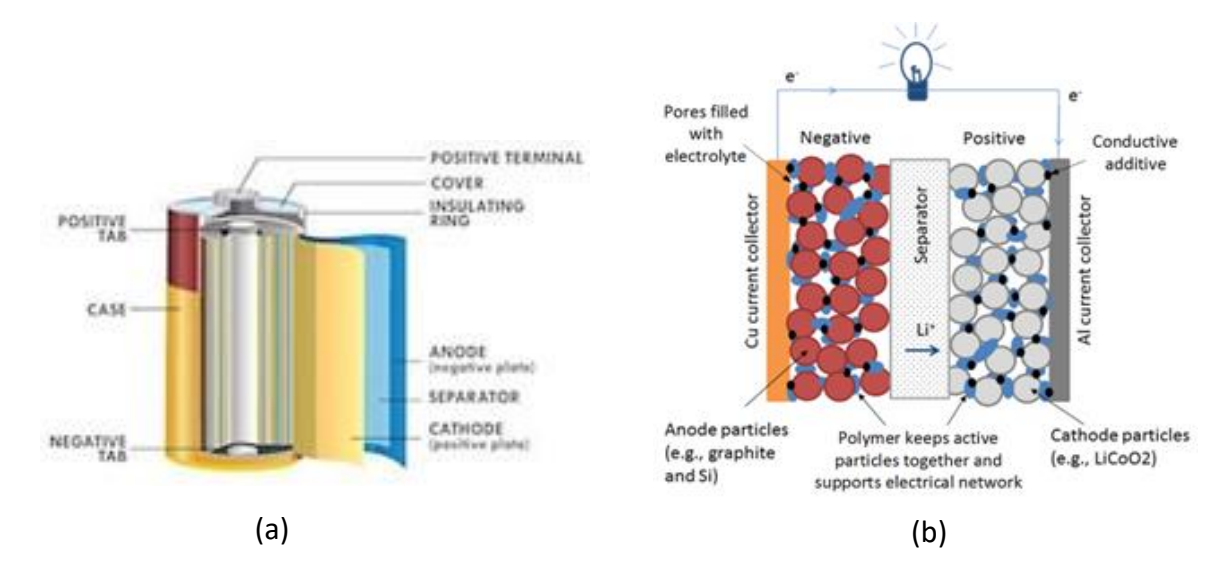


Figure 1: Schematic of (a) a cylindrical battery [1] and (b) a full cell.

The earliest Li-ion batteries used Li metal as their negative electrodes. This provided benefits such as low negative electrochemical potential (-3.040 V vs. standard hydrogen electrode) and a high theoretical capacity (3860 mA h g⁻¹). However, these early batteries suffered from low Coulombic efficiency and short cycle lives. Li metal electrodes grow dendrites – long branching structures – as the batteries undergo charge/discharge cycles, which leads to internal short circuits (ISC) and can cause thermal runaway (TR). Advances were made to slow this phenomenon and improve the feasibility of the Li metal electrode [2], but this technology has not been commercialized.

Since then, a variety of cathode and anode material combinations have evolved [3]. A brief summary of the usual electrode types found in commercial batteries is shown in Figure 2. Intercalation cathode materials, which store Li ions within their solid host network, are very widely used. Transition metal oxide cathodes are the most popular example of intercalation cathodes, with LiCoO₂ (LCO) still used in most commercial batteries today. Nickel and manganese-rich cathodes are gaining popularity as a more energy dense and thermally stable alternative to LCO. Various studies have examined LiNi_xMn_yCo₂O₂ compounds [4–6], focusing on xyz = 111, 442, 532, 541, 622, 811, and others. Polyanion compounds, such as LiFePO₄ (LFP), are used in some applications due to better thermal stability and high-power capability. Cathodes utilizing these active materials are less prone to dendrite growth under standard operating conditions, thereby reducing the chance of ISC due to dendrites.

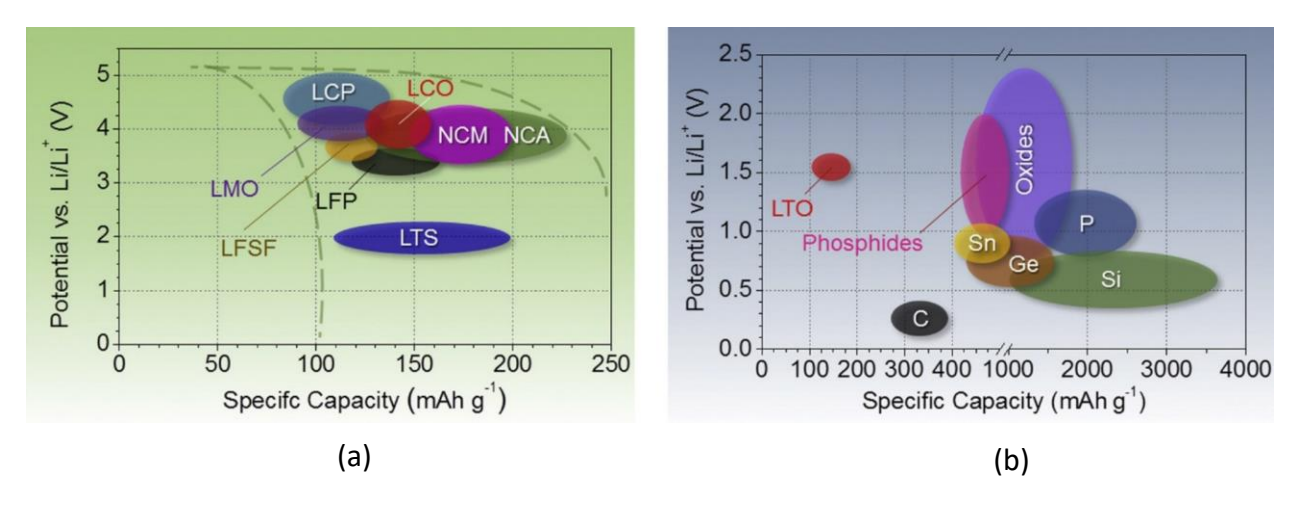


Figure 2: Approximate ranges of average discharge potentials and specific capacities of (a) intercalation-type cathodes and (b) conversion-type anodes [6].

Intercalation anodes, namely in the form of graphite as the active material, were used in commercial Li-ion batteries for over 20 years and are still a popular choice today. Graphite consists of graphene sheets, in which the carbon atoms form strong and stable bonds. This type of arrangement is beneficial for both electrical conductivity and Li transport [7]. Li ions intercalate between the graphene, with one Li atom being stored per six carbon atoms. The theoretical capacity of carbon anode material is low (372 mA h g⁻¹ and 330-430 mA h cm⁻³), which motivates the search for higher capacity active materials. Type B conversion anode materials, such as germanium (Ge) and silicon (Si) are alternatives with superior gravimetric and volumetric capacities – up to 10 times that of carbon materials. Instead of intercalating into inter-atomic sites, these materials form compounds with Li. However, these active materials suffer from short cyclic lives, as they tend to undergo high volume changes (up to 300% for Si), which cause fracture of the active material and solid electrolyte interphase (SEI) layer. This causes loss of electrical contact with the bulk electrode and depletion of Li inventory due to the repeated formation of new SEI.

Various improvements were made over the years to make battery electrodes more stable and reliable [8]. Cathode material surfaces can be coated with oxides, such as Al₂O₃, SiO₂, TiO₂, and more to prevent direct contact with electrolyte, suppress phase transitions, and improve structural and thermal stability. Anode materials, which suffer from thermal decomposition of SEI, have also seen improvements. Modifying the SEI by mild oxidation or metal and metal oxide deposition was shown to improve SEI stability. Smoothing active edge surfaces and covering edge

structures reduces the number of reaction sites and protects graphite from exfoliating. Electrolyte used in Li-ion batteries is highly volatile and flammable, and reacts with both cathode and anode active material, especially at elevated temperatures. In order to mitigate these reactions and risk of fire, various additives are now added to electrolytes. Additives are added to improve SEI formation, protect cathode active materials, stabilize LiPF₆ salts, enhance solvation, prevent overcharge, and function as fire retardants. Separators, which are made of a combination of polyethylene (PE) and polypropylene (PP), are synthesized to shut down the Li ion transfer as the cell temperature increases beyond 130°C [9]. A tri-layer PP/PE/PP separator coated with a ceramic, such as Al₂O₃ or SiO₂ is also utilized and enhances the separator collapse temperature.

A number of safety devices have also been implemented over the years [8]. Modern cell designs feature current interrupt devices (CID's), vent caps, and shutdown separators. A CAD model with photos and a CT scan image of a cap used in the cells investigated are shown in Figure 3. These function to render a cell electrically inert, vent built up gas, and stop electrochemical reactions, respectively. At the battery pack level, there is the battery management system (BMS) to monitor cell and pack behaviors, a variety of sensors (voltage, temperature, and sometimes gas), and thermal fuses to prevent excessive current flow.

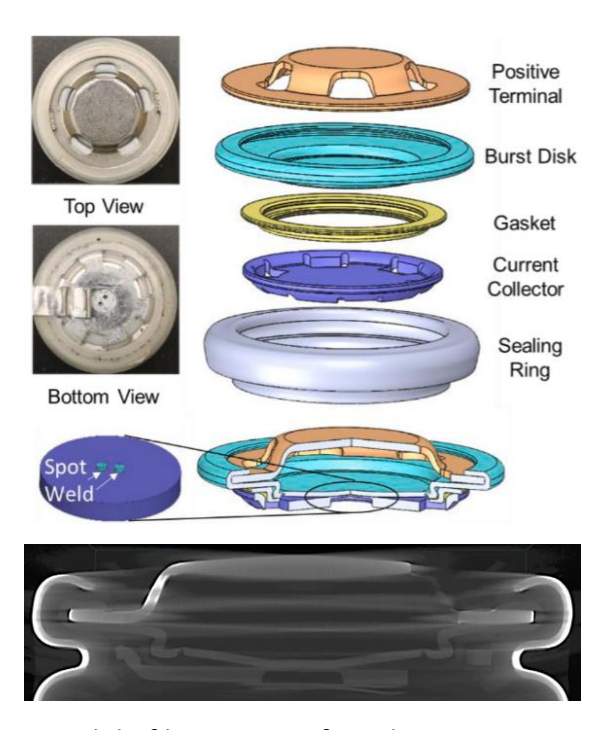


Figure 3: Photos and CAD model of battery cap from literature [10], CT scan image of battery cap from a sample.

1.2: Thermal Runaway of Lithium-Ion Batteries

When a cell operates outside of normal conditions, many undesirable side reactions can occur [9]. On the anode side, SEI decomposition – an exothermic process – occurs between 80°C and 120°C. As the SEI decomposes and the active material is exposed to electrolyte, the SEI layer is created again. This process, called SEI regeneration, is also exothermic. Between 120°C-250°C, the decomposition and regeneration reactions are balanced and occur simultaneously. As temperatures rise above 250°C, the structure of the graphite collapses and the active materials reacts with electrolyte, which contributes to further internal heating. At the cathode, a variety of exothermic reaction begin at 260°C. These reactions result in the cathode active material decomposition and oxygen generation.

The electrolyte decomposes via exothermic reactions as well. The LiPF₆ salts begin decomposing at 230°C. The onset of electrolyte decomposition begins at 256°C which produces hazardous byproducts, such as HF. Other gases, such as CO and H₂, are also created during electrolyte decomposition. These substances are vented out of a cell during TR and can ignite into disastrous combustions.

The separator, usually a porous mix of PE and PP, has melting points at 130°C and 170°C.

The melting of the separator is an endothermic process, though not enough to remove energy generated by the other reactions. The melting of the separator results in the shrinking, which also closes the porosity – shutting down the Li ion transfer between the electrodes. If the internal heating was caused by exceedingly high current, then the shrinking of the separator can help slow down, or even prevent, a TR condition caused by electrical abuse such as external short circuit, high current, overcharge, etc. However, in the event of thermal abuse, the separator will keep melting and shrinking. This will lead to separator collapse and vaporization (at a high enough temperature), allowing the two electrodes to come into direct contact. The ISC caused by this generates massive amounts of heat, leading to a violent TR reaction. There are various methods of studying cell behavior and thermal runaway. Calorimetry, such as accelerating rate calorimetry (ARC), is an effective way to quantify the heat generated by various reactions and their thermal peaks. Computer models and simulations are useful for studying the compatibility of chemistries, growth of dendrites, and more.

Current state-of-the-art products use an onboard battery management system and a variety of sensors to monitor batteries and detect an abnormal state. Voltage, current, and temperature are the usual metric used for diagnosis and to identify the onset of thermal runaway, but these have limitations. For example, the heat generated inside the battery will take time to be detected by thermocouples mounted on the surface due to the low thermal conductivity of polymeric separators and other battery components. Spinner et al. [11] reported on the temperature distributions within 18650 surrogate cells during a temperature step-change experiment, finding that the low axial conductivity led to temperature gradients of 7-9 °C. Furthermore, these temperature gradients took more than 20 minutes to reach equilibrium, suggesting that surface mounted thermocouples would be significantly delayed from detecting temperature rise within the center of a cell. One such scenario leading to rapid internal temperature rise is an internal short-circuit, which can be difficult to detect within individual cells prior to thermal runaway [12,13]. Monitoring the physical behavior of cells (e.g., electrode and cell volume changes) could provide more instantaneous insight into battery health and can even be used as a diagnostic tool to predict thermal runaway.

Most battery electrodes change volume during lithiation and de-lithiation due to

associated phase changes in the active materials. Graphite, which is still the most popular choice for commercial negative active materials, experiences about 10% volume change [14]. Silicon, which has received much attention due to its low cost, high abundance, and high theoretical capacity (3579 mAh g⁻¹ for silicon vs. 372 mAh g⁻¹ for graphite), is also a popular choice for negative active material active material. Although its high volumetric expansion (>300%) [15] causes fracture and short cycle life, it is already experiencing adoption into commercial battery negative active materials in small quantities (~5 wt.%) typically in the form of silicon oxide [16].

1.3: Strain Measurements for Battery Health Monitoring and Thermal Runaway Prevention

The volumetric change of battery cells due to the expansion and contraction of electrode active materials during cycling is a promising metric for battery diagnostics purposes. The mechanical expansion of the electrodes translates to the surface of a cell more quickly than the heat transfer to the surface of the cell, providing a real-time look into the electrochemical and mechanical state of the cell. Recent studies have used a plethora of methods to explore volume changes at the electrode and cell level, including displacement sensors [17–20], load cells [21,22], XRD [21,23,24], fiber optic sensors [25–29], multi-beam optical sensor [30,31], synchrotron X-ray computer tomography (CT) and digital volume correlation [32], laser scanning [33], and tensile experiments [34]. Recently, a gas pressure sensor was also used to infer the electrode behavior of a cell during cycling [35]. A variety of models [18,36,37] have also been used, as well as finite-element methods [38], to study the expansion behavior of cells.

Strain gages have also been utilized to study battery expansion behavior at the stack [39], cell [40,41], and jelly roll [42,43] levels. Wang et al. [39] utilized strain gages to track the volume change of several cells in a stack during charge and discharge. Their analysis showed a large strain change between 3.95 to 4.05 V, which correlated to the structural change of LiCoO₂ cathode from the H1 to the H2 hexagonal phase. Hendricks et al. [40] used strain gages to study the behavior of prismatic cells and predicted depth of discharge. Willenberg et al. [41,42] used surface-mounted strain gages to study the diameter change of cylindrical 18650 cells. Their studies used surface-mounted strain gage data to track diameter and volume change behaviors as functions of cell aging. They also performed CT analyses and found that jelly roll deformation developed as cells underwent repeated cycling.

1.4: Cell Degradation During Repeated Overcharge and Strain

Overcharge behavior of lithium-ion batteries has been a topic of interest for many years [45-47], and has generally been found to cause premature ageing of cells. The ageing mechanisms are usually divided into three main degradation modes (DM's): loss of conductivity (LoC), loss of lithium inventory (LLI), and loss of active material (LAM) [48]. LoC is usually caused by the degradation of binder and electrolyte, as well as current collector corrosion. LLI is related to the reactions between the active material and electrolyte, solid electrolyte interface (SEI) layer growth, and lithium plating, which consume the amount of lithium which is available for lithiation and delithiation of the active material. Finally, LAM occurs when the active materials undergo irreversible phase transformations. The processes which occur during LLI and LAM failure modes are usually accompanied by gas evolution from electrolyte decomposition as well [49]. Modern studies have utilized electrochemical impedance spectroscopy (EIS) and equivalent circuit modeling to correlate electrical abuse to battery ageing mechanisms [50-59], which provides insights into irreversible reactions occurring within electrodes. Incremental capacity analysis (ICA), which is performed by taking the differential of a cell's capacity with respect to its potential, was also shown to be useful in identifying DM's. A usual Nyquist plot, which is used to quantify the real (Z_{Re}) and imaginary (Z_{Img}) parts of a cell's impedance, along with the usual DM's associated with the changes in each, is shown in Figure 4 below.

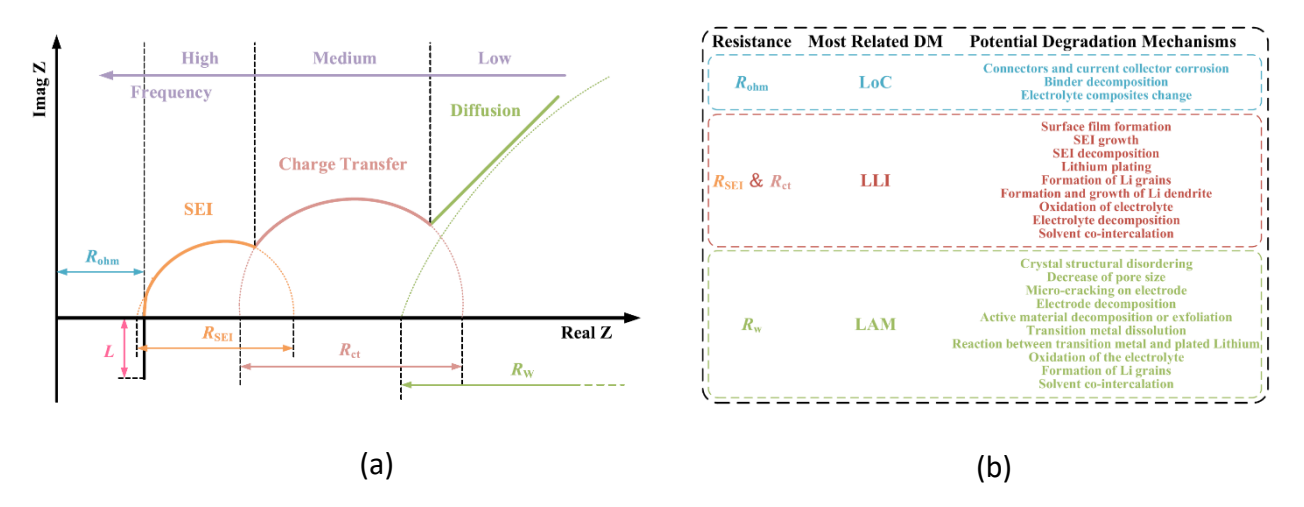


Figure 4: (a) Nyquist plot showing the components of a usual EIS data set from a Li-ion battery and (b) the DMs associated with the changes in each arc/region of the EIS spectrum [58].

The concept of using strain measurements to track the state of health of a cell is still fairly new. While a cell's strain signature was shown to correlate directly to the electrochemical reactions occurring within electrodes during normal cycling [60], this relationship during abuse conditions remains largely unexplored. Previous overcharge experiments showed that strain measurements can detect CID activation during overcharge to failure, though whether degradation during relatively mild overcharge can be detected using strain is still unknown.

1.5: Electrochemical Modeling and Mechanical Predictions

One of the most popular models used to capture the electrochemical behavior of modern anodes and cathodes is the pseudo 2-dimensional (P2D) model proposed by Doyle and Newman in 1993 [61], which was later revised [62] and extended to a full cell in 1996 [63]. Prior to this, the most accurate electrochemical models of the time utilized porous electrode theory [64], which accounted for the large interfacial area of the electrodes and its effects on electrochemical reactions. In 1982 West et al. [65] applied porous electrode theory to model intercalation electrodes, which involved transport in the electrode and electrolyte phases. The transport in the electrolyte phase was described using dilute solution theory. The major improvement on this by Doyle and Newman in 1993 came from using concentrated solution theory, which correctly defined transport properties within the electrode-electrolyte system [66]. An important objective of this model was to be general enough to be applicable to all the materials used in lithium-polymer-intercalation systems at the time.

The reason this model is named pseudo 2D is due to the primary dimension being the thickness of the electrochemical system (e.g., length x) while the second pseudo dimension is the radius of the active material particles. The first dimension relates to the concentration gradient of lithium ions within the electrode and electrolyte phases, while the second to the concentration gradient of lithium within the active material particles. This model was recently extended to a pseudo 4-dimensional (P4D) [67] form, where the mass, charge, and energy conservation, along with reaction kinetics, for the previous 1D model were extended to be fully resolved in a 3D geometry. The fourth dimension in the P4D model remains the radius of an active material particle to model both lithium (de)intercalation and diffusion throughout the active material.

This electrochemical model is useful for simulating the effects of charge, potential, and

current gradients to understand the effects of battery design on performance and longevity. Since the electrochemical reactions and their rates can now be fully resolved in 3D space, this has important implications for the mechanical design of a battery. The results of a P4D simulation could be used to sense areas of stress concentration within electrodes, which could be useful for predicting mechanical damage. The electrochemical simulation results are also useful for predicting the stress on the cell level, which is the goal of the modeling process in this work.

A number of recent studies [68–70] used the P4D model in COMSOL Multiphysics with the volume change of active material to model the mechanical response of a battery, but these have limitations. The volume change of the active material within the electrodes was usually assumed, and the stress within the electrodes was the product of said assumption. Additionally, the mechanical properties of electrodes were taken from previous studies, which did not account for different volume fractions of active materials and different cathode chemistries. The model formulation used in this work addresses both of these issues. By using fundamental cell volume expansion data of active materials from XRD studies, the model can be adapted to virtually any active material. Furthermore, to reduce the need for mechanical characterization of each new electrode design, the Mori-Tanaka homogenization scheme is applied to attain realistic effective properties for composite porous electrodes.

1.6: Objectives of the Dissertation

The overall objective of this work is to characterize the mechanical behavior of Li-ion cells and identify signs of damage and precursors to TR. This is done experimentally for a Li-ion cell with graphite/silicon and NCA chemistry, where a baseline strain signature is established (Objective 1) and then compared to the abuse strain response (Objective 2). A modeling framework (Objective 3) is put forth to predict the average stress within a cell and the strain on the surface of the casing, which is meant to extend this work to various chemistries and combination of constituents within a composite electrode. The goals of the three main objectives are described in detail below.

The first objective of this dissertation, which constitutes CHAPTER 2, shows that strain data measured at the surface of cells can be utilized to provide insight into the reversible phenomenon inside of a battery in real time. The development of an experimental setup to

measure battery potential, current, surface strain, and temperature is described in this chapter. This data is collected initially at a slow C/10 rate to minimize temperature changes and ensure that the strain response is due to the electrochemical reactions. The contribution of thermal strain to the total behavior of cells is also identified through heating/cooling experiments. Data is then collected as cells cycle at increasingly faster rates (i.e., C/5, C/2, and 1C) to determine the effects of charge rate on strain, temperature, and electrochemical reactions.

The second objective, which comprises CHAPTER 3, characterizes the strain behavior of cells as they are subjected to abuse cycling conditions and identifies changes in the strain signature which could be used to track a battery's state of health and predict TR. For this objective cells are overcharged past the nominal capacity and the cutoff voltage until CID activation, and are then heated to TR. A second overcharge scenario is studied as well, where cells are repeatedly overcharged by 5% and 10% of their nominal capacity as changes in the electrochemical and strain behavior are identified. The main degradation modes during overcharge are identified and confirmed through EIS analysis, and the contribution of strain measurements towards their detection are discussed.

The third and final objective of this research, which is discussed in CHAPTER 4, uses a combination of electrochemical and mechanical modeling to predict the stress behavior of each electrode and the surface strain of 18650 batteries. The electrochemical behavior is simulated using a P4D model within COMSOL Multiphysics FEA software and is used as an input for the mechanical simulation. The mechanical model uses fundamental data – the volumetric unit cell expansion of active material as a function of lithium content and elastic properties of each constituent – to predict the mechanical response of composite electrodes. This is accomplished by calculating the volume change of the entire composite and applying it as a thermal strain to the domain. The effective mechanical properties are calculated by homogenizing the constituents using the Mori-Tanaka approach. The effective mechanical properties and simulation results are compared to literature and show good agreement. The applicability of this model, its limitations and future improvements are discussed.

CHAPTER 2: BASELINE STRAIN BEHAVIOR

Most of the previous studies on strain gages have been primarily qualitative in nature and do not provide a direct correlation between the strain and the electrochemical reactions at the electrode level. Moreover, it is known that the temperature of a cell changes during cycling and is a function of the C-rate, but none of the previous studies discussed these temperature effects in their strain gage measurements. Also, Ni-rich cathodes, such as NMC and NCA, and Si-graphite based composite anodes are attracting a lot of attention due to their high energy density, and no study exists on the strain behavior of this electrode materials. Further, a direct correlation of the electrochemical reactions occurring at the individual electrode, i.e., both anode and cathode, level to the surface strain will enable real-time monitoring of battery health. Also, the strain could be a function of location on the cell as the geometry of the cylindrical cell is complex and jelly roll may induce non-uniform strain. However, none of the previous studies provide any information about the variation of strain on the cell at various locations. Hence, the first main objective of this research is to conduct a comprehensive experimental study to quantify the surface strain on 18650 cylindrical cell and to correlate the strain to the internal state of the cell (i.e., various electrochemical process that occur at the electrode level).

2.1: Experimental Setup for Baseline Strain Measurements

Figure 5 shows the schematic of the entire strain gage measurement and battery cycling setup. A National Instruments (NI) PXIe data acquisition (DAQ) chassis was selected to house a voltage card for thermocouple measurements and a strain card for strain measurement. The excitation voltage and strain gage output readings were performed internally by the strain card, set to quarter bridge configuration to measure the strain form each strain gage. A custom LabVIEW virtual instrument (VI) was created on a desktop PC, shown by the black box on the left side of the figure, to synchronize and record the strain data from the axial and hoop legs of the rosette (to account for the different Gage Factors) as well as the thermocouple data to a single data file. MATLAB code was written to analyze the strain and temperature data collected during experiments. A Solartron 1470E potentiostat was used to electrically cycle batteries to simulate charge and discharge at various rates. Cell temperature was measured using a thermocouple attached to the casing of the cycled cell, while ambient temperature was measured using a

thermocouple taped to the casing of a dummy cell, which are both depicted as green cylinders. The dummy cell used was identical to the cycled cells, but itself was not cycled. All of the experiments for the baseline strain measurements were conducted inside a Thermal Product Solutions Tenney Jr (TJR R1) temperature chamber, which is represented by a light blue box around the 18650 cells in Figure 5, to eliminate fluctuations in ambient temperature.

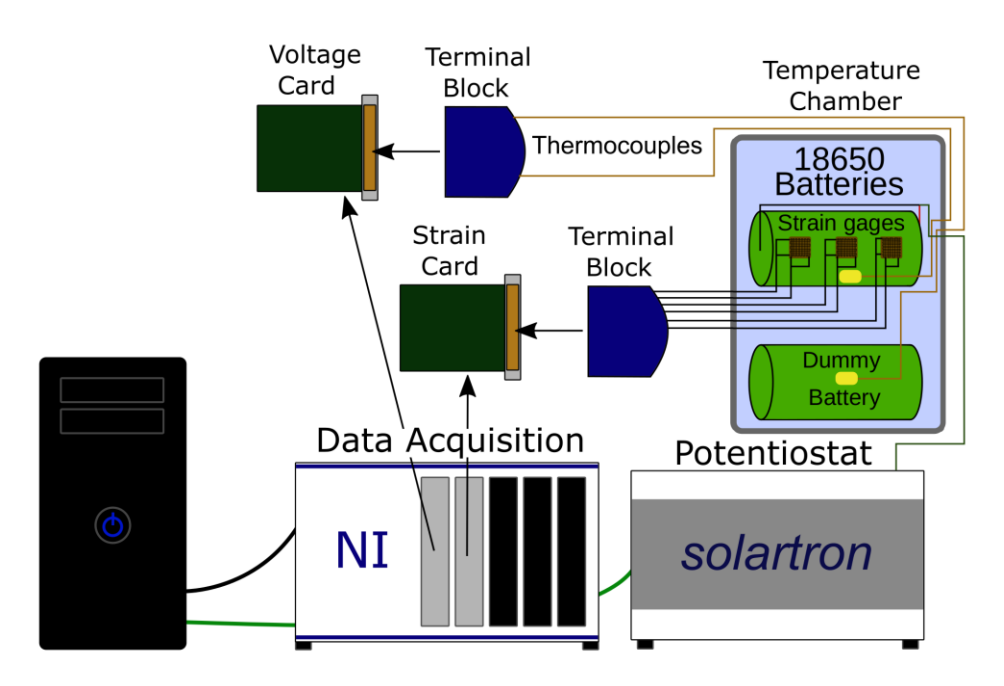


Figure 5: Schematic of strain measurement and battery cycling setup.

Figure 6a and Figure 6b show a schematic and a photograph, respectively, of a 3.4 Ah 18650-format cylindrical cell instrumented with planar T-rosettes (i.e., two strain gages arranged in a way to measure strain in two orthogonal directions, HBM or HBK Inc.) and K-type thermocouples (Omega Inc.). Prior to mounting these sensors, the surface of the cell was prepared for proper adhesion of the strain gages. The shrink wrap around the cell was removed with a utility knife so that only the part above the spin groove remained (to prevent accidental shorts). The surface of the cell was polished with 180 grit Emery Cloth, and then cleaned using lint-free cloths soaked in RMS1 solvent mixture from HBM. The epoxy used to bond strain gages was the X60 adhesive from HBM, which cures at room temperature and can be used in environments of up to 60°C.

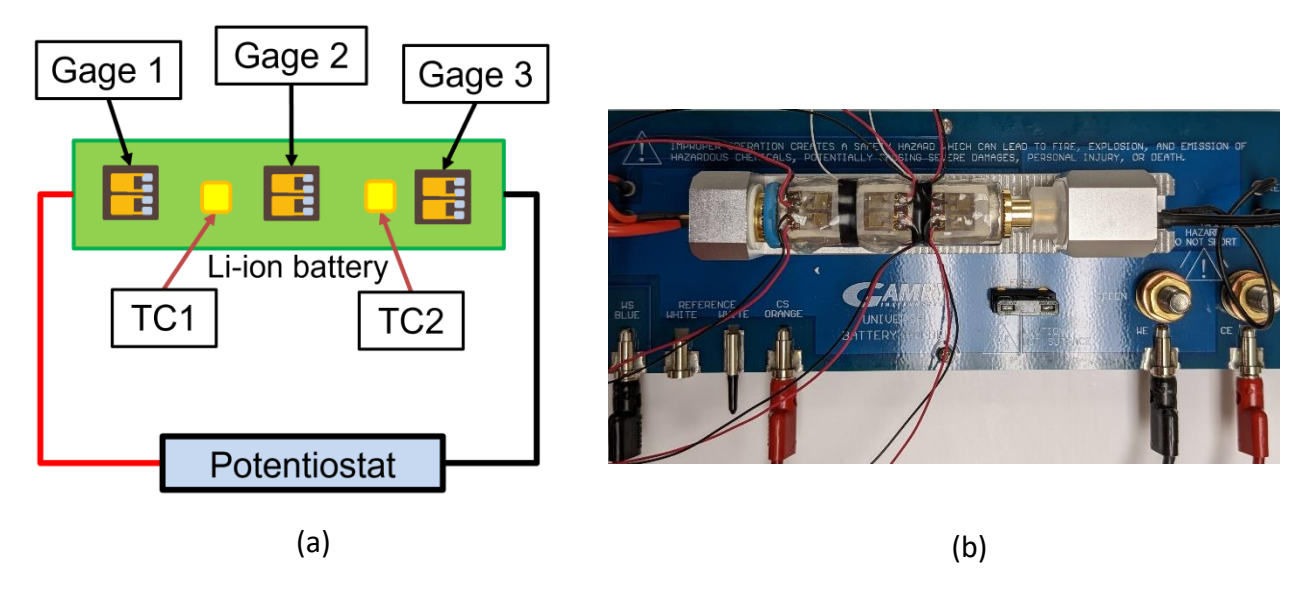


Figure 6: (a) Schematic of an instrumented cell and (b) a picture of a cell instrumented with strain gages and a thermocouple in a cell holder.

Particular care was taken to apply all rosettes as repeatably as possible, i.e., ensuring proper alignment of the rosettes with axial and circumferential directions of the cell and ensuring that the rosettes are positioned at the identical location in all the cells. To apply a repeatable amount of pressure during epoxy curing, a cell holder was machined from 304L stainless steel (SS) block. An 18.2 mm hole was bored through the block, which was then cut in half along the length. After epoxy was applied between the casing and the strain gages, the cell was then placed inside the SS holder with cellophane tape separating the cell and the holder. Then 15 lbs. of weight were placed on top to exert a uniform pressure onto the rosettes during epoxy curing.

Shielded cables were used for strain gage connections to prevent electromagnetic interference from adding noise to the strain measurements. The thermocouple measurement initially contained a high amount of noise due to ground loop issues which were caused by the cell casing and NI voltage card being at different potentials. The noise was eliminated by taping the tips with Kapton tape, thereby electrically insulating them. This prevented electromagnetic interference and reduced the noise of measurements, i.e., the noise of the recorded strain and temperature data was less than $0.01~\mu \epsilon$ and $0.03^{\circ} C$, respectively.

2.2: Electrochemical Cycling Procedure

The parameters for electrochemical tests are described below. At least three separate cells were used for each case. In all the experiments conducted the thermal chamber was maintained at 23°C, except for thermal cycling tests. The cycling scenarios were set up as follows. First, a pre-conditioning constant current (CC) discharge step with 2.5V cutoff potential followed by a constant voltage (CV) step with 100 mA cutoff current was used to ensure that each experiment began at 0% SoC. This was followed by a 2 hour rest at open circuit potential (OCP) to let the potential, temperature, and strain equilibrate. After the pre-conditioning, the cell was subjected to 3 cycles of CC-CV charge with 4.2V and 100mA cutoff, and CC-CV discharge with 2.5V and 100mA cutoff. All CC-CV steps were followed by 2 hours of rest at OCP. The CV step was added to the end of each charge to ensure the cell reaches 100% SoC, and to each discharge to bring the cell down to 0% SoC. It was noticed that at higher C-rates (1C) the batteries retain up to 3% SoC at the end of the CC discharge step.

The electrochemical cycling was done at a variety of C-rates to explore the effects of charge and discharge rates on temperature and strain. During an experiment, C-rates for charge/discharge were chosen and kept constant for all 3 cycles. The chosen C-rates for charge and discharge during each experiment were as follows: C/10 charge and discharge, C/5 charge and discharge, C/5 charge, and C/5 charge, 1C discharge. In all these experiments, a 2 hour rest step (i.e., OCP) was included between charge and discharge steps. The convention used to express C-rates is full charge/discharge per hour, meaning that a C/10 rate signifies that a full charge or discharge was achieved in 10 hours, whereas a 1C rate would mean that a battery was charged or discharged in a single hour.

All data analysis was conducted in MATLAB. The differential capacity (dQ/dV) and differential strain (d ϵ /dV) were calculated from the Q vs. V and ϵ vs. V data, respectively, using the MATLAB "polyfit" function with a prescribed number of points. A first degree polynomial mx+b was acquired, where m was the dQ/dV or d ϵ /dV value. All data was collected at a 1 Hz rate; therefore, a high number of points were needed – especially for the C/10 rate experiments – to yield smooth dQ/dV and d ϵ /dV curves. The minimum number of points – or window – used for C/10, C/5, C/2, and 1C galvanostatic steps were 60, 40, 20, and 10, respectively. If an error was

generated during evaluation using the "polyfit" function stating that the polynomial was badly conditioned, the window was expanded until no such error occurred. If curves were generated without an error but were still noisy, we window was increased as well.

2.3: Electrode Characterization

2.3.1: CT Analysis

The internal structure of the 18650 cells was investigated using Computed Tomography (CT) scan analysis. Figure 7a, Figure 7b, and Figure 7c are the computed tomography – or CT-scan images – of a cylindrical cell showing the side, zoomed image of Figure 7a, and top views, respectively. It can be seen that the center of the cell is hollow and does not contain a mandrel. Also note from the images that the jelly roll (a stack of cathode/separator/anode spirally wound into a cylinder) does not contact the header or the bottom of the cell casing, i.e., the length of jelly roll is smaller than that of cell casing. The alternating bright and dark rings visible in Figure 7b and Figure 7c are the Ni-rich layered oxide composite cathode and graphite-Si composite anode films, respectively. The copper current collector is visible in Figure 7b, and the dark (anode) coating is seen on both sides of the current collector. Likewise, the aluminum current collector has cathode coatings on both sides. However, Al is barely visible in Figure 7b (as the dark line down the center of the cathode layers) due to its relatively low density (resulting in lower intensity during CT scan data acquisition). A thin polymer separator exists between cathode and anode films to prevent the physical contact between them but is not clearly visible, because the thickness of this separator is close to the resolution of the imaging system.

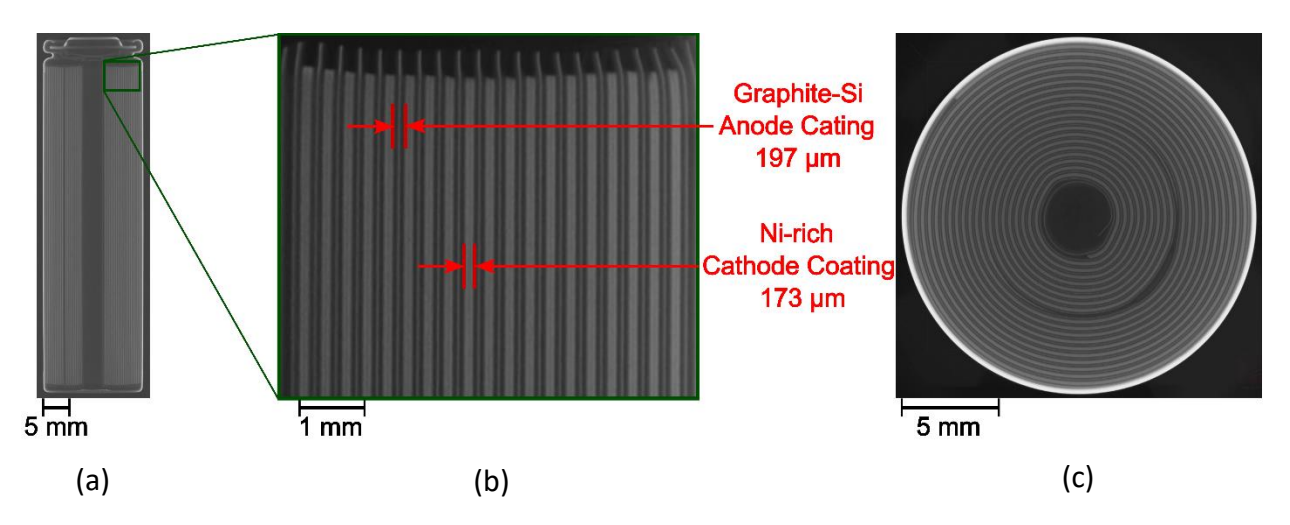


Figure 7: CT cross-section images of the 18650 cylindrical cell showing (a) side (full cell), (b) side (zoomed-in), and (c) top views.

2.3.2: SEM and EDS Analysis of Harvested Electrodes

In order to accurately characterize the electrochemical reaction occurring in the cells, characterization of the active material was needed. To perform this, electrodes were harvested from a fresh cell and analyzed in an EDS-equipped SEM. The SEM image of the negative electrode in Figure 8a below shows that the majority of the negative active material contains spherical and oblong graphite particles, approximately $10\text{-}20~\mu\text{m}$ in diameter. An EDS analysis of the anode revealed the silicon content to be approximately 5.70 ± 0.18 atm%, which is within the range reported in literature [16]. An SEM analysis of the cathode, depicted in Figure 8b, showed a much smaller particle size, with the primary (individual) particles smaller than $1~\mu\text{m}$ and the secondary (or agglomerates of primary particles) on the scale of $25\text{-}50~\mu\text{m}$. An EDS analysis was conducted for the cathode electrode as well, and yielded a well-distributed elemental map of Ni, Co, and Al. The Ni concentration reported was high, comprising approximately 80% of the active material, alluding to the use of either a Ni-rich NMC (NixCoyMn1-x-y with x > 0.8) or NCA (LiNi1-x-yCoxAlyO2 with 1-x-y > 0.8) chemistry. As such, NMC811 and Ni-rich NCA are both possible candidates, though the former is less likely due to the lack of Mn and presence of Al in the EDS spectra (Table 1 and Table 2).

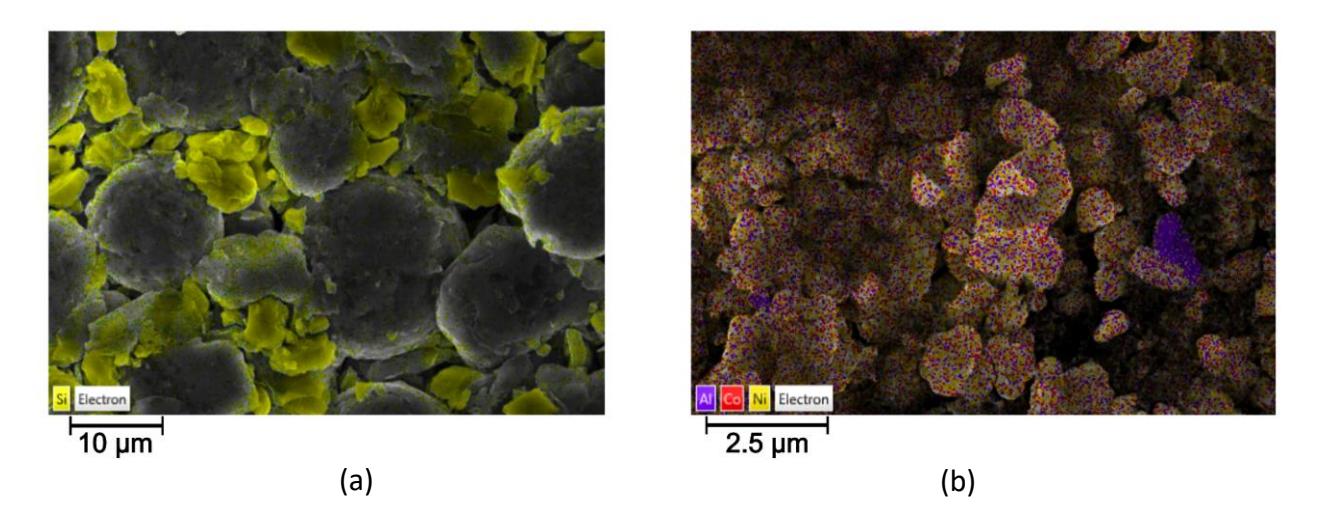


Figure 8: The EDS analysis of (a) the negative electrode confirms the presence of silicon (in yellow), and in (b) the positive electrode the presence of nickel (in yellow).

Element	Atomic %	Wt. %	
С	83.78	0.66	
0	12.4	0.13	
Si	3.81	0.07	
Cu	0.01	0	
Total	100	0.86	

Table 1: EDS spectrum of anode, averaged over 3 locations.

Element	Atomic %	Wt. %		
С	40.48	0.18		
0	33.97	0.1975		
F	6.21	0.045		
Al	1.23	0.0125		
Со	2.79	0.06		
Ni	15.32	0.3275		
Total	100	0.85		

Table 2: EDS spectrum of cathode, averaged over 3 locations.

2.3.3: Strain Drift and Thermal Expansion Experiments

A drift test was performed on one of the instrumented batteries to quantify the uncertainty in the strain measurements with the test setup. At the lowest C-rate (C/10), the experiment duration is just over 3 days; hence, to quantify the drift during such a time period

and beyond, a 7-day duration was chosen for this drift test. Figure 9 shows that, over the course of the 7-day test, the strain drifted linearly with time and reached a maximum value of $\pm 10~\mu \text{s}$ at the end of the 7th day. Hence, the uncertainty in the strain measurements due to drift is negligible.

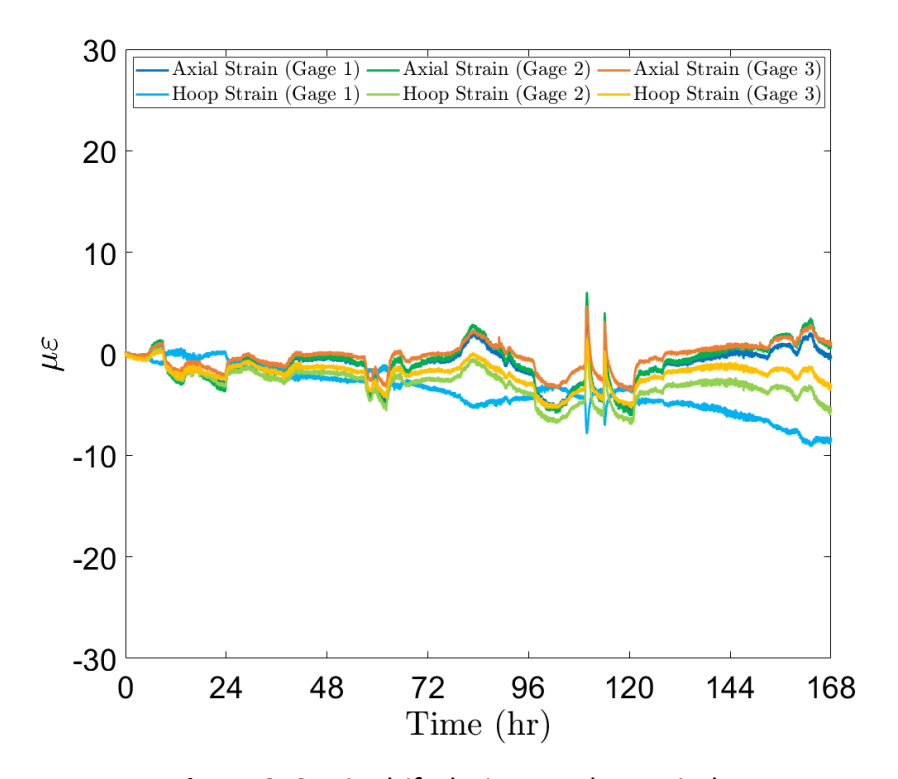


Figure 9: Strain drift during a 7-day period.

Since the primary objective of this study is to infer the internal state of an 18650 cylindrical cell from the strain measured on the surface, it was important to quantify the strain contribution due to ambient as well as the cell temperature fluctuations. Hence to measure the strain purely due to temperature changes, the cylindrical cells were subjected to heating and cooling cycles by varying the temperature of the TJR environment chamber from 45°C to 5°C as shown by dashed red curve in Figure 10a (within the operating limits of the batteries). The hoop strain measured from the middle of the cell (i.e., from Gage 2 in Figure 6) during this experiment as a function of temperature is shown in Figure 10b. The heating and cooling cycles, as in Figure 10a, were performed on cells at 0% (fully discharged), 50% (half charged), and 100% (fully charged) states of charge (SoC) to see if SoC affects the strain measurements due to temperature changes. The cells have a capacity of 3.4 Ah; therefore, cells were brought to 0 Ah, 1.7 Ah, and

3.4 Ah of charge corresponding to at 0%, 50%, and 100% SoC's, respectively, before conducting thermal cycling. The starting temperature for all these thermal experiments was 25° C, and the strain at the beginning of the experiment for all the cells, i.e., cells at all SoC's, was set to 0 $\mu\epsilon$.

Figure 10b shows that, a temperature rise of 20° C, i.e., $\Delta T = 20^{\circ}$ C results in a change of strain, i.e., $\Delta \epsilon$ of 143 $\mu\epsilon$, 134 $\mu\epsilon$, and 162 $\mu\epsilon$ at 0%, 50%, 100% SoC, respectively. During the cooling step when temperature was lowered by 20° C, i.e., $\Delta T = -20^{\circ}$ C, the strain of the cell at 0%, 50%, and 100% SoC's reached -151 $\mu\epsilon$, -167 $\mu\epsilon$, and -141 $\mu\epsilon$, respectively. Hence it is evident from the Figure 10b that the change of strain per °C change in temperature is constant with an average value of $\Delta\epsilon$ / $\Delta T = 7.5 \mu\epsilon$ /°C for various SoCs; note that all the curves have identical slopes. Hence, it can be concluded that the thermal expansion of the cell is fairly independent of the SoC, and this data will aid in identifying the strain due to temperature changes in the cell.

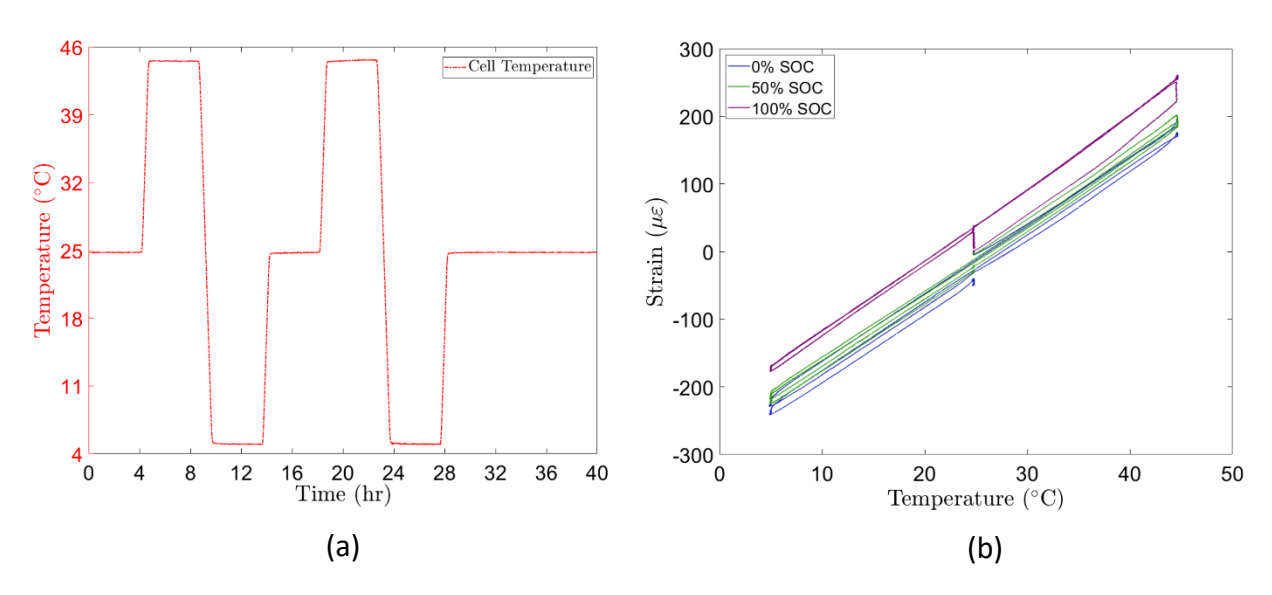


Figure 10: Middle hoop strain during thermal cycling at 0, 50, and 100% SoC as (a) strain and temperature vs. time and (b) strain vs. temperature.

2.4: Electrode Strain Measurements

2.4.1: Strain variation along the axis of 18650 cylindrical cell

Figure 11 shows both the hoop and axial strain data from Gage 1, Gage 2, and Gage 3 as a function of time during three consecutive C/5 charge/discharge cycles. It can be noted that the overall trend from all the gages is same, i.e., peaks and valleys coincide, but the magnitude of the strain is different. The hoop strain from Gage 2, i.e., mid-section of the 18650 cell has the highest

magnitude while the hoop strain from Gage 1 and Gage 3, which are near the ends of the cell show almost half of that magnitude. This can be attributed to the geometry of an 18650 cell and the arrangement of jelly roll within the cell casing. As seen in the CT scan image in Figure 7, the jelly roll does not extend throughout the cell and is not in contact with the top or the bottom of the casing. Consequently, the bottom of the cylinder and cap at the top impose constraints to the expansion of the cell when jelly roll tries to push in the radial direction. Since there is no such constraint at the center, the hoop strain from Gage 2 (or in the middle of the cell) shows the highest magnitude.

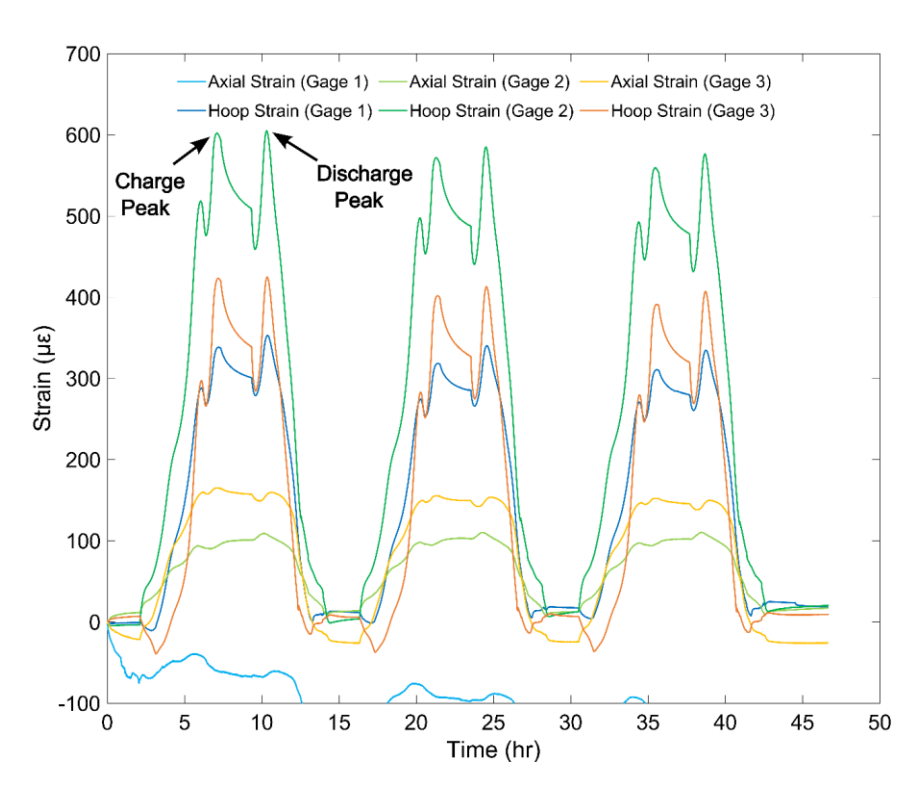


Figure 11: Strain measurement from all three rosettes (i.e., the three gages shown in **Figure 6**) during three C/5 cycles.

In addition to being the highest in magnitude, the strain at the center (or from Gage 2) is the most consistent from cell to cell compared to the strain from the other locations. For example, the axial strain magnitudes are relatively lower (i.e., a peak value of $100~\mu \epsilon$) compared to the hoop strains (~650-700 $\mu \epsilon$), and the axial strains also had high variance between cells. The low magnitudes of axial strain can be attributed to the way the jelly roll interacts with the cell can. For example, as the jelly roll expands/contracts during charge/discharge, it cannot push on

the header or the bottom of the casing to cause direct change in the axial (strain) dimensions of the cell. However, it can induce an axial deformation through the friction between the jelly roll and the can. Hence, the coefficient of friction between the jelly roll and the casing could be a major factor that could affect the axial strain and associated inconsistency. Consequently, in some of the cells the axial strain was even negative, i.e., an indication of contraction.

Since the middle location, i.e., Gage 2 in Figure 6, is the farthest from the irregularities in geometry (i.e., cylinder ends), the strain signature from that rosette is the most consistent, and as expected it was the case in all the cells evaluated in in this study. Hence, if the strain is used to monitor the health or state of the cell, the hoop strain signal from the mid-section of the cylindrical cell should be selected for such study. Consequently, the remainder of the paper focuses on the hoop strain from Gage 2, i.e., hoop strain at the mid-height of the 18650 cylindrical cell.

2.4.2: Cell Break-In Behavior

Figure 12a shows the hoop strain signal from Gage 2 of a fresh cell as a function of time during the first 20 cycles at C/5 charge/discharge and note that the strain signal evolves initially as the fresh cell is subjected to cycling. The overall strain magnitude at any given SoC during the first 4-5 cycles changes. The strain magnitude gradually increases and reaches a maximum in the fifth cycle and decreases slightly before stabilizing. Hence before testing at the C/10, C/5, C/2, and 1C rates, all the cells of this study were cycled for 20 times at a C/5 rate to bring the cells to stable strain behavior, and this process is referred to as a "break-in" procedure.

The peak strain during charge process and discharge process as a function of cycle number along with the coulombic efficiency of the cell is shown in Figure 12b. Note that the cycling efficiency remains around 99.8% throughout the break-in cycling, suggesting no significant changes to the electrochemical state of the electrodes occurred and the effect of side reactions on the cell behavior during the break-in process is minimal. However, the interesting observation is that surface strain evolves, and during the first 4-5 cycles when the strain signal is still evolving the maximum strain in a given cycle occurred during the charging process (i.e., the dotted line is below the solid line), but after the 5th cycle the maximum strain occurred during the discharge process, i.e., the dotted line crosses and stays above the solid curve for the remaining cycling

history, and the gap between these lines reaches a steady state. This feature/behavior is consistent in all the cells evaluated in this study. This could be attributed to the electrodes shifting and the jelly roll settling into within the cell casing. Hence, the surface strain complements the electrochemical data and provides valuable information about the internal physical state of the cell.

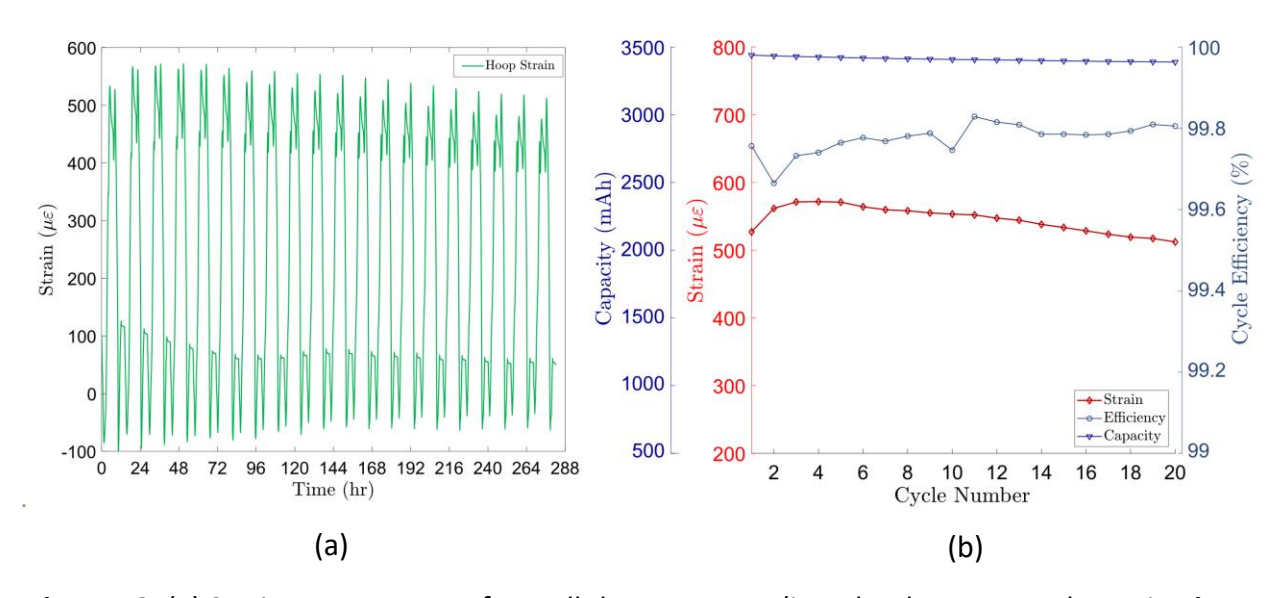


Figure 12: (a) Strain measurement from all three rosettes (i.e., the three gages shown in **Figure 6**) during three C/5 cycles. (b) The hoop strain signal (from Gage 2) for several cycles is plotted showing how it evolves with cycles before reaching steady state behavior. (c) Cycle efficiency, discharge capacity, and maximum strain during a given cycle is plotted as a function of cycle number.

2.4.3: Surface Strain Behavior as a Function of SoC

The surface strain, potential, and temperature of 18650 cell as a function of SoC (or time) during a typical C/10 galvanostatic charge/discharge cycle is shown in Figure 13a. The data shown in Figure 13 is the hoop strain from Gage 2 (see Figure 6), i.e., at the mid-section of 18650 cell which indicates the changes in the circumferential dimension of the cell. In a typical cycle, as shown in Figure 13a, during the charging process, i.e., when Li is removed from cathode and inserted into anode particles, the strain increases non-linearly with SoC (or time) initially, reaches a peak value of 460 μ s at 80% SoC and decreases to 418 μ s at 87% SoC before increasing again to reach the maximum strain value of 542 μ s at 100% SoC. Hence, the maximum hoop strain occurs at the end of charge, which means that the cell diameter will be the largest at the end of

the charge. The reason for the decrease in the strain between 80% and 87% is believed to be the significant shrinking of cathode particles [71]; a detailed discussion on this is provided later. At the beginning of discharge a sharp decrease in strain of a magnitude of 20-50 μ s was observed followed by an increase leading to a peak strain at 80% SoC comparable in magnitude to the strain at the end of the charging step; the strain decreases thereafter in a non-linear fashion until the end of discharge. The strain vs. SoC trend during the discharge almost mirrors the trend observed during the charge process. The strain approaches 0 μ s at the end of discharge, implying that the phenomenon responsible for the strain is reversible, e.g., reversible electrochemical reactions.

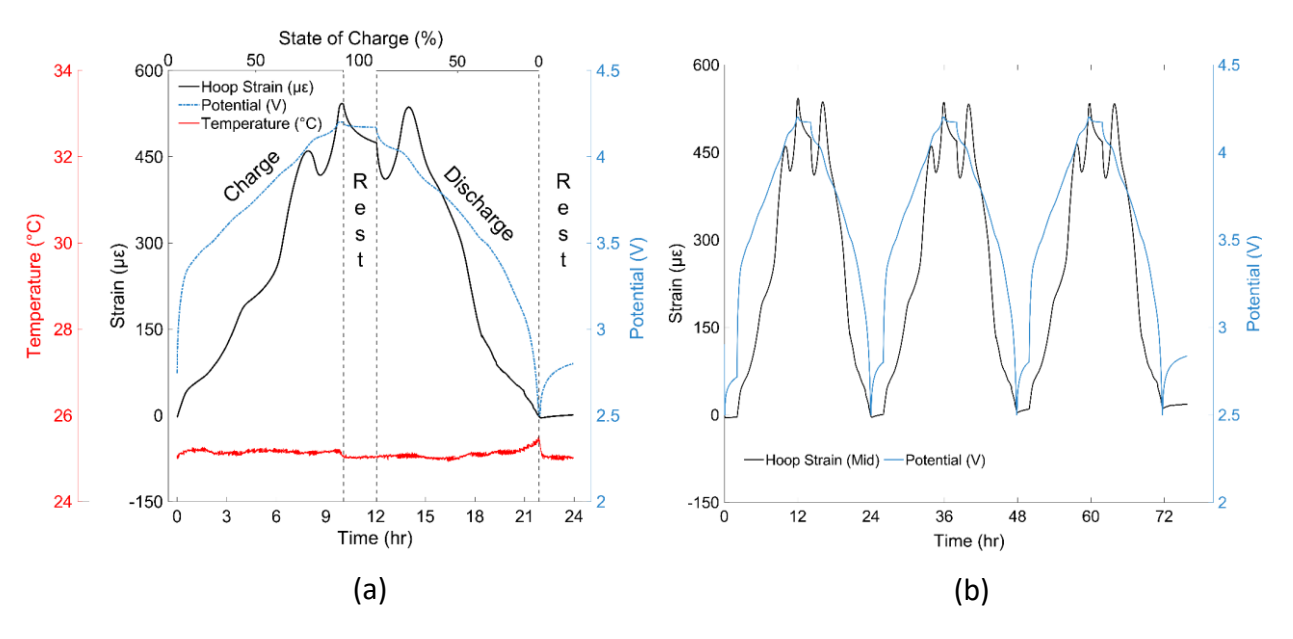


Figure 13: a) Strain, potential, and temperature vs. time during a typical C/10 charge/discharge cycle with a 2 hr rest step in between, b) strain and potential vs. time for 3 cycles showing consistent cycling behavior.

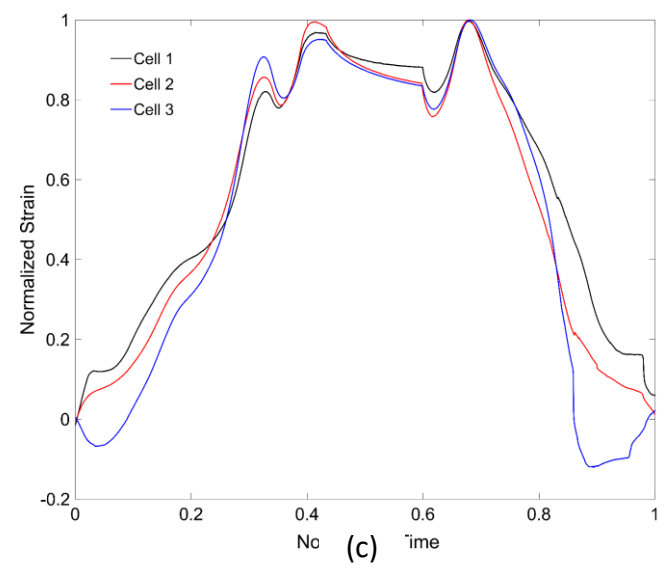


Figure 14: Typical strain (normalized with the peak strain at 100% SoC) response during a C/5 charge/discharge cycle from three different cells confirming that the strain signature observed is a function of anode and cathode chemistry and electrode and cell fabrication/processing parameters.

During the rest step there is strain relaxation of 50-100 $\mu\epsilon$, which is seen to almost level out by the end of the two hours. Full relaxation (i.e., to reach stable strain value) can take as long as 8 hours, but the largest change happens within the first two. The relaxation behavior observed during the rest step can be attributed to the time-dependent deformation behavior of the electrode constituents such as polymers (binder and separators) and the active materials such as lithiated Si. Although binder only makes up a small percent of a composite electrode, Sethuraman et al. [30,72] experimentally demonstrated that the stress response of a composite electrode is strongly influenced by the mechanical behavior of the binder, and it is well known that the polymers, in general [73], and binders such as PVdF undergo stress relaxation [74]. Further, the active materials such as lithiated Si are viscoplastic in nature [75] and undergo stress relaxation during the rest period as shown experimentally by Sethuraman et al. [76]. Further, it should be noted that the temperature of the cell also relaxes during the rest step contributing to the strain relaxation observed during the rest step.

The overall increase in hoop strain during charge process (or overall increase in cell diameter) and decrease in the strain during discharge process can be attributed to the volume changes (or change in lattice parameters) of active particles in anode and cathode associated with the Li intercalation/insertion reactions. For example, it is well known that the volume of

graphite [77] and Si [78] increases monotonically with the SoC during lithiation. Several studies on the Ni-rich cathodes [23,79,80] showed that the volume of Ni-rich active material particles remains almost constant and decreases slightly at the end of SoC during de-lithiation. The overall effect of this would be an increase in the volume of the jelly roll during charging process, causing an increased strain as shown in Figure 13. Since the phase changes are reversible, the associated volume changes are also reversible during the discharge process resulting in the overall decrease in the strain. Further, the graphite and Si particles experience a volume change of greater than 10% and ~300%, respectively, during cycling while the volume change of cathode particles is relatively small; hence, the magnitude of the hoop strain measured is expected to be dictated by the changes occurring at the negative electrode, which is a graphite-Si-based composite in this study. A more detailed explanation of the correlation between strain and phase changes associated with the electrochemical reactions is provided below.

Figure 13b shows that the strain behavior is consistent for a multitude of cycles. In other

words, the strain response is repeatable and reversible, i.e., the trend and magnitude of the strain is not only repeatable in each and every cycle, but it also has one-to-one correspondence with the SoC of the cell. Further, Figure 14 which depicts the hoop strain (normalized with respect to maximum strain) as a function of SoC during C/5 cycling for different cells show that this behavior was consistent among several cells. Note that though the magnitude of the strain measured differs slightly among cells, with an average maximum strain of 570 µE and standard deviation of 109 με (13 different cells), the general trend of the strain remains the same. The difference could be due to cell-to-cell variation or other factors related to the mounting of the strain gauges. Figure 13a also shows that the temperature of the cell changes continuously with SoC during both the charge/discharge processes, but the change is marginal. For example, the maximum temperature rise measured during a typical C/10 cycling was approximately 0.5°C. To quantify the strain contribution due to ambient as well as the cell temperature fluctuations and to measure the strain purely due to temperature changes, the cylindrical cells were subjected to heating and cooling cycles at three different SoC as shown in Figure 10. It was evident from the Figure 10b that the change of strain per °C change in temperature for the cylindrical cells of this study is constant with an average value of $\Delta \varepsilon / \Delta T = 7.5 \,\mu \varepsilon /^{\circ} C$ for various SoCs. In other words,

the thermal expansion of the cell is fairly independent of the SoC. Based on the thermal cycling measurements shown in Figure 10, the thermal strain associated with 0.5° C change in temperature is approximately 4 $\mu\epsilon$ during a C/10 cycle. This amount of strain is negligible compared to the strain magnitudes measured during C/10 cycling. Therefore, the strains recorded on the surface are caused directly by the electrochemical reactions within the cell. Hence, it should be concluded that the strain signal shown in Figure 13 is a function of the microstructure, chemistry, fabrication/process parameters of the anode and cathode. In addition, cell geometry and cell fabrication/process parameters along with the cycling conditions influence the strain signature.

2.5: Differential Capacity Analysis

Differential capacity, i.e., dQ/dV data and strain data is plotted in Figure 15 as a function of cell voltage to further show the correlation between the surface strain and the electrochemical reactions occurring during charge and discharge processes. The dQ/dV and middle hoop strain (i.e., hoop strain from Gage2) as a function of voltage for C/10 charge/discharge process are shown in Figure 15a and Figure 15b. During charge, as shown in Figure 15a, there are clear dQ/dV peaks at 3.5V, 3.7V, 3.9V, and 4.1V labelled as 1, 2, 3, and 4, respectively. During discharge, as shown in Figure 15b, the peaks occur at 4.0V, 3.8V, and 3.5V, labelled as 4, 3, and 1+2, respectively. There is an appreciable increase in the strain at the electrochemical reaction peaks, suggesting that they are the cause of the strain evolution.

Differential capacity peaks for a full cell with graphite negative active material and NMC811 positive active material have been reported by Jung et al. [81] and for a Li/NMC811 cell by Noh et al. [82]. Ni-rich NCA cathode have been studied as well [71,83–85], and show similar differential capacity peaks to NMC811 due to the high nickel content. The first peak, i.e., peak 1 at 3.5 V, in Figure 15a is indicative of the onset of graphite lithiation ($C_6 \rightarrow LiC_X$), and the second peak at 3.7 V represents the onset of hexagonal to monoclinic ($H_1 \rightarrow M$) phase transition within the NMC811 positive active material [33]. The next two peaks at 3.9 V and 4.1 V are determined to be caused by the monoclinic to hexagonal ($M \rightarrow H_2$) and from the hexagonal to a new hexagonal ($H_2 \rightarrow H_3$) phase transitions, respectively, in the positive active material. Hamezuli et al. [86] reported the dQ/dV response of composite anodes containing graphite and silicon, and they

observed that the half-cell redox peak potentials increased and broadened with increasing silicon content. This behavior may explain the small shoulder observed prior to the charge peak number 1 in Figure 15a. It is worth noting that during the charge step, peak numbers 1 and 2 associated with $C_6 \rightarrow LiC_X$ in the negative electrode and the $M \rightarrow H_2$ transition in positive electrode are distinct. During discharge, however, these were observed to broaden and merge together.

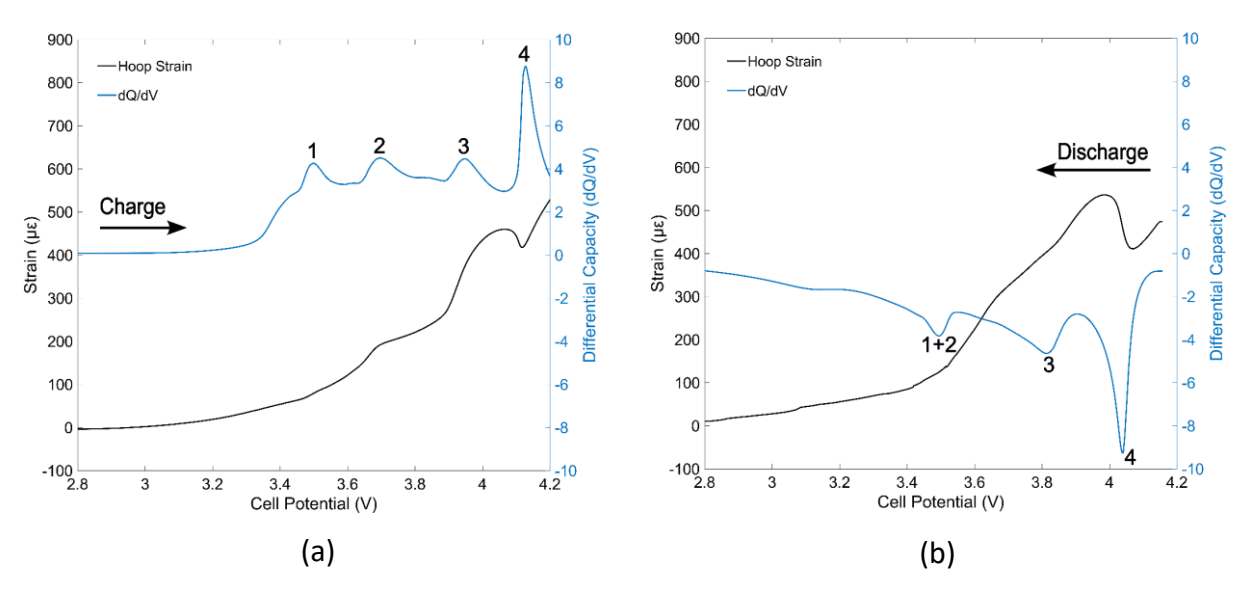


Figure 15: Differential capacity (dQ/dV) and strain vs. cell potential (V) during (a) charge and (b) discharge.

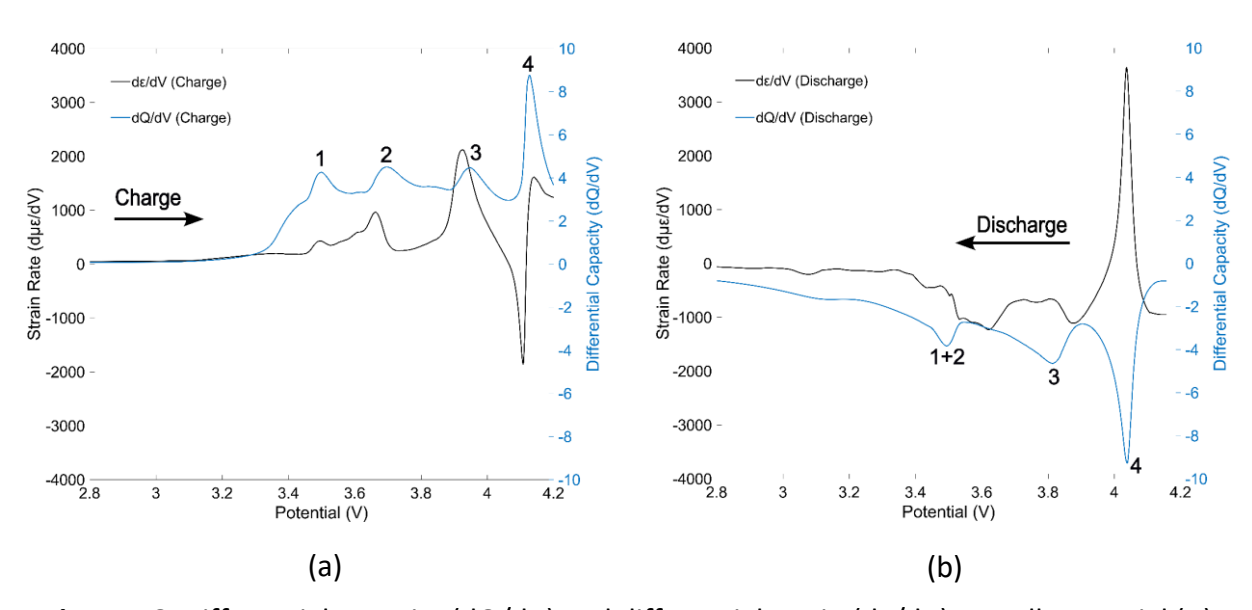


Figure 16: Differential capacity (dQ/dV) and differential strain (d ϵ /dV) vs. cell potential (V) during (a) charge and (b) discharge process.

It should be noted that each peak in Figure 15 not only indicates the onset of a specific phase transition but also indicates the associated volume change of active particles in anode and cathode. Since the hoop strain is an indication of the changes to the dimensions of the jelly roll which occurs due to volume changes of the active particles, the strain measured is an indication of the phase changes or the associated electrochemical reactions. Although the onset of graphite lithiation occurs at 3.5V, the strain increase started at 3.4V which can be attributed to the onset of lithiation of Si which occurs before the lithiation of graphite. It should be noted that all the phase changes associated with the cathode active material: $H_1 \rightarrow M$ transition at 3.7V, $M \rightarrow H_2$ transition at 3.9 V, and $H_2 \rightarrow H_3$ transition at 4.1V, i.e., peak numbers 2, 3, and 4, respectively, in Figure 15a, result in a marginal decrease in volume. Specifically, the volume changes associated with the peaks 2 and 3 are marginal, but the peak number 4 attributed to the hexagonal H2→H3 transition causes a large volume decrease [71]. The interesting point to note here is that although the cathode particles are supposed to either remain unchanged or shrink during the charge process, the surface hoop strain keeps increasing as shown in Figure 13 and Figure 14. This could be attributed to the fact that the magnitude of volume change in anode particles (i.e., greater than 10% and 300% in graphite and Si, respectively), is significantly more than that of cathode particles. In fact, using a rule of mixtures type of analysis, the graphite-silicon combination present in the electrodes could experience up to 19% volume expansion compared to only ~6-7% volume changes in Ni-rich cathode particles. Hence, anode particles govern the strain magnitude. Studies have documented that the lithiation of graphite causes most of the volume change during a charge/discharge cycle [19]. However, the peaks and valleys observed in the strain-voltage plot match with the c-axis lattice parameter change with the voltage in both NMC811 and Ni-rich NCA; hence, although the volume change of positive active material particles is relatively small, the c-axis change is appreciable, and could be playing a relatively more important role in driving the surface strain than the volume change of the Ni-rich particle itself. During discharge, the electrochemical reactions (or phase changes) occur in reverse, and the response follows these phase changes. As a result of the one-to-one relation of the strain and the phase changes in the anode and cathode, the rate at which the strain changes with respect to voltage is noticeable at the onset of phase changes in Figure 15a and Figure 15b.

Figure 16a and Figure 16b show the differential strain data $d\epsilon/dV$ as a function of cell potential V during charge and discharge process, respectively. An interesting point to note here is that the $d\epsilon/dV$ peaks almost always appear to be either preceding or coinciding with the dQ/dV peaks. This is interesting because it appears that the strain signals can indicate the onset of structural changes in the anode and cathode particles slightly earlier than the dQ/dV data.

2.6: Effects of C-Rate on Cell Behavior

2.6.1: Effect of C-Rate on the surface strain behavior

The discussion above established a clear and strong correlation between the electrochemical reactions (or cell potential and the phase changes) and the surface hoop strain of the 18650 cell. Here the effect of the charge and discharge rates on the surface strain is presented. The hoop strain (from Gage 2) measured during various charge and discharge rates is shown in Figure 17a and Figure 17b, respectively. The overall trend of the strain remains unchanged with the C-rate, but the entire strain-potential curve shifts to right for higher charge rate (see Figure 17a) and it shifts to the left for higher discharge rates (Figure 17b). For example, the peak strain occurs at 4.05V during C/10 charge but shifts to 4.08V for C/5 charging. Similarly for discharge, higher C-rates shift the strain peak towards the lower cutoff potential, i.e., the peaks occur at 3.98V, 3.95V, 3.88V, and 3.78V for C/10, C/5, C/2, and 1C discharge rates, respectively. Table 3 shows the strain peak locations and cell temperatures at those peaks. As expected, higher C-rates lead to slightly higher temperature change of the cell which leads to slightly higher strain at any given potential; note that the magnitude of peak strain increases slightly with C-rate which is likely due to increased heat generation at higher C-rates.

Discharge Rate	Discharge Peak 4 (dQ/dV) Location (V)	Maximum Stain Location (V)	Maximum Strain (με)	Cell Temperature (°C)
C/10	4.05	3.98	533	25.5
C/5	4.02	3.95	576	26.0
C/2	3.95	3.88	582	27.8
1C	3.88	3.78	598	31.0

Table 3: Maximum strain locations at various cell discharge rates and corresponding temperatures.

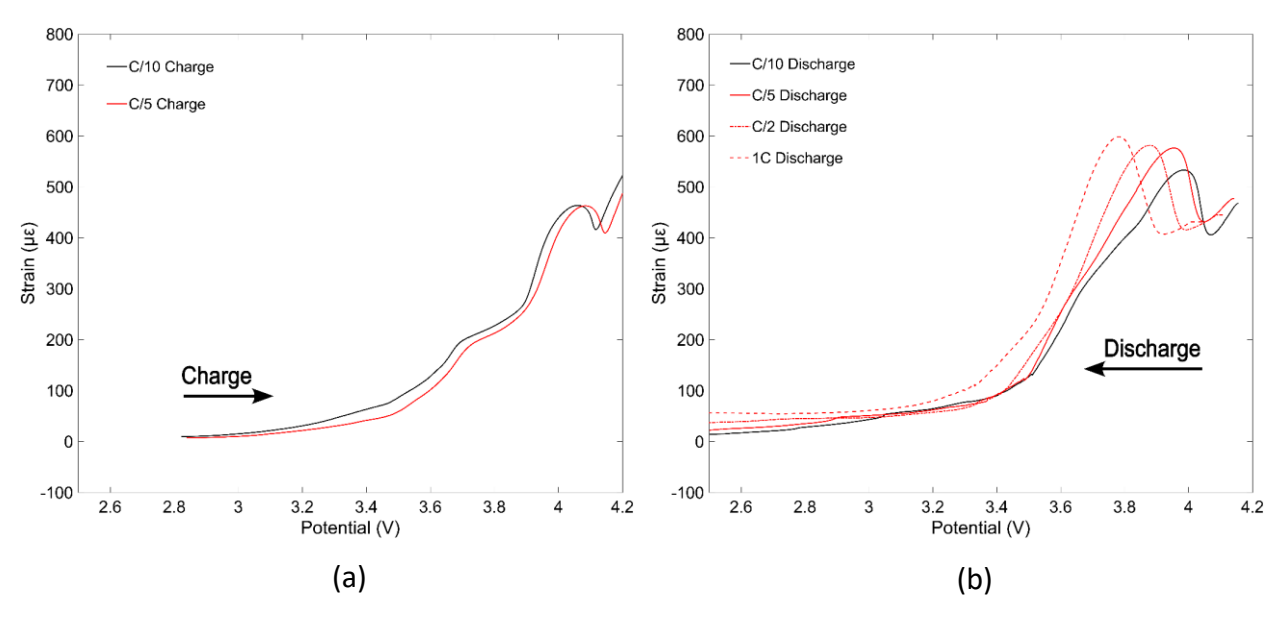


Figure 17: Strain ($\mu\epsilon$) vs. cell potential (V) for discharge rate experiments during (a) charge and (b) discharge.

2.6.2: Effects of C-Rate on dQ/dV and dε/dV peaks

Differential capacity analyses were also conducted on the cycling rate experiments to investigate the effects on the chemical reaction peaks. The dQ/dV behavior during charge is depicted in Figure 18a, and for discharge in Figure 18b. During charge, it can be seen that the dQ/dV peaks shift towards a higher potential during the faster C-rate. During discharge, the dQ/dV peaks shift towards a lower potential, reduce in magnitude, and broadens with higher C-rates. These trends on the dQ/dV peaks are consistent with other studies which attributed the peak broadening to relatively slower electrochemical kinetics compared to the applied current [20]. For example, the rate limiting process, in general, is solid-state diffusion of Li in the anode and cathode particles. As a result, a higher concentration of Li exists near the surface of the active particles during a higher C-rate lithiation, and vice a versa. The higher (lower) concentration will be reflected as higher (lower) potential for a given state of charge. In addition, a higher C-rate leads to a higher ohmic drop. The peak shift observed in Figs.6c and 6d can be attributed to a combination of these two effects.

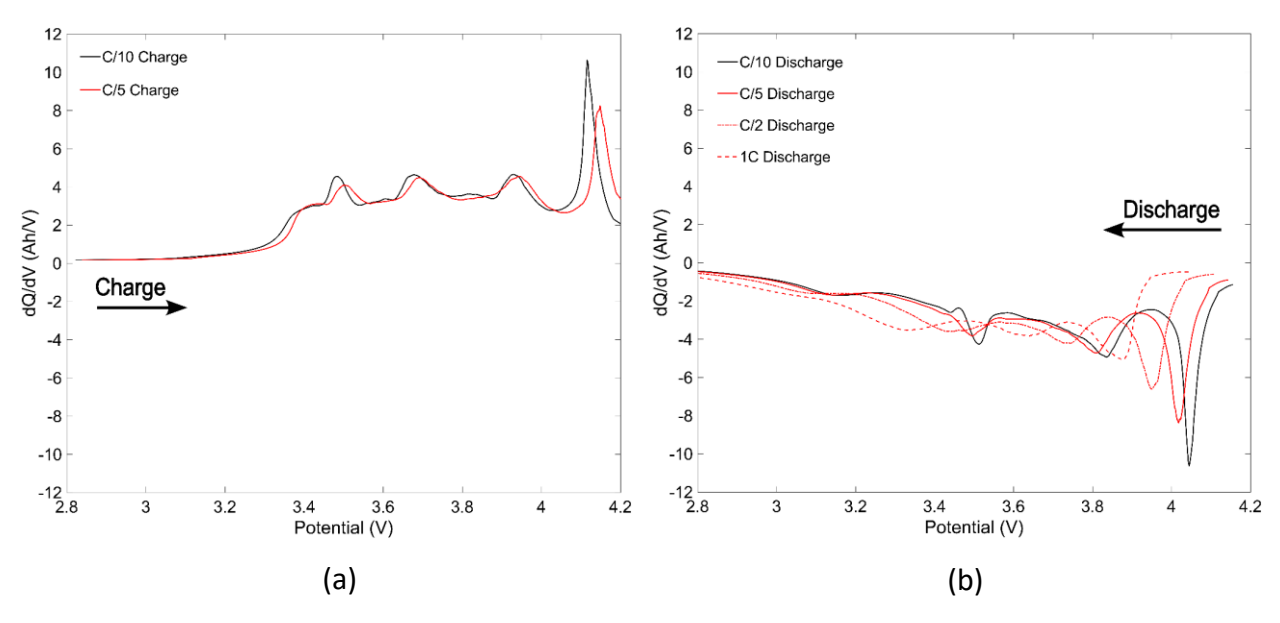


Figure 18: Differential capacity (dQ/dV) vs. cell potential (V) for discharge rate experiments during (a) charge and (b) discharge.

Since the volumetric changes of the active material are directly responsible for the strain behavior of the cell, Figure 19a and Figure 19b show that the peak shifting, reduction in magnitude, and broadening is seen in the $d\epsilon/dV$ peaks as well. During charge the differential strain peaks shift towards a higher potential and broaden. The peak near 3.93V (for C/10) shifts to 3.96V and reduces in magnitude, while the magnitudes of the other peaks remain fairly consistent. During discharge, all peaks shift towards a lower potential and broaden as well. The positive $d\epsilon/dV$ peak near 4.04V (at C/10) shifts to 4.01V, 3.94V, and 3.85V for C/5, C/2, and 1C discharge protocols, respectively. This peak reduces in magnitude and broadens with every shift to a lower potential. The negative peak at 3.88V (for C/10) also shifts to a lower potential but becomes more negative. The locations for this peak during C/5, C/2, and 1C discharge protocols are 3.84V, 3.70V, and 3.64V, respectively. This behavior mirrors that seen in the dQ/dV analysis.

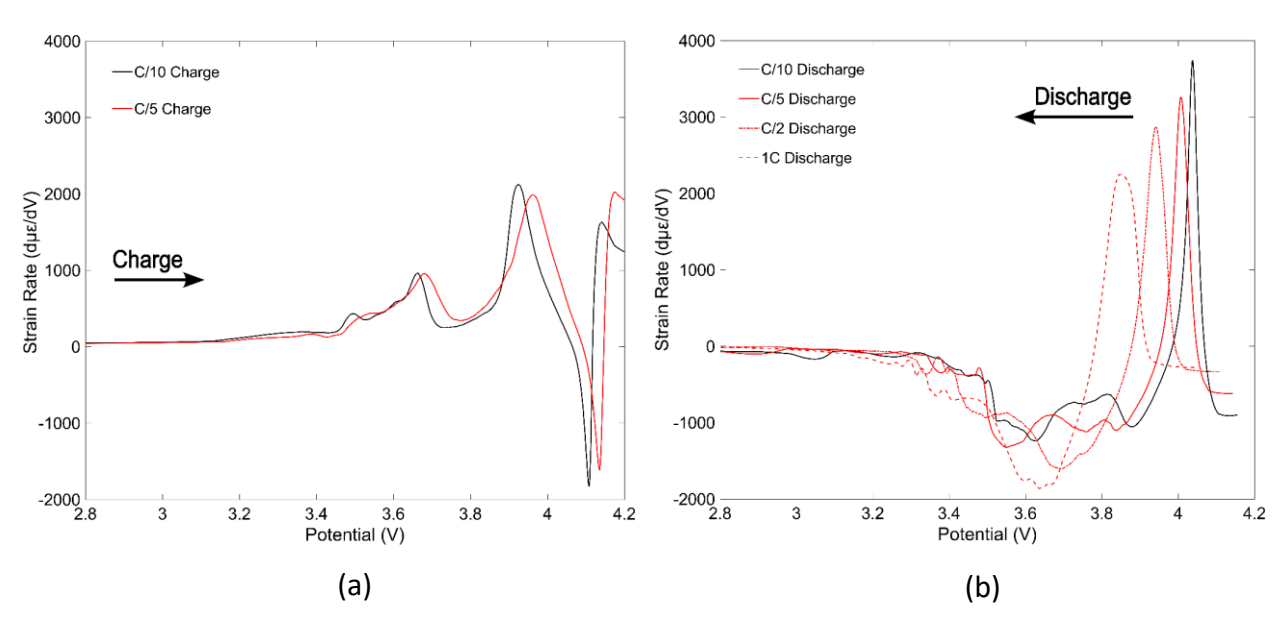


Figure 19: Differential strain ($d\epsilon/dV$) vs. cell potential (V) for discharge rate experiments during (a) charge and (b) discharge.

CHAPTER 3: STRAIN BEHAVIOR DURING OVERCHARGE AND HEATING TO THERMAL RUNAWAY

In this chapter, the utility of strain measurement to track cell degradation during overcharge and predict current interrupt device (CID) activation is evaluated. Two main overcharge scenarios are tested here: overcharge until CID activation, after which cell were heated to TR, and repeated overcharge until 105% and 110% of nominal capacity. Results from ICA and EIS analyses support the insights into cell degradation gained from strain analysis, confirming the validity of strain-based battery health monitoring. The conclusions from this work could be extremely useful for systems in which the possibility of thermal runaway is unacceptable – such as aircraft, ocean vessels, and space systems.

3.1: Overcharge to CID Activation Experiments

3.1.1: Experimental Setup and Procedure for Overcharge to CID Activation Experiments

The overcharge experiments were conducted in a custom-build blast enclosure for abusive battery testing with dimensions of 16x8x8 ft at NSWC Carderock to contain a possible thermal runaway event. As a result, a slightly different setup from that of Figure 5 was used in these experiments. Strain, temperature, cell potential (V) and current (A) were collected using an Agilent DAQ. As this DAQ did not have a similar capability to the one used for baseline experiments, quarter bridge completion modules (BCM's) were used, which received 10V excitation from a dedicated power supply, to collect strain data. A voltage output was collected from the BCM's, which was converted to strain. A wiring schematic for a BCM, which was needed for each strain gage grid, is shown in Figure 20 below. The excitation voltage (10V DC) was supplied through the "EX+" and "EX-" lines, which connected to the strain gage through the wires labeled "SG Leg 1" and "SG Leg 2." The output voltage from the strain gage measurement circuit was read through the wires labeled "SG- Signal" and "SG+ Signal." To convert the voltage output to a stain reading, Equation 1 below was used:

$$\varepsilon = \frac{(\gamma * R_2 + (\gamma - 1)) * R_{G,0}}{(1 - \gamma) * R_{G,0} * GF}; \qquad \gamma = \frac{V_{meas}}{V_{in}} - 0.5,$$

Equation 1

Where R_{G,0} is the resistance of the strain gage at the start of the experiment, R₂ the

resistance of the bridge completion resistor (350 Ω), GF the gage factor, V_{in} the excitation voltage (10V), and V_{meas} the output voltage of the BCM measured by the DAQ, respectively.

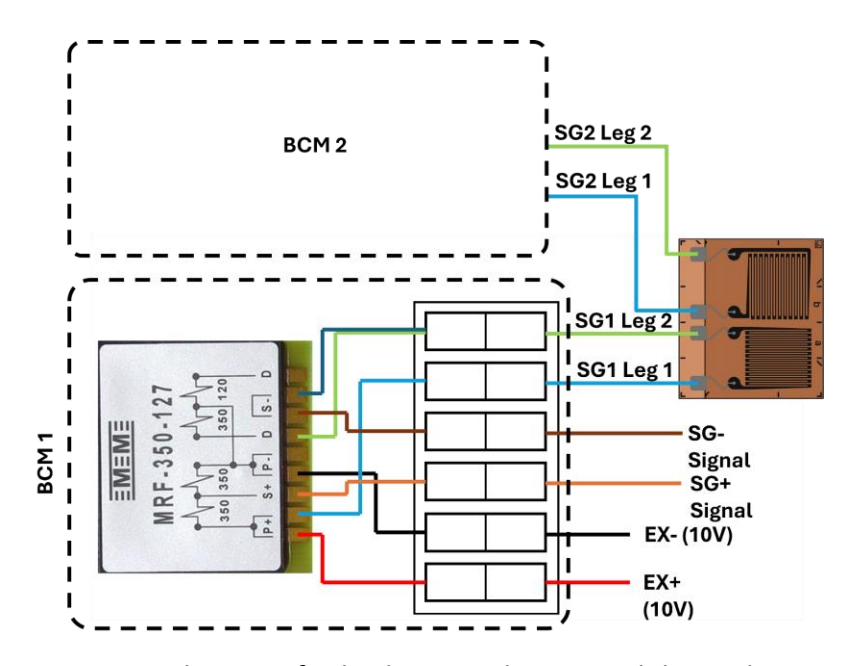


Figure 20: Wiring schematic for bridge completion modules and strain gages.

To ensure that the setup with BCM's was wired correctly, cells with a known strain behavior were cycled using a Gamry potentiostat inside a Tenney TJR environment chamber. The cells were cycled at a C/5 rate, and the measured strain behavior (which is discussed in more detail in chapter 3.2) was compared to that recorded at MSU. The strain recorded using the setup at NSWC Carderock closely matched the one recorded at MSU, signifying that the BCM's were wired correctly, and the strain equations used to convert the voltage output to strain were implemented without error.

The first set of OC experiments was performed to determine the strain state of a battery as it is overcharged to failure – CID activation, venting, or TR. To accomplish this, a power supply was used to prescribe a potential and current to charge cells at a C/5 rate from 2.5V to failure. The region between 2.5A and 4.2V is within the normal operation window of the cell. The start of the electrical abuse experiment was marked by the cell's potential exceeding 4.2V, which continued at a C/5 rate until CID activation at approximately 5V. An Agilent DAQ was used to collect test data (ambient and cell temperature, cell potential, charge current, and strain) during the overcharge experiment. The cells were then given a rest period to determine how much strain

relaxation occurred after CID activation and were then heated to TR using a heating pad.

3.1.2: Verification of Cell Cycling Setup at NSWC Carderock

To ensure that the strain measurement setup was wired correctly and the equations to convert the voltage output to strain readings were implemented correctly, a cell with known strain behavior was cycled galvanostatically at a C/5 rate. The comparison between the strain behavior collected at MSU and NSWC Carderock can be seen below in Figure 21. The main difference between the two measurements is the state of axial strain, which is tensile during experiments performed at MSU and compressive during those performed at NSWC Carderock. It is important to note that this was not the case with all cells – the strain state in the axial direction rarely differed in measurements conducted at Carderock vs. those gathered at MSU. Also, strain measurements in the axial direction did not provide consistent results, even in the same cell, as discussed in chapter 3.1.3. Strain in the hoop direction at the center of the cell remained reliable, however, and was used to perform all strain-related analysis for the abuse tests. It can be seen in Figure 21 that the magnitude and overall behavior of the hoop strain recorded using the setup at NSWC Carderock closely matched the one recorded at MSU, signifying that the BCM's were wired correctly, and the strain equations used to convert their output to strain were implemented without error.

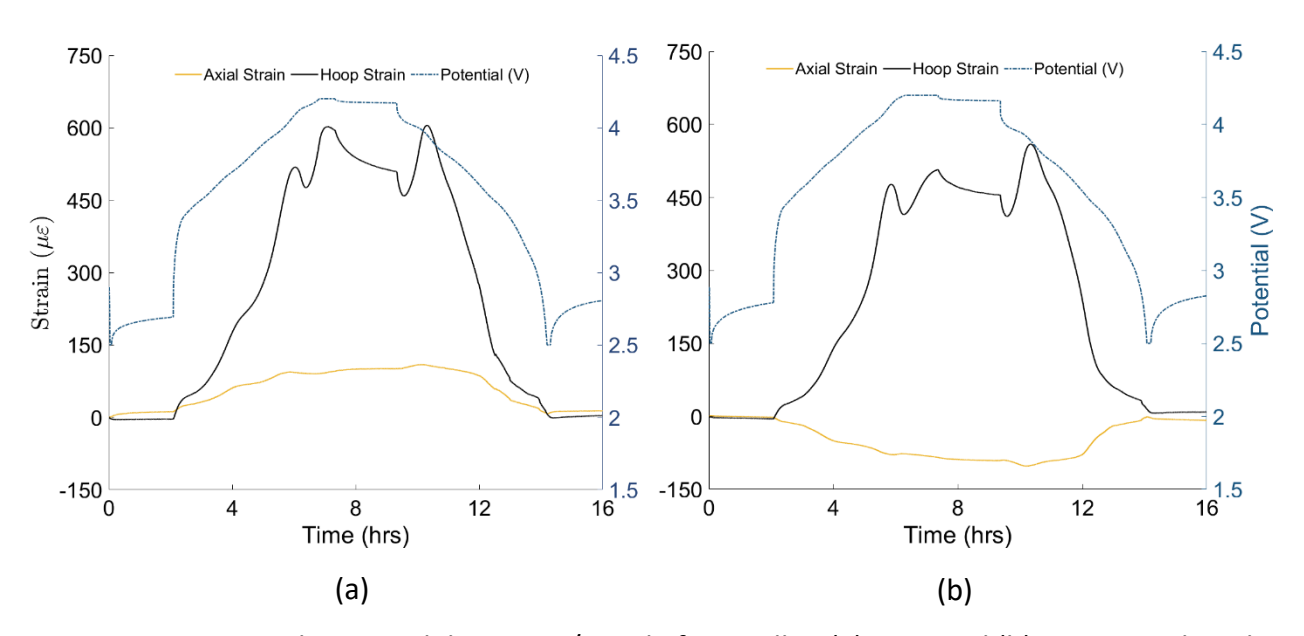


Figure 21: Strain and potential during a C/5 cycle for a cell at (a) MSU and (b) NSWC Carderock.

3.1.3: Surface Strain Behavior During an Overcharge Process

The discussion above shows that the surface hoop strain correlates remarkably well with the electrochemical reactions and the associated phase changes in the electrodes. One can take advantage of this aspect, and any deviation of the strain signal (from that of Figure 13a) can be considered as an indicator that can be used to identify unwanted chemical reactions or physical changes that occur in the cell. An abuse test was conducted where a cell was overcharged at a C/5 rate until CID activation. The purpose of this test was to determine if strain signal provides any additional insights on the processes that occur during the overcharge process and how this affects the magnitude of the strain. Figure 22 shows that the hoop strain (from Gage2 of Figure 6) increases rapidly during overcharge, i.e., after 100% state of charge indicated by a vertical dashed line. A maximum value of 1634 $\mu\epsilon$ was recorded at the moment of CID activation, which is 2.54 times the strain at 100% SoC. A rapid increase in temperature was also observed during overcharge despite the relatively low C/5 rate; however, the ΔT of 14 °C that occurs during the overcharge contributes an estimated 140 $\mu\epsilon$ of the strain due to temperature change. The large additional strain can be attributed to a combination of volume changes of particles and gas generation inside of the sealed cylindrical cell. When the gas pressure inside the sealed cell reaches a critical limit, it triggers the CID activation, which occurred in the present cell at 3.95 Ah, which is nearly 16% over the nominal capacity. Wang et al. [87] reported a detailed analysis on the overcharge behavior of NMC811 vs. graphite pouch cells, which contain no CID and therefore underwent thermal runaway after 30% overcharge (or 130% SoC). They also observed significant swelling of the NMC811 vs. graphite pouch cells beginning at 4.68 V which was attributed to gas buildup in the cell.

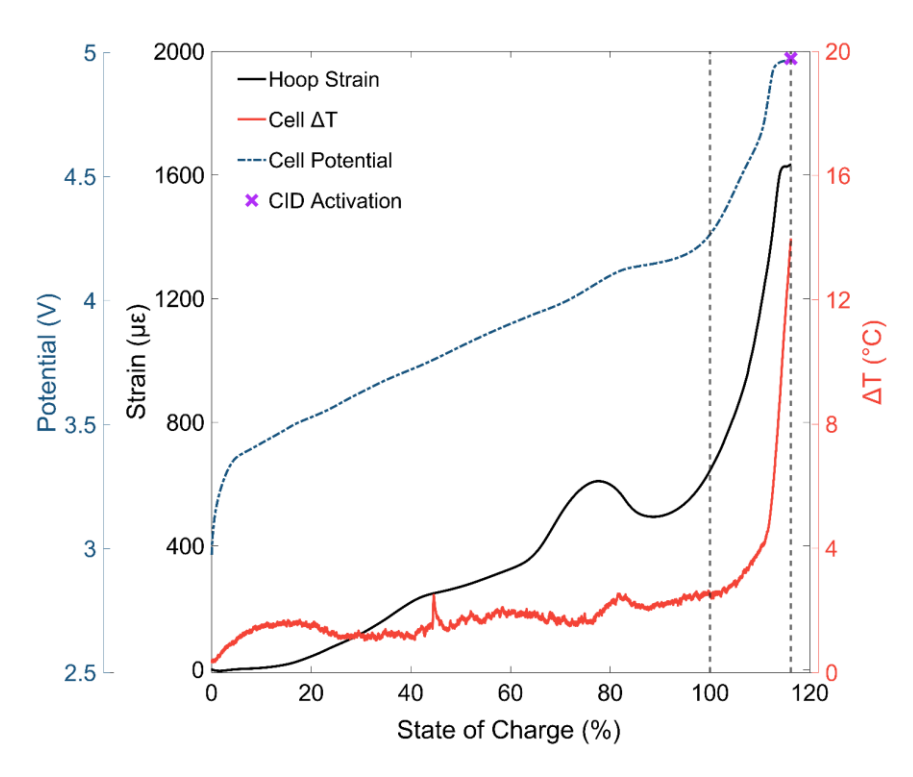


Figure 22: Hoop strain (from Gage2), cell potential, and temperature behaviors during overcharge abuse test.

Gas generation occurs due to decomposition of the electrolyte, which is expected to rapidly increase above the manufacture specified upper voltage limit of 4.2 V. A plateau observed in Figure 22 in both voltage and strain, moments before CID activation, strongly suggests the onset potential of an electrochemical reaction such as electrolyte oxidation or plating of Li metal on the anode surface. Plating of Li metal would also result in the chemical decomposition of the electrolyte during the formation of an SEI layer. At much higher potentials, oxygen release from Ni-rich layered oxide cathodes is also possible. The reactions between oxygen and other electrolyte decomposition products are strongly exothermic and generally leads to thermal runaway. Thermal runaway was not observed during overcharge of the 18650 cells in this study, because the pressure buildup due to above mentioned possible gas generation reactions reached a critical level to activate CID which prevented thermal runaway.

At 4.2V (or at 100% SoC) the hoop strain of the cell was 644 $\mu\epsilon$ (regarded as 100% for the following comparisons) and increased to 1634 $\mu\epsilon$ (2.54 times) at CID activation. By assuming the cylindrical cell as a pressurized cylinder, one can make some interesting observations. For example, the total amount of strain generated (not related to temperature change) during

overcharge (i.e., from SoC >100%) was 875 με. This level of hoop strain correlates to 3.98 MPa of pressure acting on the internal surface of the cell casing at CID activation. It should be noted that the CID-activation pressure at room temperature were reported [88,89] to be approximately 1.3-1.4 MPa for NMC811-graphie cylindrical cells. The estimate based on simple rudimentary pressure vessel-based model is in the ballpark but slightly higher due to following reasons. First, the thermal strain estimates were based on room temperature thermal expansion measurements which are clearly different from the temperatures observed during the overcharge conditions. Also, the simple assumption ignores the fact that jelly roll could continue to expand beyond 100% SoC providing the additional contact pressure that accounts for the remaining pressure. This implies that additional mechanisms other than gas generation contribute to the strain evolution during overcharge. While further study is needed to decouple the phenomena contributing to the observed strain behavior, it is clear that strain measurements can provide valuable information on the physical state of the cell. The strain signal can provide additional valuable information quickly and in a fairly inexpensive way that could complement voltage, temperature, and other sensing techniques in identifying the state of a cell.

3.1.4: Surface Strain Behavior of Overcharged Cells During Heating to Thermal Runaway

The objective of these experiments was to characterize strain behavior of the previously overcharged cells during heating to TR. Overcharged cells behave differently from healthy cells during this type of failure, therefore these results are generally not comparable to studies performed on healthy cells. For example, Mier et. at. [2022] reported vent activation between 138°C and 151°C for healthy cells heated to TR, compared to the 86°C to 92°C recorded during the experiments at NSWC Carderock. As stated in the previous section, further study is needed to fully understand strain evolution during overcharge and the quantify the gas generation. Nevertheless, analyzing the strain behavior of an overcharged cell during heating can still prove to be important. When a cell's CID activates, it becomes electrically inert, and cannot provide a voltage or current signal. Hence, a BMS cannot infer the internal state of such a cell. In such a case, strain measurement could prove to be a valuable tool to monitor a cell and be able to identify when it poses a threat.

Figure 23 below shows the strain behavior of the overcharged cell #3 (which used a high

temperature epoxy, capable of withstanding 200°C before burning off, to bond strain gages) during heating to thermal runaway. From data listed in Table 4, it is seen that strain decreased by 291 µɛ during the rest period after CID activation. As the heating begins, the shape of the strain follows that of the cell temperature, signifying that initially the strain increase is purely thermal. The strain increases linearly between 2 and 5 minutes, after which the slope decreases, and the strain reaches a maximum value at 6 minutes and 59°C. While the time to maximum strain and its magnitude are different for cell 1 and 2, the temperature at the maximum strain for those cells was comparable at 72.3°C and 59°C, respectively, as shown in Table 4. The strain begins to decrease after 6 min until there is a sharp drop in strain, marking the activation of the vent safety device. It is worth noting that the vent activated at a similar temperature for all 3 cells in the experiments performed. The strain decreases at a faster rate after vent activation, until the strain behavior shows a jump as the cell goes into TR. Another interesting point is that the TR initiation temperature for all 3 cells was consistent at 139°C - 149°C. The separator is known to melt at 130°C and above, which is consistent with the TR initiation temperatures seen in these experiments.

Cell	Strain After Rest	Max Strain (TR)	Temp. at Max Strain	Temp. at Vent Activation	Temp. at TR Initiation
1	1013 με	1212 με	72.3°C	88.8°C	149.0°C
2	1497 με	1474 με	59.0°C	91.8°C	139.5°C
3	951 με	1186 με	59.0°C	85.9°C	145.7°C

Table 4: Strain and temperature points of interest during thermal runaway experiments.

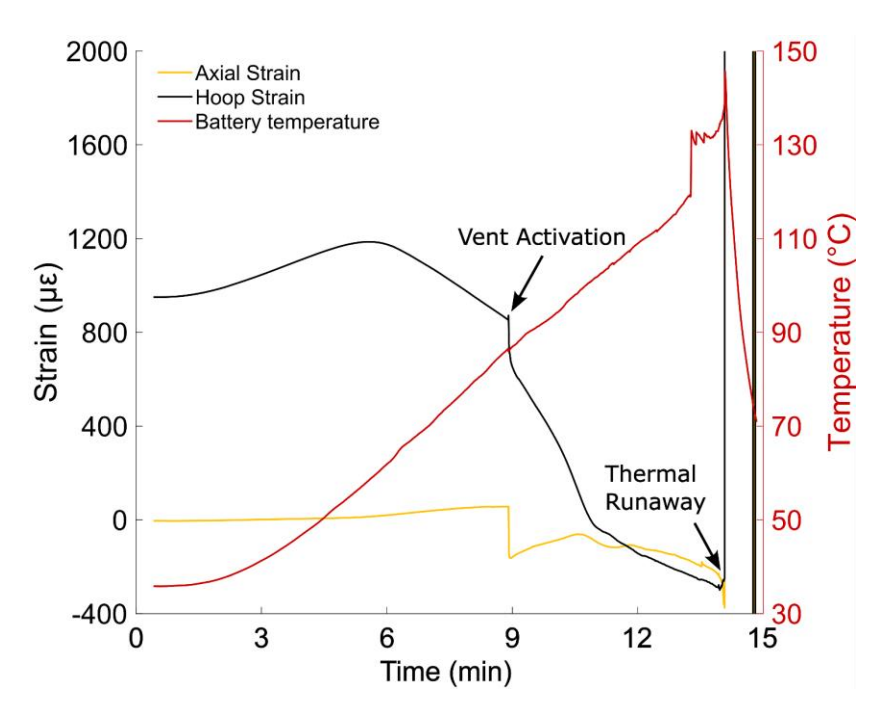


Figure 23: Strain and temperature behavior of an overcharged cell during heating to thermal runaway.

As mentioned previously, the quantitative results from the TR experiments are not directly comparable to other studies where healthy cells are heated. The qualitative results from this study are still valuable, however. The vent activation event is clearly detectable through strain measurements, which is an important indicator which points to cell abuse or damage. If implemented in a practical setting, such an indication may be able to provide the valuable time needed to prevent a TR event.

3.2: Repeated Overcharge Experiments

3.2.1: Experimental Setup and Procedure for Repeated Overcharge Experiments

During the work completed to quantify the strain behavior at normal cycling conditions it was determined that the strain in the hoop direction was consistent, while strain in the axial direction varied. For this reason, axial stain data was used to correct for transverse effects in the hoop strain data [90] using Equation 2 below:

$$\varepsilon_b = \left(\frac{1 - \nu K_b}{1 - K_b^2}\right) (\hat{\varepsilon}_b - K_b \hat{\varepsilon}_a)$$

Equation 2

Where ε_b is the true value of principal strain in the hoop direction, ν is the Posson's ratio of the cell casing (steel), K_b is the transverse sensitivity in the hoop direction, $\hat{\varepsilon}_b$ is the measured strain in the hoop direction, and $\hat{\varepsilon}_a$ is the measured strain in the axial direction. Hence, only the corrected hoop strain data (ε_b) was used for analysis and to create plots.

The overcharge experiments were conducted in a custom-build blast enclosure for abusive battery testing with dimensions of 16x8x8 ft at the Naval Surface Warfare Center Carderock Division to contain a possible thermal runaway event. For this reason, a combination of power supplies and loaders was implemented to charge and discharge cells. An Agilent DAQ system was used to record all test data, including BCM output, excitation and battery voltages, applied current, and cell and ambient temperatures. Agilent switch cards, relays, and an Arduino microcontroller were used to create cycling scenarios.

3.2.2: Repeated Overcharge Cycling Conditions

In the previous section cells were overcharged until CID activation, which occurred at 117±3% nominal capacity (17±3% overcharge). To explore how cell behavior is affected by comparatively mild overcharge, two scenarios were chosen: repeated overcharge to 105% and 110% of nominal capacity. Each cell was first cycled between 2.5 and 4.2V with 100 mA cutoff using a Gamry potentiostat inside a Tenney Jr (TJR) temperature chamber set to 23°C to avoid effects due to ambient temperature fluctuations. The recorded cell potential, strain, and temperature were used as a baseline for the overcharge experiments. An average value for the nominal cell capacity was then determined and used to calculate a capacity that each cell would be overcharged to for the selected scenario. The cells were then moved into the blast enclosure for the overcharge experiments, which did not have ambient temperature control. As a result, the ambient temperature during the overcharge experiments varied between 24°C and 32°C.

During the first scenario a cell was repeatedly overcharged to 105% SoC (approximately 3.57Ah), which will henceforth be referred to as 5% overcharge (OC). The goals of this scenario were to determine if a mild 5% OC was enough to generate irreversible strain and whether the OC cycles had cumulative effects (e.g., if two 5% OC cycles were comparable to one cycle where a cell was overcharged to 110% SoC). The cycling procedure for the first scenario consisted of a galvanostatic charge at 0.7A to 105% SoC, followed a 2 hour OCP rest step, then a galvanostatic

discharge at -0.7A to 2.5V, followed by another 2 hour OCP rest step. This was repeated for 3 cycles at a time, for a total of 12 cycles. During the second scenario, a total of four cells were repeatedly overcharged to 110% SoC (approximately 3.74 Ah), which will henceforth be referred to as 10% OC. The cycling profile was identical to the 5% OC scenario, with the exception of the cutoff capacity. The cells were also characterized using electrical impedance spectroscopy (EIS) before any abuse cycling was done and after every three 10% OC cycles. Additionally, a fifth cell was subjected to six 10% OC cycles, after which it was discharged to 0% SoC and disassembled inside of an argon-filled glovebox to analyze the electrodes and current collectors.

3.2.3: EIS Procedure and Parameterized Equivalent Circuit

EIS analysis was performed on cells subjected to the second overcharge condition (i.e., 10% OC) at 23°C inside a Thermal Product Solutions Tenney JR temperature chamber using a Gamry Reference potentiostat. The cells were charged to 4.2 V with 100 mV cutoff, held at OCP for 2 hours, discharged to 50% SoC, and held at OCP for 4 hours before conducting the EIS measurement. The frequency range used was 1 KHz to 0.1 Hz. Most cells failed during the 9th or 10th cycle, therefore EIS data presented in this publication is limited to cells which underwent no abuse cycles (fresh), three 10% OC cycles, and six 10% OC cycles. The parameterized equivalent circuit used for modeling the EIS behavior is shown in Figure 24 below. The inductive behavior and contact resistances of the cell, which are collected at high frequencies, are represented by the inductor (L1) and resistor (R2), respectively. The first resistor/constant phase (R3/CPE3) element is used to model the solid electrolyte interface (SEI) arc behavior of EIS data, and the second (R4/CPE4) is used to model the charge transfer arc. The diffusion behavior present at low frequencies is modeled by the Warburg element labeled W5. Taking into account the diffusion coefficients of the electrodes and the minimum frequency, the infinite Warburg element is applicable for diffusion thicknesses greater than 2 µm. The spacing between electrodes and the anode active material particle sizes exceed this value, hence the low frequency behavior can be modeled by an infinite Warburg element.

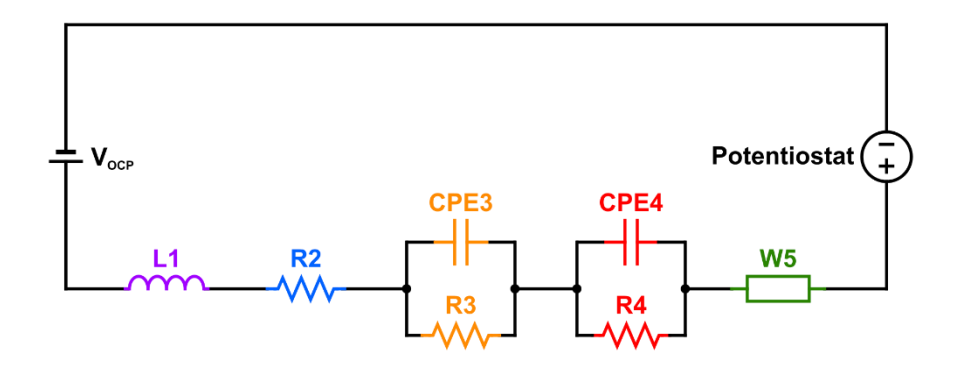


Figure 24: Equivalent circuit model of a cell.

3.2.4: Repeated Overcharge Behavior

The first abuse scenario performed was 5% OC. Figure 25a shows the cell potential, temperature (compared to ambient), and hoop strain during a baseline cycle (with 4.2V, 100 mA cutoff). Figure 25b shows the cell potential, temperature (compared to ambient), and hoop strain of the same cell during a 5% OC cycle. In Figure 25b, the hoop strain signals from both rosettes are shown to demonstrate the slight variability of measurement, even on the same cell, yet an overall similar strain profile. Hence, only the hoop strain from one rosette is shown for the remainder of this work. During overcharge the potential reaches a peak value of 4.44 V, and hoop strain a peak of 408.1 με, which is 1.16 times the peak strain values measured during normal cycling (at 4.2 V) after compensating for thermal strain [60]. The comparison of peak strains during normal and 5% OC cycling, including compensation for strain due to cell heating (ε_{Therm}) is shown in Table 5 below. Strain and potential relaxation is observed during the rest step at open circuit potential (OCP), which is consistent with the previous work [60]. Finally, strain is seen to return to a near zero state at the end of discharge and during the following rest step, signifying that irreversible reactions during a 5% OC are minimal. The peak temperature change with respect to ambient (ΔT) recorded during the overcharge step was 5.5°C, while the overall maximum temperature change with respect to ambient was 6.6°C.

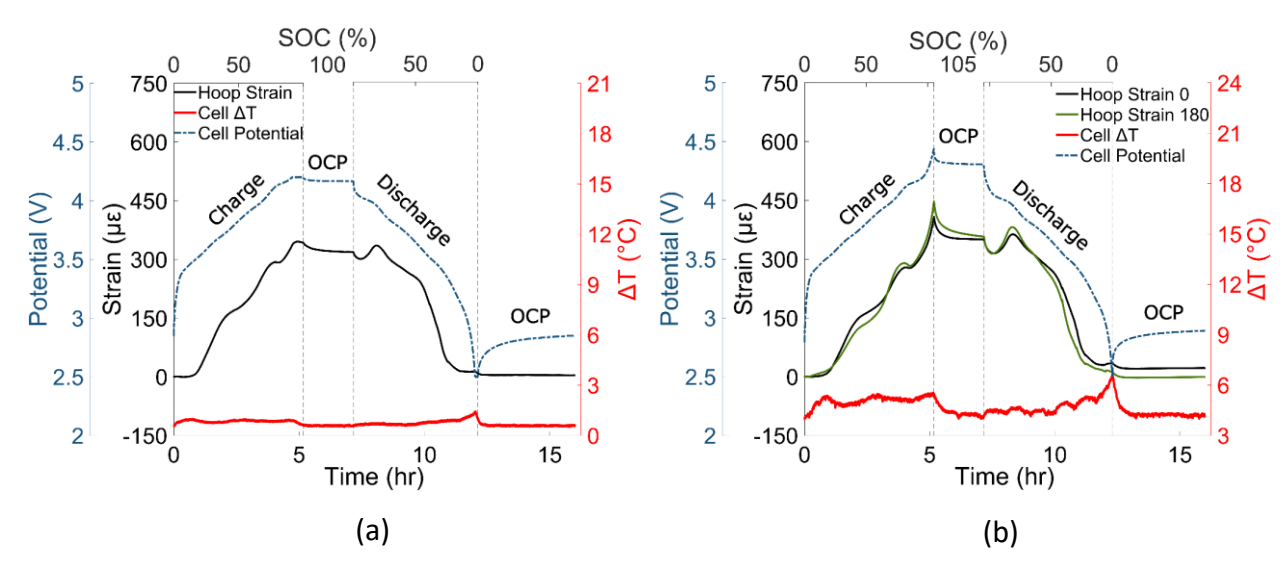


Figure 25: Hoop strain (compensated to transverse effects), temperature change, and cell potential during galvanostatic cycling with (a) normal 4.2V cutoff, and (b) 5% OC cutoff.

A representative comparison between normal and overcharge cycling is shown in Figure 26a and Figure 26b as well, where the former is the baseline behavior of a cell which is later subjected to 10% OC shown in the latter. During the first 10% OC cycle shown in Figure 26b the potential reaches a maximum value of 4.69 V, and the hoop strain a maximum value of 1276.3 $\mu\epsilon$, which is 1.62 times the peak strain during normal cycling (at 4.2 V), after compensating for strain due to cell heating, as shown in Table 5. Both of these values are higher than those seen during the 5% OC cycle. The strain state returns to near zero by the end of the rest period (OCP step) after discharge, though is slightly higher than after the 5% OC cycle. The peak temperature change with respect to ambient (Δ T) during the overcharge step was 6.6°C, which is also higher than the temperature change seen during the 5% OC step shown in Figure 25b. The overall maximum temperature change of 7.4°C above ambient was observed during the discharge step, which is higher than during the 5% OC cycle.

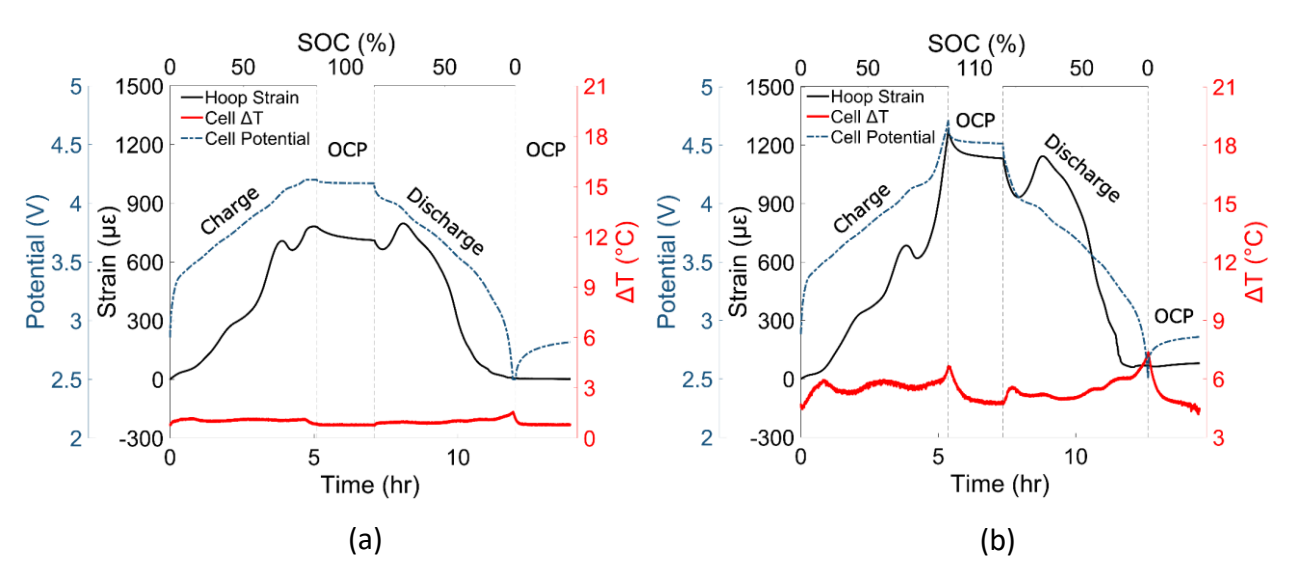


Figure 26: Hoop strain (compensated to transverse effects), temperature change, and cell potential during galvanostatic cycling with (a) normal 4.2V cutoff, and (b) 10% OC cutoff. Both strain and potential reach a higher maximum value than during 5% OC.

OC Level	Nominal strain (at	Nominal strain (no	Maximum strain	Maximum strain (no	Normalized max. strain (no
	4.2V)	ETherm)		E _{Therm})	ε _{Therm})
5% OC	345.4 με	343.0 με	408.1 με	396.3 με	1.16
10% OC	780.4 με	777.6 με	1276.3 με	1260.1 με	1.62

Table 5: Strain comparison between baseline and the first overcharge cycle.

The full cycling profile for the 5% OC experiment is shown in Figure 27a, and for a representative 10% OC experiment in Figure 27b. It can be seen that the maximum strain, maximum potential, and temperature change all increase for both 5% OC and 10% OC cycling. While the increase is slight during 5% OC cycling, it is much more prominent during the 10% OC cycling. The maximum temperature is also seen to increase greatly during 10% OC cycling, especially after the 3rd cycle. It can be seen that during 10% OC cycling the CID activation occurs during the charge step of the 10th cycle. The strain is seen to retain a non-zero value at the end of overcharge cycles — a phenomenon which is more prominent in the 10% OC experiments. Henceforth, this non-zero strain at the end of a cycle will be referred to as residual strain. As seen in Figure 27a and Figure 27b, the residual strain at the end of a 10% OC cycle has a greater magnitude than at the end of a 5% OC cycle. An interesting observation for both 5% and 10% OC cycling is that hoop strain continues to increase after the usual 4.2V cutoff, and mostly recovers

after the discharge to 2.5V. The implications behind this observation are related to the electrochemical reactions occurring within the electrodes and will be discussed in section 3.2 of this publication.

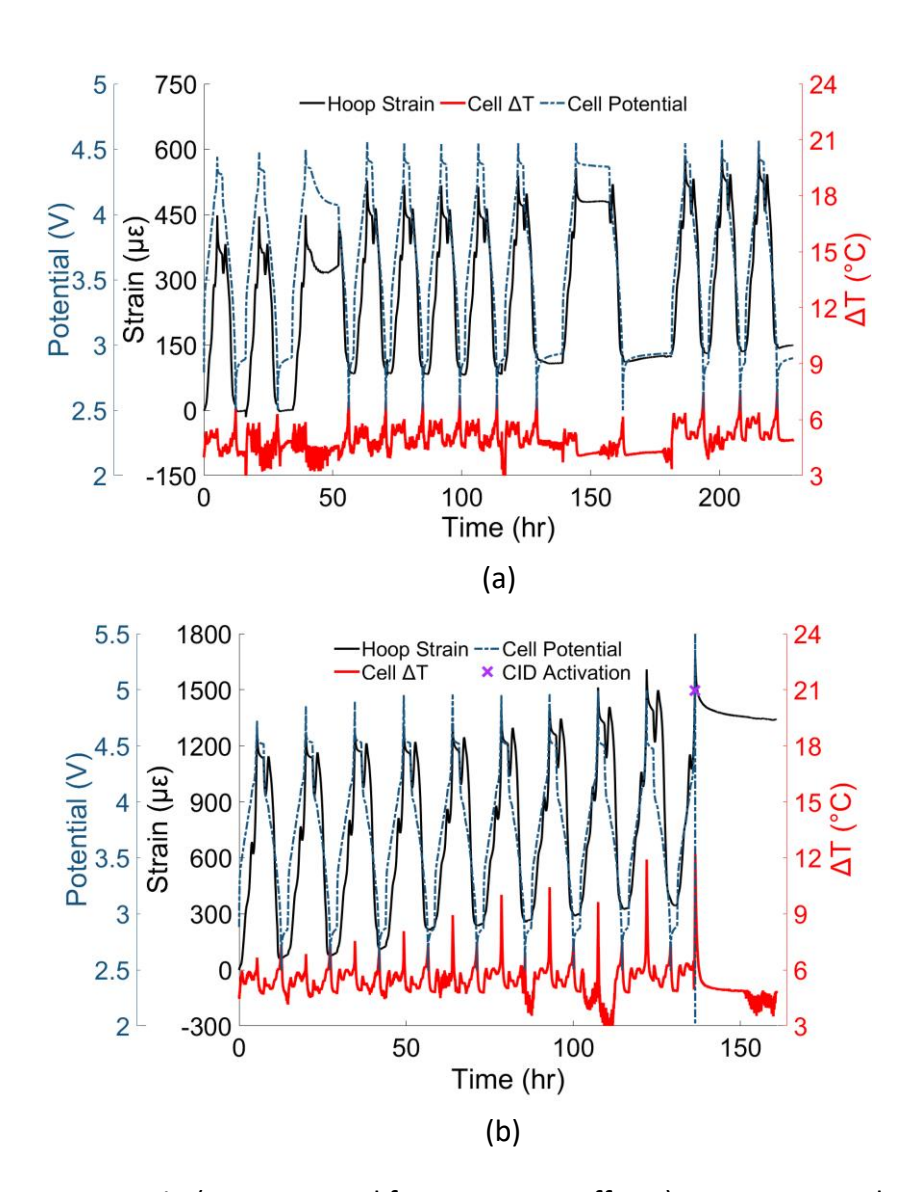


Figure 27: Hoop strain (compensated for transverse effects), temperature change, and potential during (a) repeated 5% OC and (b) repeated 10% OC cycling. Maximum potential, strain, and temperature change increase slightly during every 5% OC cycle, and significantly during every 10% OC cycle, with CID activation during the 9th 10% OC cycle.

The cycle details for the 10% OC experiment are shown below in Figure 28. Strain and cell potential profiles for each cycle versus time – consisting of a 10% overcharge, 2 hours rest at OCP, and discharge to 2.5V steps – is shown in Figure 28a. It can be seen that although the magnitude

of the hoop strain continues to increase, the overall trend remains the same. This overall increase in magnitude is related to irreversible reactions, such as internal gas generation, occurring within the cell, which manifest physically as the residual strain at the end of each cycle. The largest increase in residual strain is seen to occur between the first and second cycles, which is due to the residual strain rise at the end of the first cycle. From the second cycle onwards, the increase in both the total magnitude of the hoop strain and residual strain are steadier compared to the 1st to 2nd cycle. The CID safety mechanism is activated by the buildup of internal pressure. Hence, the residual strain at the end of the last cycle prior to CID activation is likely the closest representation to the pressure buildup within the cell without the added effects of the volumetric changes in the active material.

Figure 28b shows the maximum hoop strain and potential for each cycle, which both occur at the end of the overcharge step, as well as the cycle efficiency. While both the maximum hoop strain and cell potential steadily increase during 10% OC cycling, the cell efficiency shows a different trend. During the 2nd through 4th cycles, the cell efficiency is at least 99.5%, which implies that irreversible processes are using a relatively small amount of energy (compared to subsequent cycles). From the 5th cycle onwards the cycle efficiency decreases, reaching a minimum of 98% prior to the last cycle during which the CID activates. This implies that from the 5th cycles onwards, the irreversible phenomenon occurring inside the cell is exacerbated by the cumulative effects of the previous overcharge events.

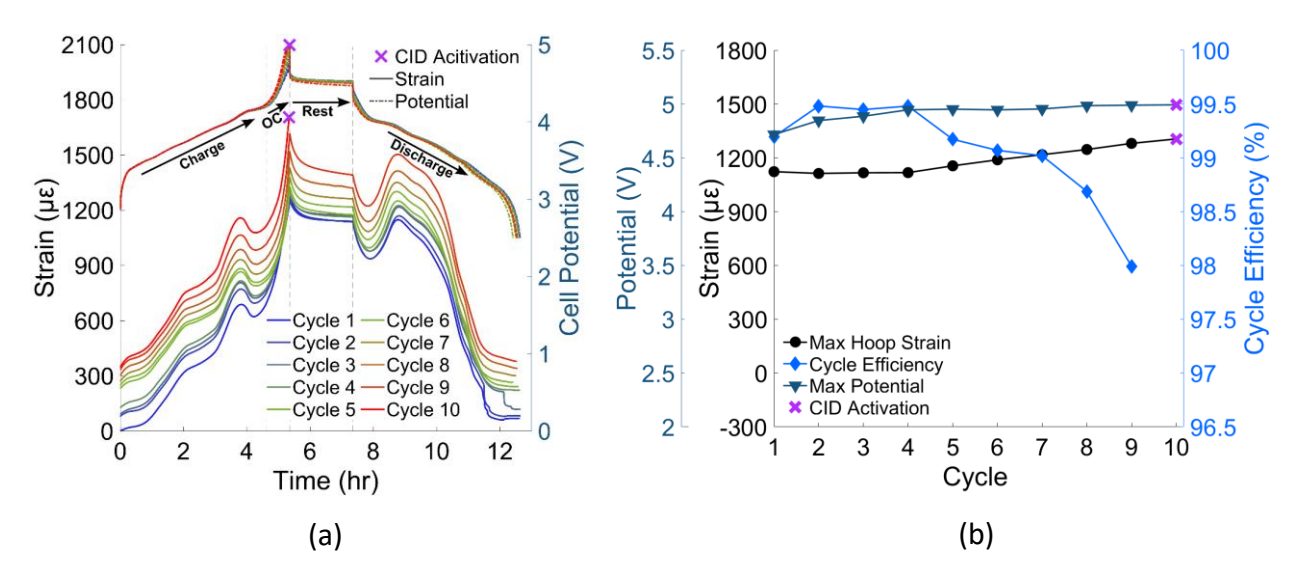


Figure 28: (a) Hoop strain vs. time profile for each 10% OC cycle, showing a similar trend between cycles with a steady increase in magnitude. The residual strain at the end of each cycle is also seen to increase. (b) Maximum hoop strain, potential, and cycle efficiency for each 10% OC cycle, showing a steady increase in both maximum strain and potential, and a drastic decrease in cycle efficiency, especially after the 4th cycle. The magenta "X" marks in both figures indicate the CID activation event, which occurred during the 10th cycle for this sample.

The experiment results for all of the 10% OC experiments are shown in Table 6 below. It can be seen that the maximum temperature change (11.39±0.50°C) and potential (5.01±0.01 V) are also consistent and occur during the last cycle immediately before CID activation. Although the magnitude of the strain varies between cells, the results are fairly consistent for both the normalized maximum strain (1.73±0.10) and residual strain (220±53 μ E) values. The normalized strain values have been compensated for temperature effects using the Δ E/ Δ T = 7.5 μ E/°C, as measured in the previous work [60].

The residual strain at the end of every cycle can be a useful metric. If the 18650 cell is analyzed as a simple pressurized cylinder, 220 \pm 53 µ ϵ in the circumferential (hoop) direction correlates to 1 \pm 0.24 MPa of internal pressure. The published values for CID activation pressures are 1.058 \pm 0.053 MPa at room temperature and 0.920 \pm 0.076 MPa at 100°C for a cap design similar to the cells used in this study [10]. The calculated internal pressure from the residual strain matches closely to the published CID activation values.

Cell	Nominal Strain (at 4.2V)	Maximu m Strain (at CID)	Last Cycle Residual Strain	ΔT at CID (°C)	Normalize d max. strain (no ε _{Therm})	Maximum Potential (at CID)	No. of full cycles before CID
1	691 με	1337 με	301 με	11.29	1.81	5.02	9
2	769 με	1298 με	180 με	11.66	1.57	4.99	10
3	393 με	796 με	232 με	10.63	1.82	5.02	15
4	445 με	841 με	168 με	11.98	1.69	5.00	9
Mean	574 με	1068 με	220 με	11.39	1.73	5.01	11
St. Dev.	159 με	250 με	53 με	0.50	0.10	0.01	2

Table 6: 10% OC test results for all 4 samples.

3.2.5: Incremental Capacity and Strain Analysis of Repeated Overcharge

A variety of analyses were conducted to determine the underlying mechanisms responsible for the maximum strain increase and residual strain buildup during repeated overcharge cycling. The first of these was the incremental capacity analysis (ICA), as shown in Figure 29a, which uses a differential of the cell's capacity (Q) with respect to the cell's potential (V). The resulting plot (dQ/dV) contains peaks, numbered 1 through 4, which correspond to specific electrochemical reactions occurring within the electrodes of the cell. The peaks for the cell chemistry analyzed in this study, which utilizes a graphite-silicon anode and an NCA cathode [60], are well documented in literature [71,83–85]. The first peak, centered at 3.52V, is attributed to the onset of graphite lithiation ($C_6 \rightarrow LiC_X$) which continues throughout the charge cycle. The shoulder at 3.41V prior to the first peak may be attributed to the onset of Si lithiation, which occurs at a lower potential than that of graphite. The remaining peaks numbered 2 through 4 correlate to the phase transitions of the cathode active material: $H_1 \rightarrow M$ at 3.71V, $M \rightarrow H_2$ at 3.95V, and $H_2 \rightarrow H_3$ at 4.15V, respectively. The final phase transition correlates to the reduction in hoop strain prior to 100% SoC, as seen in Figure 29a. It can be seen that with consecutive overcharge cycles the dQ/dV peaks, particularly peak 4, shift to a higher potential.

A similar analysis was conducted for the strain measurements, where the differential of the strain ($\mu\epsilon$) was taken with respect to the cell potential (V). The resulting incremental strain analysis (ISA), as seen in Figure 29b, yields peaks in $d\epsilon/dV$ which correspond to the change in strain slope caused by the volumetric changes of the active material within the electrodes. Peak shifting similar to ICA is observed, which implies that cell degradation modes can be deducted

using ISA analysis. This relationship, to the best of the authors' knowledge, has not been reported previously in literature. The peaks are seen to shift to a higher potential but do not reduce in magnitude, which is indicative of loss of conductivity (LOC) and loss of lithium inventory (LLI), signifying that those are the main degradation modes [51,58]. Since none of the peaks reduce in magnitude, little evidence is seen for loss of active material (LAM).

As noted previously, the hoop strain continues to increase cells overcharge from 4.2V to the maximum potential. During 10% OC, the hoop strain reaches approximately 73% higher strain than during normal cycling (at 4.2V with 100mA cutoff). Most of the strain generated in this region seems to be reversible, however, as evidenced by the cell returning to a relatively low strain state – approximately 97 με at the end of the first cycle, as depicted in Figure 28. While it is possible for gas to evolve and some part of it re-absorbed into the electrolyte [91], the most likely cause of the reversible strain after 4.2V is the expanded utilization of the active material within the electrodes. The operational voltage limits of electrochemical cells are usually selected to avoid both particle cracking due to mechanical expansion [84] and electrochemical degradation due to side reactions [92] and. Based on the strain data, limiting the cell to 4.2V does indeed lower the magnitude of forces acting on the active material particles. As the cell approaches 4.2V, the final phase transition of the cathode, labeled as peak 4 in Figure 29, occurs between 4.08 and 4.2V. This causes a large decrease in the c-axis of the NCA active material unit cell, leading to a 4% volume reduction [84], which translates to the strain decrease seen between 3.8 and 4.3 hours (during which the cell is between 4.08 and 4.16V) in Figure 28a. It can be seen that after 4.3 hours (or 4.16V), the strain is neither increasing nor decreasing – as evidenced by the zero slope in Figure 29b – signifying that the volumetric reduction of the cathode active material is matched by the expansion of the anode active materials.

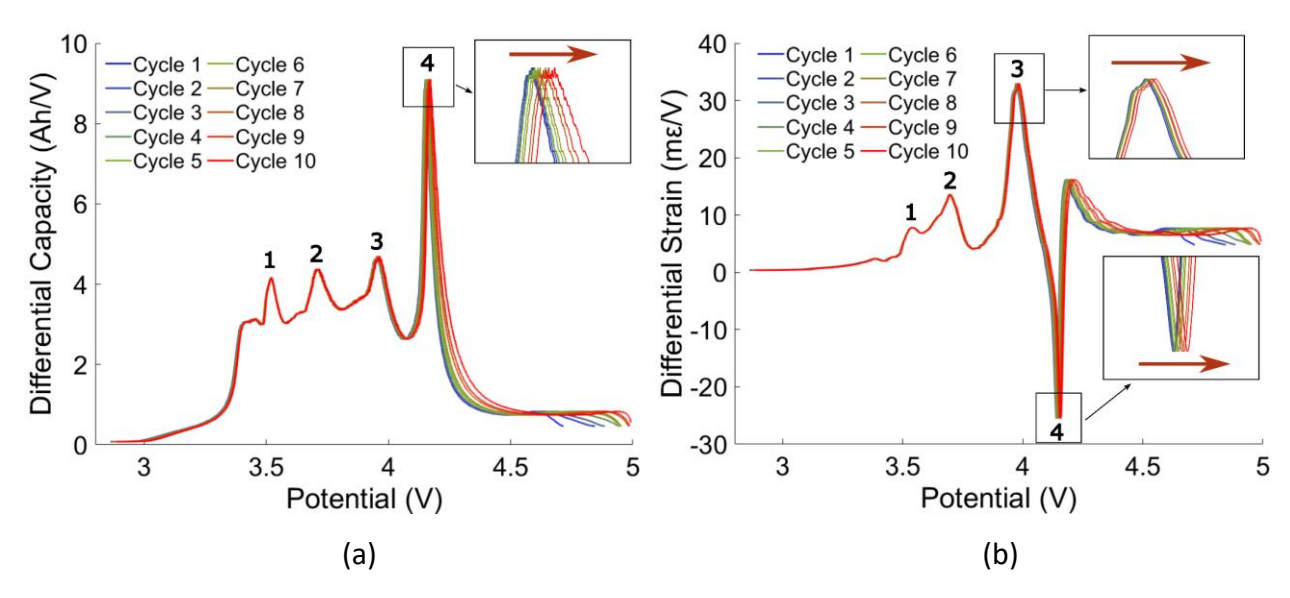


Figure 29: (a) Incremental capacity analysis (ICA) showing dQ/dV peaks and (b) incremental strain analysis (ISA) plots show $d\epsilon/dV$ peaks during the charge step for every 10% OC cycle. Both ICA and ISA show peak shifts towards a higher potential with an increasing cycle number.

As the potential continues to increase, the expansion of the anode dominates the overall cell behavior. Silicon alloys with lithium, and its volumetric expansion is usually approximated to be linear. Graphite lithiates in stages, each of which have a different volume. As the cell's potential climbs past 4.2V, it is likely that graphite continues the transition from stage 2 to stage 1, which leads to significant volume change of the graphite unit cell [93]. The electrochemical reactions slow down considerably after approximately 4.3V, as seen in Figure 29b, but the slope of strain remains positive until the termination of the overcharge step. While gas generation is expected to occur in cathode active material with high nickel content (Ni \geq 80%) [5] as the positive electrode exceeds 4.2V, there is an additional possible source of reversible expansion present. In previous work [60], an SEM-EDS analysis revealed that the silicon particles in the anode range in size from 1 to 5 μ m. Particles of this diameter can take a significant amount of time to lithiate fully, which would contribute to the reversible expansion of the cell after 4.2V.

3.2.6: EIS Analysis and Parameterized Equivalent Circuit

Electrochemical Impedance Spectroscopy (EIS) analysis was performed on cells subjected to 10% OC cycling. Figure 30 shows the EIS response of a fresh cell (before overcharge), after three, and after six overcharge cycles. Each of the collected spectra is modeled as a parameterized equivalent circuit shown in Figure 24, and the predicted result Z_{Re} and Z_{Im} values

for a cell before abuse cycling (pristine), after three 10% OC cycles, and after six 10% OC cycles are shown in Figure 31a, Figure 31b, and Figure 31c, respectively. The parameters for each circuit element are shown in Table 7, where Y and n represent the admittance and phase coefficient for the CPE element and W represents the Warburg coefficient.

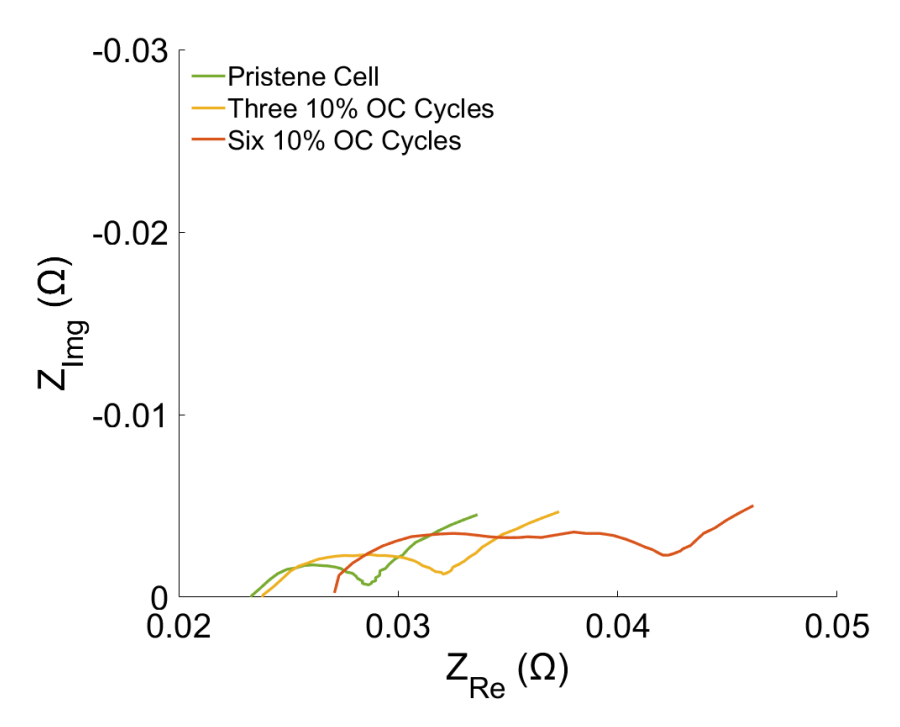


Figure 30: Electrochemical impedance spectra of a cell before OC cycling (pristine), after three, and six 10% OC cycles.

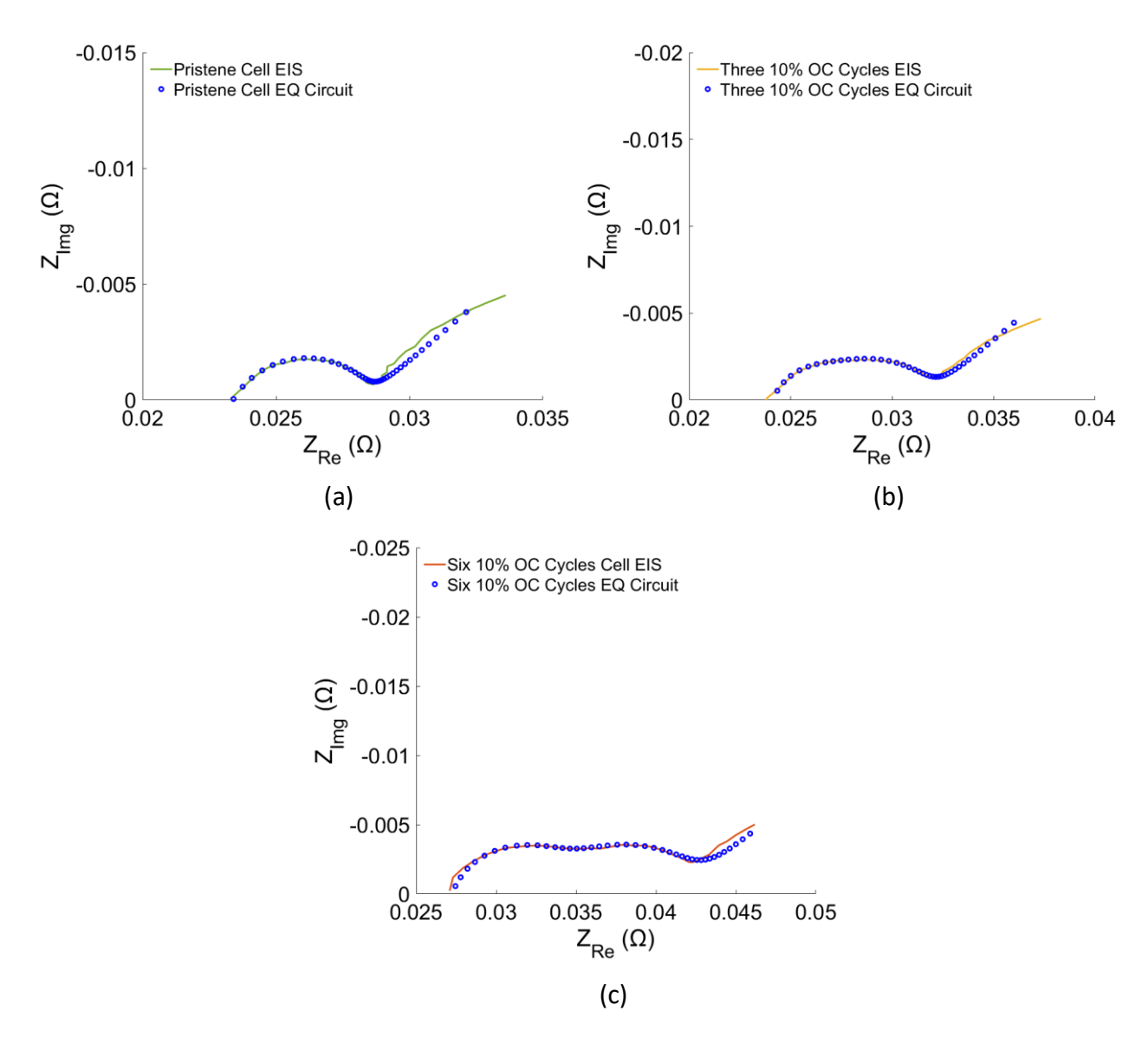


Figure 31: EIS spectrum compared to a parameterized L-R-RC-RC-W circuit for a cell (a) before OC cycling (pristine), (b) after three 10% OC cycles, and (c) after six 10% OC cycles. A good agreement can be seen between the equivalent circuits and the obtained spectra.

The EIS spectrum of the pristine cell is consistent with those reported in literature [58], with one arc present followed by the diffusion behavior. Three overcharge cycles increase the cell's contact resistance slightly, and the central arc is seen to elongate. Six overcharge cycles increase the contact resistance further, implying that the cell experiences conductivity loss (CL), which occurs due to current collector corrosion, binder decomposition, and loss of contact with the active material [50,51,58]. The evolution of the SEI arc between the third and sixth cycles corresponds to the loss of lithium inventory (LLI) degradation mode (DM). This is indicative of electrolyte decomposition and oxidation, as well as changes in SEI thickness and morphology.

The Warburg constant does not change significantly, indicating that loss of active material (LAM) is not a significant degradation mode during this experiment [51].

	L1 (nH)	R2 (mΩ)	R3 (mΩ)	Y3 (F)	n3	R4 (mΩ)	Y4 (F)	n4	W5 $\left(\frac{m\Omega}{\sqrt{s}}\right)$
0 Cyc	350	22.1	4.8	0.80	0.80	1.45	0.16	1.00	3.0
3 Cyc	240	23.4	5.1	2.10	0.80	3.10	0.16	1.00	3.5
6 Cyc	260	26.2	7.3	5.50	0.80	8.30	0.25	0.84	3.3

Table 7: Estimated parameters for the equivalent circuit model.

While some studies report LAM as a major DM during repeated overcharge, the results in this study align with those from Liu et al. [57] who report that during overcharge above 4.5V LLI is the main DM. This is consistent with the behaviors seen in the ICA and ISA plots, as none of the dQ/dV and dɛ/dV peaks reduce in magnitude. This signifies that the crystal structure of the active material, as well as the mechanical integrity of the electrodes, do not degrade significantly during this type of electrical abuse [58]. While EIS and ICA can narrow down the possible DM's present, they cannot provide insight into when a cell's CID will activate. The strain data collected during this work is shown to predict this event accurately. The DM mechanisms present can also be further collaborated using the strain data collected. The decomposition and re-formation of SEI is usually accompanied by gas generation, which is also present during electrolyte oxidation and decomposition. From the combined use of electrochemical and mechanical analyses, the aforementioned degradation mechanisms are shown to be significant during 10% OC abuse.

CHAPTER 4: BATTERY MODELING AND SIMULATIONS

Modern secondary batteries are complex systems with much variability in their design. A full cell, such as one shown in Figure 1, contains many layers of electrodes which are composite materials. The electrochemistry and mechanics of this system are linked and must both be considered to accurately predict its behavior. The goal of this modeling effort is to develop a tool which can predict the mechanical response of a battery due to electrochemical cycling using fundamental data. The electrochemical simulation is accomplished through the COMSOL Multiphysics Batteries and Fuel Cells module, which uses a P2D model modified to be applicable in 3 spatial dimensions (a P4D model) to predict the electrochemical behavior of electrodes. The electrochemical response is calculated using an active material's equilibrium potential as well as electrical and chemical properties. To link the mechanical response of a composite electrode to the electrochemistry, its mechanical properties are needed. A Mori-Tanaka homogenization scheme [94] is used to calculate the effective properties of porous composite electrodes, which are then used in the simulation. This approach allows the mechanical properties of electrodes to be determined purely based on the constituents and their volume fractions, allowing for many types of chemistries and active material loading situations to be modeled.

4.1: Electrochemical Model

One of the most widely used model for simulating the electrochemical behavior of secondary batteries is the pseudo 2-dimensional (P2D) model proposed by Newman and Doyle in 1993 [61], which was extended to a full cell in 1996 [63]. Recently the charge, mass, and energy balance, along with reaction kinetics, were extended from the previous 1D geometry to a 3D space by Lin et al. [67] in 2023. Lithium (de)intercalation and diffusion for active material particles is calculated as a function of the particle's radius, which remains the pseudo dimension.

A schematic of an electrode and the P2D model parameters are shown in Figure 32 below. The spatial dimension is represented by x, which is the thickness of the electrode. The pseudo dimension is the radius of the active material particle and is given by r.

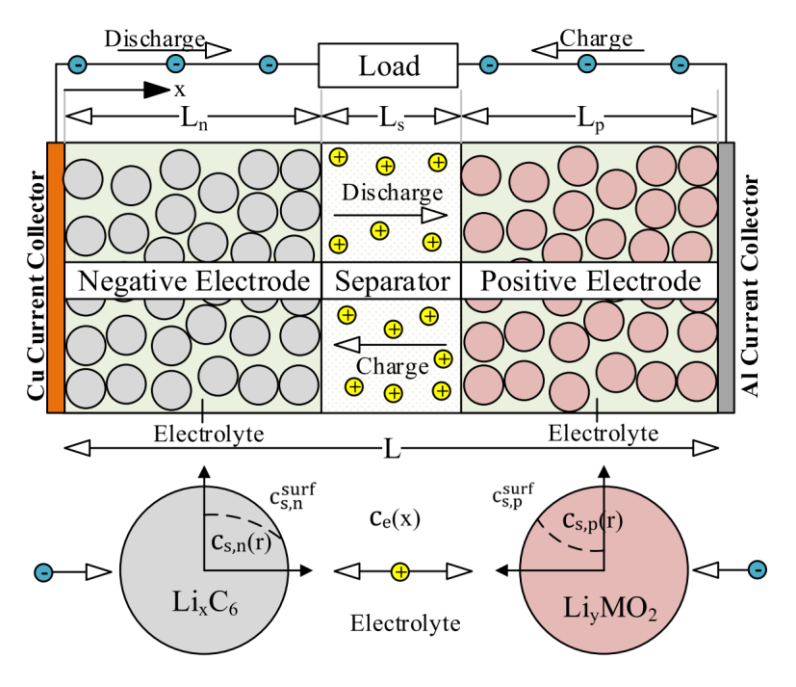


Figure 32: P2D model of an electrode from Jokar et al. [95].

The main equations used for solving the electrochemistry within the P2D model are as follows [95]. The solid-state Li $^{+}$ ion concentration within the solid electrode particles, c $_{s}$, are solved for using Fick's law of diffusion for spherical particle geometry. The concentration of Li $^{+}$ ions within the electrolyte phase – which is also present in the electrolyte-filled pores of the separator – is denoted by c $_{e}$ and solved using mass conservation. The electric potential of the solid phase, denoted by Φ_{s} , is derived using Ohm's law. The electric potential in the liquid electrolyte phase, Φ_{e} , uses both Kirchhoff's and Ohm's laws. Finally, the pore wall flux of Li $^{+}$ ions within the electrodes are related to the applied current by the Butler-Volmer kinetics equations. These relations are given for the electrodes by Equation 3-Equation 8, and for the separator by Equation 9 and Equation 10. As mentioned previously, x is the spatial dimension at the electrode scale, while the variable r is used to calculate the lithium concentration within the active material. This model is time-dependent, which is represented by the variable t.

$$\frac{\partial c_s(x,r,t)}{\partial t} = \frac{D_S}{r_p^2} \frac{\partial}{\partial r} \left(r_p^2 \frac{\partial c_s(x,r,t)}{\partial r} \right)$$

Equation 3

$$\varepsilon_p \frac{\partial c_e(x,t)}{\partial t} = \frac{\partial}{\partial x} \left(D_{eff} \frac{\partial c_e(x,t)}{\partial x} \right) \alpha_e (1 - t_+) J(x,t)$$

Equation 4

$$\sigma_{eff} \frac{\partial^2 \Phi_s(x,t)}{\partial x^2} = a_e FJ(x,t)$$

Equation 5

$$-\sigma_{eff}\frac{\partial\Phi_{s}(x,t)}{\partial x}-k_{eff}\frac{\partial\Phi_{e}(x,t)}{\partial x}+\frac{2k_{eff}RT}{F}(1-t_{+})\frac{\partial\ln c_{e}}{\partial x}=I_{a}$$
 Equation 6

$$J(x,t) = K_c \left(c_s^{max} - c_s^{surf}\right)^{0.5} \left(c_s^{surf}\right)^{0.5} c_e^{0.5} \left[\exp\left(\frac{0.5F\mu_s(x,t)}{RT}\right) - \exp\left(-\frac{0.5F\mu_s(x,t)}{RT}\right) \right]$$
Equation 7

$$\mu_{s}(x,t) = \Phi_{s}(x,t) - \Phi_{e}(x,t) - U_{k}; \qquad V_{cell}(t) = \Phi_{s}(0,t) - \Phi_{s}(L,t)$$
 Equation 8

$$\varepsilon_p \frac{\partial c_e(x,t)}{\partial t} = \frac{\partial}{\partial x} \left(D_{eff} \frac{\partial c_e(x,t)}{\partial x} \right)$$

Equation 9

$$-k_{eff}\frac{\partial\Phi_{e}(x,t)}{\partial x}+\frac{2k_{eff}RT}{F}(1-t_{+})\frac{\partial\ln c_{e}}{\partial x}=I_{a}$$

Equation 10

The P2D model is widely used and is known to provide accurate results. One of its limitations, however, is that it can only resolve a 1D geometry. As mentioned previously, Lin et al. [67] extended the P2D model to a 3D geometry, creating the P4D model. The most notable change in this formulation comes from the partial derivatives in the x direction being replaced by the gradient operator (∇). This model is used within the COMSOL Multiphysics Batteries and Fuel Cells module to simulate the electrochemistry of half and full cells. The Batteries and Fuel Cells

module contains a materials library for most commonly used active materials (e.g., graphite anode, NMC111 cathode, NCA cathode, and silicon as an additional active material) and electrolyte-solvent blends (e.g., 1M LiPF6 in 2:1 EC:DMC), with electrical and chemical properties accounted for. Each active material also contains an equilibrium potential as a function of lithium content, providing the tools needed for electrochemical simulations.

Currently, the mechanical properties and volumetric changes of an electrode during cycling need to be determined experimentally, which are both functions of the active material type and content, as well as the other constituents. The modeling process used in this work is able to accept fundamental elastic properties of the composite electrode components – active material, binder, conductive additives, and porosity – to predict the mechanical properties of the electrodes. With the wealth of published data about the volumetric changes within various types of active materials, measured using X-ray diffraction (XRD), the volumetric changes at the electrode scale can be quantified. By combining these, the mechanical behavior of electrodes with various chemistries and different percentages of constituents can be predicted. This prediction is controlled by the active material lithium content (i.e., SoC), and can therefore be easily coupled with FEA software capable of running electrochemical simulations, such as COMSOL Multiphysics. Here, stress is calculated at the electrode level and compared to published anode and cathode data. A portion of an 18650 cell is then simulated to predict its mechanical response. This prediction can be useful for battery pack design and predicting how much expansion cells with different chemistries are expected to expand and contract by. The cell-level behavior is also useful for practically applying the findings from the strain measurements in this study. If the amount of expansion from a cell is known, strain gages or pressure sensors can be placed at strategic locations within a battery pack to detect cell degradation and precursors to thermal runaway using mechanical measurements.

4.2: Mori-Tanaka (M-T) Homogenization Scheme with Eshelby Formulation

The homogenization scheme used in this work was first introduced by Mori and Tanaka in 1973 [94] and is useful for determining the effective elastic properties of a composite material. It leverages John Eshelby's [96] formulation for the elastic field of an elliptical inclusion in an infinite homogeneous matrix material. Figure 33 illustrates a composite geometry with a matrix

(Phase 1) and ellipsoidal inclusions (Phases 2-4) and equates it to a homogenized material where the effective elastic properties are the combination of those of the constituents. A representative volume element (RVE) is chosen to be large enough to characterize the behavior of the inclusion and matrix, yet small compared to the entire composite. This RVE, along with an ellipsoidal inclusion is illustrated in Figure 33 below. The matrix and inclusion are treated as linear elastic materials where stress is defined by Equation 11 and Equation 12 below, where C_{ijkl} is the stiffness tensor of the matrix material. The stiffness tensor with the superscript Ω represents the inclusion material.

$$\sigma_{ij} = C_{ijkl} \varepsilon_{kl}$$

Equation 11

$$\sigma_{ij} = C_{ijkl}^{\Omega} \varepsilon_{kl}$$

Equation 12

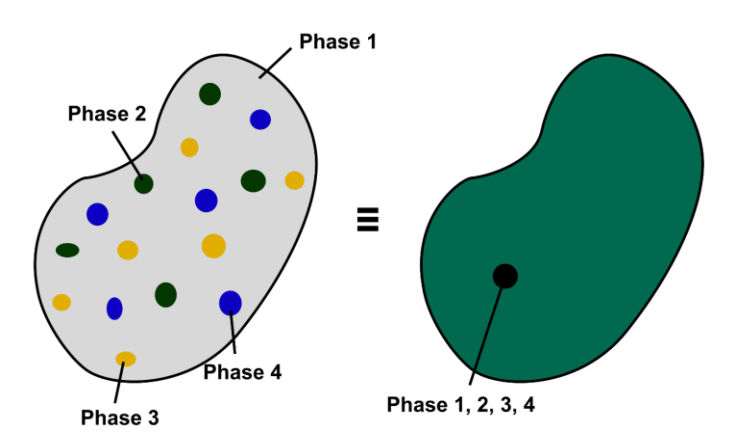


Figure 33: Composite material homogenized into one with effective properties.

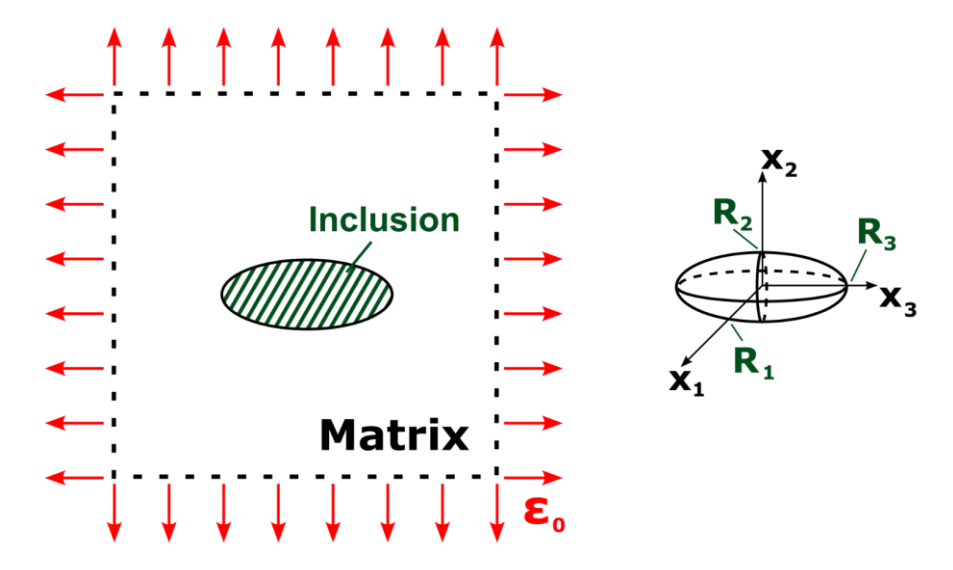


Figure 34: RVE representing an infinite medium with an ellipsoidal inclusion.

The total volume encapsulated in the RVE is represented by V, while that of the inclusion is represented by Ω , as shown in Figure 35. All terms in this formulation denoted by Ω relate to the inclusions, while those without relate to the matrix material. The initial approach is similar to the solution of a biaxially loaded infinite medium with a stress-free hole [97], where the solution first considers a stress state at the far field, where the contribution of the hole is not present. In a similar fashion, a uniform solution is considered for the matrix without an inclusion, which is denoted by "o" in the equations below. The "defect" solution, denoted by "d," considers the contribution of the inclusion on the stress state of the composite in the RVE.

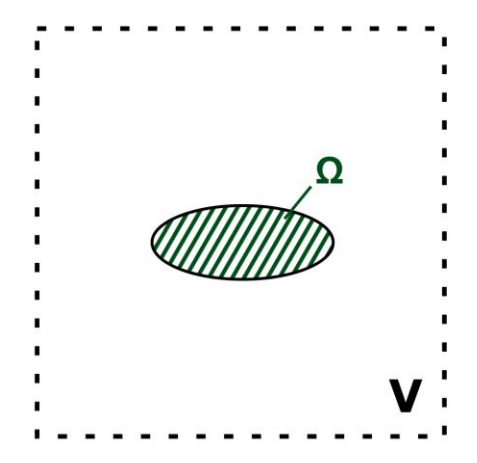


Figure 35: Homogenization RVE showing the inclusion region (Ω) and the matrix (V- Ω).

$$\sigma_{ij} = \sigma_{ij}^o + \sigma_{ij}^d$$

Equation 13

$$\varepsilon_{kl} = \varepsilon_{kl}^o + \varepsilon_{kl}^d$$

Equation 14

Then, the stress in the matrix only $(V-\Omega)$ region is:

$$\sigma_{ij}^{o} + \sigma_{ij}^{d} = C_{ijkl} (\varepsilon_{kl}^{o} + \varepsilon_{kl}^{d})$$
 in $(V - \Omega)$

Equation 15

Additionally, the stress in the inclusion only (Ω) is represented by:

$$\sigma_{ij}^{o} + \sigma_{ij}^{d} = C_{ijkl}^{\Omega} (\varepsilon_{kl}^{o} + \varepsilon_{kl}^{d})$$
 in Ω

Equation 16

As mentioned previously, the local effects of the inclusion decay when considering the far-field, and the stress only has the uniform component:

$$\sigma_{ij}^o = C_{ijkl} \varepsilon_{kl}^o$$

Equation 17

Next step in the formulation is to introduce the concept of eigenstrain. Deformation caused by thermal expansion and phase change can be represented by eigenstrain. At the boundary, the traction vectors are equal in magnitude. The load on the matrix exerted by the inclusion is equal in magnitude to the load on the inclusion from the matrix, with the normal vectors having opposite directions. By including the eigenstrain in the formulation, the stress field within the inclusion can be described using the stiffness tensor of the matrix material:

$$C_{ijkl}^{\Omega}(\varepsilon_{kl}^{o} + \varepsilon_{kl}^{d}) \equiv C_{ijkl}(\varepsilon_{kl}^{o} + \varepsilon_{kl}^{d} - \varepsilon_{kl}^{r})$$

Equation 18

The eigenstrain term, denoted by the "r" superscript, is added to the inclusion region in

order to use the same stiffness tensor:

$$\sigma_{ij}^o + \sigma_{ij}^d = C_{ijkl} \left(\varepsilon_{kl}^o + \varepsilon_{kl}^d - \varepsilon_{kl}^r \right) \quad in \ \Omega$$
 Equation 19

When considering the effects and stress field of the inclusion (i.e., Equation 19), the contribution of the inclusion on stress is:

$$\sigma_{ij}^d = \mathcal{C}_{ijkl} \varepsilon_{kl}^d \qquad in \ (V - \Omega)$$
 Equation 20

$$\sigma_{ij}^d = C_{ijkl} (\varepsilon_{kl}^d - \varepsilon_{kl}^r)$$
 in Ω

Equation 21

Equation 20 and Equation 21 can now be used with equilibrium equations and boundary conditions. If an RVE in equilibrium is considered, such as in Figure 35, the body force will be zero $(\sigma_{ij,j}=0 \text{ in V})$. It is also known that at a far enough distance from the inclusion, the stress field decays $(\sigma_{ij}^d=0 \text{ at }\infty)$. Therefore, the following three equations are derived:

$$\left(C_{ijkl}\varepsilon_{kl}^{d}\right)_{,j}=0 \quad in\left(V-\Omega\right)$$

Equation 22

$$\left(C_{ijkl}\left(\varepsilon_{kl}^d - \varepsilon_{kl}^r\right)\right)_{,j} = 0 \quad \rightarrow \quad \left(C_{ijkl}\varepsilon_{kl}^d\right)_{,j} = \left(C_{ijkl}\varepsilon_{kl}^r\right)_{,j} \quad in \ \Omega$$

Equation 23

$$C_{ijkl}\varepsilon_{kl}^d=0$$
 at ∞

Equation 24

From the balance of forces, it is known that the summation of the hydrostatic component of the stress and body forces in Equation 22 equals zero. Therefore, the right side of Equation 23 represents the body force (F). Then, Equation 23 can be expressed as:

$$(C_{ijkl}\varepsilon_{kl}^r)_{,j} = -F_i \quad in \Omega$$

Equation 25

The above set of equations (Equation 22, Equation 24, and Equation 25) can now be solved using Green's function [97], as formulated below:

$$\varepsilon_{kl}^d = \frac{1}{2} \int_{\Omega}^{\square} F_i \left[G_{kj,l}(x - y) + G_{lj,k}(x - y) \right] dy$$

Equation 26

The solution to Green's function will yield the Eshelby tensor (T_{ijkl}^{Ω}) :

$$\varepsilon_{kl}^d = T_{klmn}^{\Omega} \varepsilon_{mn}^r$$

Equation 27

The Eshelby tensor is then expressed using elliptical integrals (I and J):

$$[8\pi(1-\nu)]T_{ijkl}^{\Omega} = \delta_{ij}\delta_{kl}(2\nu I_l + J_{lK}) + \left(\delta_{ik}\delta_{jl} + \delta_{jk}\delta_{il}\right)\left[(1-\nu)(I_K + I_L) + J_{IJ}\right]$$
 Equation 28

The elliptical integrals are defined using Equation 29-Equation 31 below using the axes and radii defined in Figure 34:

$$I_{I} = 2\pi R_{1}R_{2}R_{3} \int_{0}^{\infty} \frac{ds}{(R_{I}^{2} + s)\sqrt{(R_{1}^{2} + s)(R_{2}^{2} + s)(R_{3}^{2} + s)}}$$

Equation 29

$$I_{IJ} = 2\pi R_1 R_2 R_3 \int_0^\infty \frac{ds}{(R_I^2 + s) \left(R_J^2 + s\right) \sqrt{(R_1^2 + s)(R_2^2 + s)(R_3^2 + s)}}$$

Equation 30

$$J_{IJ} = R_J^2 I_{IJ} - I_I$$

Equation 31

To express the strain field in terms of applied deformation (i.e., ε0 in Figure 34), Hooke's

law, Equation 18, and Equation 27 are used. This yields Equation 32, where II_{pqkl} is a fourth order identity tensor defined by Equation 33 below:

$$\begin{split} \big[T_{pqmn}^{\Omega} C_{mnij}^{-1} \big(C_{ijkl}^{\Omega} - C_{ijkl} \big) + II_{pqkl} \big] \big(\varepsilon_{kl}^o + \varepsilon_{kl}^d \big) &= \varepsilon_{pq}^o \end{split}$$
 Equation 32

$$II_{pqkl} = \frac{1}{2} \left(\delta_{pk} \delta_{ql} + \delta_{pl} \delta_{qk} \right)$$
 Equation 33

The term on the left side of Equation 32 in square brackets can be expressed as tensor B, as shown in Equation 34 below. This form can then be used to determine the localization tensor P, which is the inverse of the B tensor:

$$B_{pqkl} \left(arepsilon_{kl}^o + arepsilon_{kl}^d
ight) = arepsilon_{pq}^o$$
 Equation 34

$$\varepsilon_{kl}^o + \varepsilon_{kl}^d = P_{klpq}^{\Omega} \varepsilon_{pq}^o$$

Equation 35

With the strain field expressed in terms of applied strain (ϵ_0), it is now useful to consider the composite at the macro scale, as shown in Figure 33. When the constituents in a matrix have a perfectly random distribution and orientation, the sense of anisotropy is lost. Therefore, at the macro scale, the composite is considered to be a isotropic and linear elastic. To reflect this in the localization tensor P, the process of isotropization is conducted, where the tensor is divided into hydrostatic (P_H) and shear (P_S) components, as denoted by the superscripts "H" and "S" and below.

$$P_{ijkl}^{\Omega} = P_H^{\Omega} \Lambda_{ijkl}^{\rm H} + P_S^{\Omega} \Lambda_{ijkl}^{\rm S}$$
 Equation 36

The components of the above localization tensor are given in Equation 37-Equation 40 below.

$$\Lambda_{ijkl}^{\rm H} = \frac{\delta_{ij}\delta_{kl}}{3}$$

Equation 37

$$\Lambda_{ijkl}^{\rm S} = II_{ijkl} - \Lambda_{ijkl}^{\rm H} = \frac{1}{2} \left(\delta_{ik} \delta_{lj} + \delta_{il} \delta_{jk} \right) - \frac{\delta_{ij} \delta_{kl}}{3}$$

Equation 38

$$P_H^{\Omega} = \frac{P_{iikk}}{3}$$

Equation 39

$$P_S^{\Omega} = \frac{P_{ijij}^{\Omega} - P_H^{\Omega}}{5}$$

Equation 40

A useful addition to this formulation is the case of spherical inclusions within the composite. As shown in the SEM analysis in Figure 8, many of the graphite particles have a spherical shape. The silicon and cathode particles are oblong, but the ratios of the radii are not consistent. Therefore, it is still worthwhile to apply the simplified spherical shape as an initial approximation. Furthermore, while it is clear that the void space between the active material particles is not spherical, it will be treated as spherical inclusions with a Young's Modulus and Poisson's Ratio of zero. The effects of the particle shapes will be taken into consideration when evaluating the accuracy of predictions made by this model.

When the inclusions are estimated to be spherical, their radii will be equal $(R_1=R_2=R_3)$. When this condition is applied to the shape integrals specified in Equation 29-Equation 31, they will have the following solutions:

$$I_1 = I_2 = I_3$$

Equation 41

$$I_{IJ} = \frac{4\pi}{R^2}$$
 $I, J = 1, 2, 3$

Equation 42

$$J_{IJ} = -\frac{8\pi}{15}$$

Equation 43

The Eshelby tensor is then evaluated, as shown in Equation 44, to achieve the result shown in Equation 45.

$$[8\pi(1-\nu)]T_{ijkl}^{\Omega} = \delta_{ij}\delta_{kl}(2\nu I_I + J_{IK}) + \left(\delta_{ik}\delta_{jl} + \delta_{jk}\delta_{il}\right)\left[(1-nu)\left(I_K + I_L + J_{IJ}\right)\right]$$
Equation 44

$$T_{ijkl}^{\Omega} = \frac{5\nu - 1}{12(1 - \nu)} \delta_{ij} \delta_{kl} + \frac{4 - 5\nu}{15(1 - \nu)} \left(\delta_{ik} \delta_{jl} + \delta_{jk} \delta_{il} \right)$$

Equation 45

Now Equation 33, Equation 37, and Equation 38 are applied to express the Eshelby tensor using hydrostatic and shear components:

$$T_{ijkl}^{\Omega} = \frac{1+\nu}{3(1-\nu)} \Lambda_{ijkl}^{H} + \frac{8-10\nu}{15(1-\nu)} \Lambda_{ijkl}^{S}$$

Equation 46

Since the Eshelby tensor can be written as a sum of Λ^{H} and Λ^{S} , it is isotropic. Next, the stiffness tensor of the inclusion is expressed as a combination of the hydrostatic and shear components:

$$C_{ijkl}^{\Omega} = k^{\Omega} \delta_{ij} \delta_{kl} + \mu^{\Omega} \left(\delta_{ik} \delta_{jl} + \delta_{jk} \delta_{il} - \frac{2}{3} \delta_{ij} \delta_{kl} \right) = 3k^{\Omega} \Lambda_{ijkl}^{H} + 2\mu^{\Omega} \Lambda_{ijkl}^{S}$$

Equation 47

Similarly, the stiffness tensor of the matrix material can be expressed in similar terms:

$$C_{ijkl} = 3k\Lambda_{ijkl}^{\rm H} + 2\mu\Lambda_{ijkl}^{\rm S}$$

Equation 48

The definitions of the stiffness tensor can now be used to evaluate the localization tensor, which is the inverse of the B tensor. After substitutions and mathematical development, the solutions for tensors B and P are obtained, as shown by Equation 49 and Equation 50 below.

$$B_{pqkl} = \left[\left(1 + \frac{1 + \nu}{3(1 - \nu)} \frac{k^{\Omega} - k}{k} \right) \Lambda_{pqkl}^{H} + \left(1 + \frac{8 - 10\nu}{15(1 - \nu)} \frac{\mu^{\Omega} - \mu}{\mu} \right) \Lambda_{pqkl}^{S} \right]$$

Equation 49

$$P_{pqkl} = B_{pqkl}^{-1} = \left[\frac{1}{1 + \frac{1 + \nu}{3(1 - \nu)} \frac{k^{\Omega} - k}{k}} \right] \Lambda_{pqkl}^{\mathrm{H}} + \left[\frac{1}{1 + \frac{8 - 10\nu}{15(1 - \nu)} \frac{\mu^{\Omega} - \mu}{\mu}} \right] \Lambda_{pqkl}^{\mathrm{S}}$$

Equation 50

When compared to Equation 36, it is clear that the term in the first square bracket of Equation 50 is PH, while the second is PS. These terms can be simplified and re-written as shown in Equation 51 and Equation 52, respectively. The terms in Equation 51 and Equation 52 which don't have a superscript Ω relate to the matrix material. As mentioned previously, this solution is only applicable in the case where the inclusions are spherical in shape.

$$P_H^{\Omega} = \frac{k + \frac{4\mu}{3}}{k^{\Omega} + \frac{4\mu}{3}}$$

Equation 51

$$P_S^{\Omega} = \frac{\mu + \xi}{\mu^{\Omega} + \xi} \qquad \text{where } \xi = \frac{\mu(9k + 8\mu)}{6(k + 2\mu)}$$

Equation 52

The next step in the homogenization scheme is to define the approximated strain tensor. The formulation in Equation 53 below uses the subscript α to represent the constituents of the composite, where α =1 represents the matrix material, while α =2, ..., M represents the other constituents present, all of which may have different mechanical properties.

$$\langle \varepsilon_{ij}^{\alpha} \rangle = P_{ijkl}^{\alpha} \varepsilon_{kl}^{o} = \left(\varepsilon_{ij}^{o} + \varepsilon_{ij}^{d} \right)^{\alpha} \quad (\alpha = 1, 2, ..., M)$$
Equation 53

To account for the contribution of each constituent, Mori and Tanaka applied an approximation rule with is similar to the Rule of Mixtures. The total strain response of the composite is then represented by Equation 54 below, where the volume fraction of each constituent is represented by Φ^{α} .

$$\langle \varepsilon_{ij} \rangle = \sum_{\alpha=1}^{M} \phi^{\alpha} \langle \varepsilon_{ij}^{\alpha} \rangle = \sum_{\alpha=1}^{M} \phi^{\alpha} P_{ijkl}^{\alpha} \varepsilon_{kl}^{o}$$

Equation 54

The approximated strain tensor can be transformed into stress by applying Hooke's Law and including the stiffness tensor in the formulation.

$$\langle \sigma_{ij} \rangle = \sum_{\alpha=1}^{M} \phi^{\alpha} C_{ijkl}^{\alpha} P_{klmn}^{\alpha} \varepsilon_{mn}^{o}$$

Equation 55

The right side of Equation 55 can also be expressed as a function of the approximated strain tensor, where \overline{C}_{ijkl} represents the effective stiffness tensor of the entire composite, as shown in Equation 56 below.

$$\langle \sigma_{ij} \rangle = \bar{C}_{ijkl} \langle \varepsilon_{ij} \rangle$$

Equation 56

The right sides of Equation 55 and Equation 56 can be set equal to each other for further formulation. Since the effective stiffness tensor is isotropic, it can be moved inside of the

summation sign of the term on the right of Equation 54. Additionally, since the strain field applied to the RVE is constant and always non-zero, it can be moved out the equation.

$$\sum_{\alpha=1}^{M} \left[\phi^{\alpha} \left(\bar{C}_{ijkl} - C_{ijkl}^{\alpha} \right) P_{ijkl}^{\alpha} \right] = 0$$

Equation 57

The stiffness tensor C can be decomposed into hydrostatic and shear components as shown below, where the bulk modulus is represented by k and shear modulus by μ .

$$C^{\alpha}_{ijkl} = 3k^{\alpha}\Lambda^{H}_{ijkl} + 2\mu^{\alpha}\Lambda^{S}_{ijkl}$$

Equation 58

$$\bar{C}_{ijkl} = 3\bar{k}\Lambda^{\rm H}_{ijkl} + 2\bar{\mu}\Lambda^{S}_{ijkl}$$

Equation 59

The definitions in Equation 58 and Equation 59 can then be used in Equation 57, which yields the following relations:

$$\sum_{\alpha=1}^{M} \left[\phi^{\alpha} \left(3\bar{k} - 3k^{\alpha} \right) P_{H}^{\alpha} \right] = 0$$

Equation 60

$$\sum_{\alpha=1}^{M} \left[\phi^{\alpha} (2\bar{\mu} - 2\mu^{\alpha}) P_{S}^{\alpha}\right] = 0$$

Equation 61

Finally, the effective properties of the composite can be calculated in terms of bulk and shear moduli.

$$\bar{k} = \frac{\sum_{\alpha=1}^{M} \phi^{\alpha} k^{\alpha} P_{H}^{\alpha}}{\sum_{\alpha=1}^{M} \phi^{\alpha} P_{H}^{\alpha}}$$

Equation 62

$$\bar{\mu} = \frac{\sum_{\alpha=1}^{M} \phi^{\alpha} \mu^{\alpha} P_{S}^{\alpha}}{\sum_{\alpha=1}^{M} \phi^{\alpha} P_{S}^{\alpha}}$$

Equation 63

The bulk and shear moduli can then be converted into Young's Modulus and Poisson's Ratio using elastic constants relations [97]:

$$\bar{E} = \frac{9\bar{k}\bar{\mu}}{3\bar{k} + \bar{\mu}}$$

Equation 64

$$\bar{\nu} = \frac{3\bar{k} - 2\bar{\mu}}{6\bar{k} + 2\bar{\mu}}$$

Equation 65

As mentioned previously, the case of spherical inclusion is a good starting point for the analysis of composite electrodes. When calculating the effective properties of a matrix with spherical inclusion, Equation 51 and Equation 52 can be used to obtain the following solutions, where the bulk and shear moduli without a superscript are those of the matrix material.

$$\bar{k} = \frac{\sum_{\alpha=1}^{M} \phi^{\alpha} k^{\alpha} \frac{k + \frac{4\mu}{3}}{k^{\alpha} + \frac{4\mu}{3}}}{\sum_{\alpha=1}^{M} \phi^{\alpha} \frac{k + \frac{4\mu}{3}}{k^{\alpha} + \frac{4\mu}{3}}}$$

Equation 66

$$\bar{\mu} = \frac{\sum_{\alpha=1}^{M} \phi^{\alpha} \mu^{\alpha} \frac{\mu + \xi}{\mu^{\alpha} + \xi}}{\sum_{\alpha=1}^{M} \phi^{\alpha} \frac{\mu + \xi}{\mu^{\alpha} + \xi}} \qquad where \ \xi = \frac{\mu(9k + 8\mu)}{6(k + 2\mu)}$$

Equation 67

4.3: Application of M-T Homogenization to Composite Electrodes

4.3.1: Model Assumptions

Throughout the M-T homogenization scheme explanation, many similarities can be seen between the composite considered during the formulation and the composite electrodes used in Li-ion batteries. This section will analyze the assumptions made and their relevance to a composite electrode. First, it is important to list all of the constituents inside each electrode.

In the case of the anode, the composition includes active material (usually graphite), a polymeric binder, and a conductive additive (CA). The cathode has a similar composition, where the active material is usually a transition metal oxide (such as NCA or NMC) with a layered structure, with polymer and a CA present as well. Both electrodes are porous, with empty space usually accounting for up to 40% of an electrode's volume. The polymeric binder used in electrode fabrication serves multiple functions; it provides both structural support to the electrodes and also conducts electrons which enable the electrochemical reactions within the active material. The CA is added to the polymer to improve its electrical conductivity during the manufacturing process, ensuring that the particles are homogeneously distributed. The CA-infused binder coats the outside of the active material particles, forming bridges between them. The void space, which is between the binder-coated particles, is filled with electrolyte after the electrodes are assembled into an electrochemical cell.

One of the first assumptions made during the M-T homogenization scheme was that all of the constituents, including the matrix, are linear elastic and therefore follow Hooke's Law. While considering the validity of this assumption, it is important to understand the magnitude of stress that electrodes experience. The experimentally measured experienced by electrodes during cycling was reported by Sethuraman et al. [30] for a composite graphite anode and by Nadimpalli et al. [31] for both a composite graphite anode and an NMC cathode. Considering both studies, the anode reached a maximum compressive stress of 10-12 MPa and a tensile stress

of 1-4 MPa. The active materials within the anode (i.e., graphite and silicon) exhibit a linear elastic behavior in this range. Graphite follows the same stress-strain curve until it reaches approximately half of its yield strength [98], which is approximately 79 MPa. Silicon, which has an amorphous structure after the first lithiation, has a reported yield strength of 1.48 GPa [99]. Though this value is for a thin film, it is still significantly higher than the experimental stress reported. The CA particles are in the form of carbon black or acetylene black in the anode and small graphite particles in the cathode and are therefore expected to behave in a similar way as the graphite active material particles. The cathode active material is in the form of small spherical particles as well (called secondary particles) which are agglomerates of layered oxide particles (called primary particles). Oxides usually have high yield strength and therefore the assumption of linear elastic behavior is expected to be accurate. The polymeric binder used in the anode is usually carboxymethyl cellulose (CMC), polyacrylic acid (PAA), styrene-butadiene rubber (SBR), or a combination of the three. The cathode usually uses polyvinylidene difluoride (PVdF), due to its use of an non-aqueous, as water-based solvents will degrade the cathode's active material. Though polymers are known to have viscoelastic behavior, the viscous contribution is highly time dependent. The intended simulation time for the electrochemical cells is on the order of hours, with a 10 hour charge/discharge time used for most simulations. At this time scale the viscous behavior of the polymers is expected to be negligible. Finally, the pores/voids are empty space with a zero Young's Modulus and Poisson's Ratio.

Another assumption is that the constituents of the composite, including the matrix, are isotropic. The type of graphite used for active material and additives is usually natural graphite, as specified by manufacturers. This form of graphite is polycrystalline [100], with the crystals oriented in random directions. Therefore, at the particle level, graphite can be considered as isotropic. The same justification applies to the cathode secondary particles, which are comprised of randomly oriented primary particles or aligned elongated particles, specifically to minimize anisotropic effects [101]. An SEM analysis revealed that the cathode used in the studied cells consists of secondary particles composed of randomly distributed primary particles, as shown in Figure 36. Since silicon is in an amorphous form, it too will have isotropic behavior. Polymers will have a randomly oriented cross-lined network and will also behave isotropically. Additionally, the

slurry of active material, polymer, and CA is thoroughly mixed to prevent agglomeration, which is comparable to the perfectly randomly distributed and oriented assumption made earlier in the chapter.

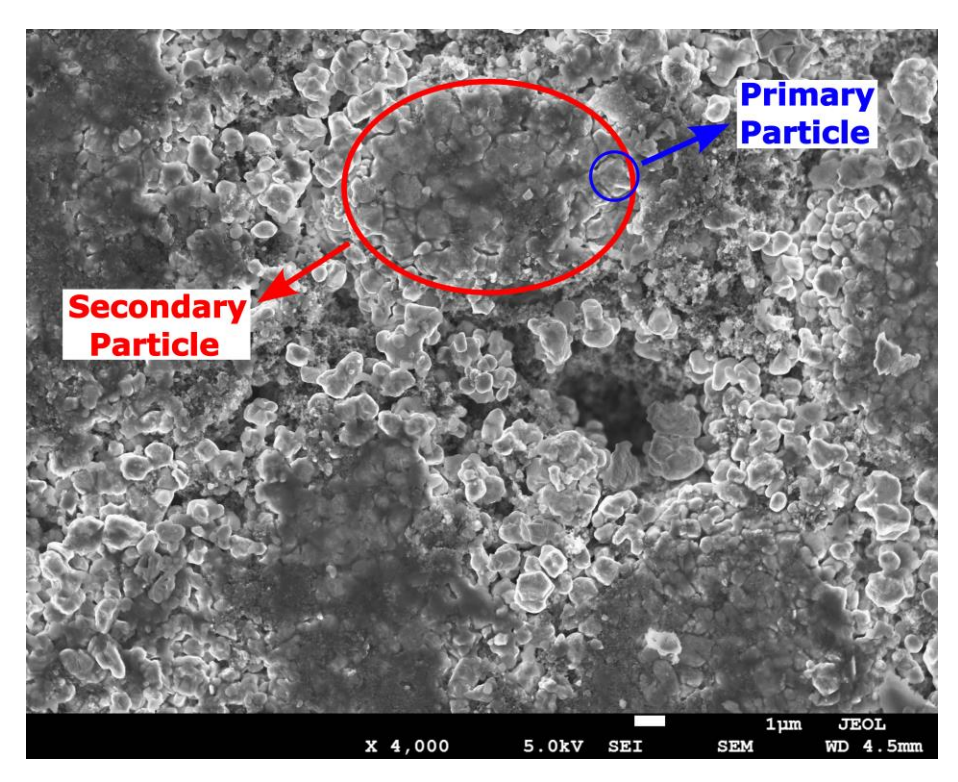


Figure 36: Secondary NMC active material particles with (top) randomly distributed primary particles and (bottom) aligned elongated particles by Park et al. [102].

For this initial estimation, the mechanical properties of the constituents are taken to be constant. The Young's Modulus of graphite and silicon is known to change as a function of lithium content [103,104], and will be taken into account during the refinement of this analysis at a later time. For the polymeric binder, only the mechanical properties during dry conditions could be readily found in literature and were therefore used. The shape of all the constituents was estimated to be spherical for the analysis conducted, though this can also be changed in the future to further refine the model.

The source of expansion and contraction of the electrodes is the volumetric changes of the active material as it reacts with lithium. Therefore, the active material will change volume during cycling, both in the anode and cathode. The binder and CA are considered to be incompressible – that is, their volume remains constant during electrochemical cycling. Through

literature surveys, it was determined that the porosity of the electrodes changes [105]. Qi and Harris [106] found through X-ray tomography that the porosity of graphite anodes in their study reduced by 15-25%. It is reasonable to assume that this percentage could be even higher for electrodes containing silicon due to the additional volumetric expansion. The electrolyte which usually fills the pores has been recently found to move out of the jellyroll due to the volumetric changed of the electrodes [107]. This signifies that the pores in the electrode are connected, and electrolyte will not significantly resist the expansion of the electrodes. The changes in the volume fractions of the constituents due to (de)lithiation are not considered during the homogenization. That is, the mechanical properties are homogenized using the initial volume fractions and are assumed to remain constant throughout cycling. This assumption is of course a simplification and will be improved in future work.

4.3.2: Results of M-T Homogenization

A total of four types of anodes and two types of cathodes were homogenized using the M-T approach described in this chapter. The anodes include the one studied by Sethuraman et al. [30], Nadimpalli et al. [31], graphite anode with 5% Si content used in the 18650 cells used for strain measurements in this research, and a graphite anode with 20% Si (by weight) purchased from NEI for stress measurement electrodes. The cathodes include an NMC111 chemistry one and the NCA cathode used in the 18650 cells studied. The NMC111 cathode was the closest stoichiometry-wise to the one studied by Nadimpalli et al. [31]. The anodes will be referred to as NEG1, NEG2, NEG3, and NEG4 in the order they are listed. The cathodes will be referred to as POS1 and POS2, respectively. The mechanical properties used for each constituent [30,103,108–111] are summarized in Table 8 below, along with their origin. The properties for conductive additives were taken to be the same as those of graphite. The volume fractions of each constituent for the homogenized electrodes are listed in Table 9. The symbol ϕ_{AM1} is used to represent the primary active material in the electrodes, and ϕ_{AM2} represents the additional active material (Si) which is present in some of the anodes.

Material	Young's Modulus	Poisson's Ratio
Graphite	10 GPa	0.38
Silicon	80 GPa	0.26
NCA	193 GPa	0.28
NMC111	199 GPa	0.25
PVdF	2 GPa	0.38
PAA	3 GPa	0.34
SBR	2 GPa	0.48

Table 8: Elastic properties of active materials.

Electrode	Label	Фам1	Фамг	Фв	Фса	ФР
Graphite anode from Ref. [30]	NEG1	0.623	-	0.068	-	0.309
Graphite anode from Ref. [31]	NEG2	0.648	-	0.055	0.037	0.260
Graphite anode with 5% Si from 18650 cells	NEG3	0.479	0.025	0.080	0.026	0.390
Graphite anode with 20% Si from NEI Corp	NEG4	0.363	0.110	0.084	0.043	0.400
NMC111 cathode similar to Ref. [31]	POS1	0.443	-	0.111	0.075	0.371
NCA cathode from 18650 cells	POS2	0.504	-	0.080	0.026	0.390

Table 9: Volume fractions of composite electrode constituents.

The graphite anode with 20wt% Si (NEG4) was the only one that had two types of binder used in its construction: PAA and SBR. For this electrode, the two binders were homogenized first using the M-T method, and then the homogenized binder was used as the matrix material to homogenize the entire electrode. The calculated effective Young's Moduli (E_{eff}) and Poisson's Ratios (v_{eff}) of the composite electrodes are listed in Table 10 below. Additionally, nanoindentation experiments were conducted on the dry electrodes NEG3, NEG4, and POS2 to compare the homogenization scheme to experimental results. The Poisson's Ratios calculated via the M-T method were used to calculate the Young's Moduli for the nanoindentation tests. A literature survey yielded a publication by Weng et al. [112] which characterized a graphite anode, which is comparable to NEG1 and NEG2, and an NCA cathode, which is similar to POS2, to further compare the results of the homogenization to published data. Even though the volume fractions

of the constituents in the publication may not be the same, they are usually close, as evidenced by the volume fractions listed in Table 9. Therefore, the mechanical properties found via tensile tests by Wang et al. are expected to be close to those of NEG1/NEG2 and POS2. The Young's Modulus reported by Wang et al. was found for the longitudinal (in the direction of the jellyroll winding) and transverse directions, which are listed as E₀ and E₉₀, respectively.

	M-T Homogenization		Nanoinde	entation	Literature	
Electrode	E _{eff} [GPa]	$V_{ m eff}$	E [GPa]	ν	E₀ [GPa]	E ₉₀ [GPa]
NEG1	2.503	0.223	-	-	3.640	3.640
NEG2	3.008	0.226	-	-	3.3.0	
NEG3	1.914	0.216	1.566±0.430	0.216	-	-
NEG4	2.372	0.213	2.723±0.933	0.213	-	-
POS1	2.556	0.193	-	-	-	-
POS2	2.600	0.180	2.748±0.919	0.180	3.620	2.500

Table 10: Comparison of effective elastic properties calculated using M-T homogenization with experimental and published results.

Even though there is some variation between the calculated, experimental, and published values for the elastic properties of the electrodes, the results are close. This indicates that the assumptions made for the homogenization model are accurate enough to produce realistic results. Researchers usually rely on published or analogous mechanical properties of electrodes for mechanical simulations, but this methodology is able to provide accurate predictions for composite electrodes with varying amounts of active materials, binder, conductive additive, and void space.

4.4: Volumetric Expansion of Active Material and Porosity Reduction

One of the most fundamental ways to quantify the expansion of active materials is by examining the volumetric change of unit cells in a crystal lattice. X-ray diffraction (XRD) is a reliable method to measure the change of lattice parameters and is therefore relevant to this modeling effort. A literature survey was conducted to find the volumetric changes in graphite [93], NCA [113], and various types of NMC [114] as a function of lithium content. The volume

change as a function of lithium content for graphite, NCA, and NMC is shown in Figure 37-Figure 39, respectively. The publication used for NCA contained two plots: one for the "a" lattice parameter, and one for the "c" lattice parameter. Since high-nickel content active material is known to have a hexagonal structure, the volume change for the unit cell was calculated. The volumetric expansion of silicon was assumed to be linear in the form of 1+2.7x, where x is the state of lithiation [115], to achieve the theoretical 370% volumetric increase.

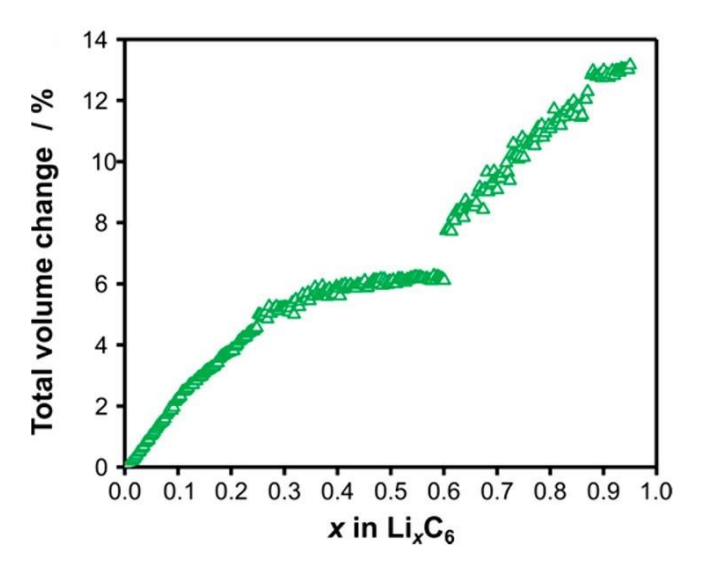


Figure 37: Graphite volume change as a function of lithium content from Schweidler et al. [93].

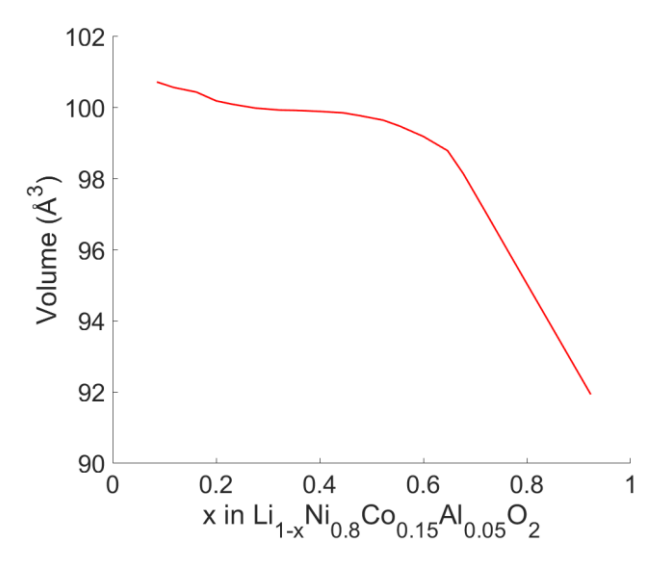


Figure 38: NCA volume change as a function of lithium content calculated using data from Robert et al. [113].

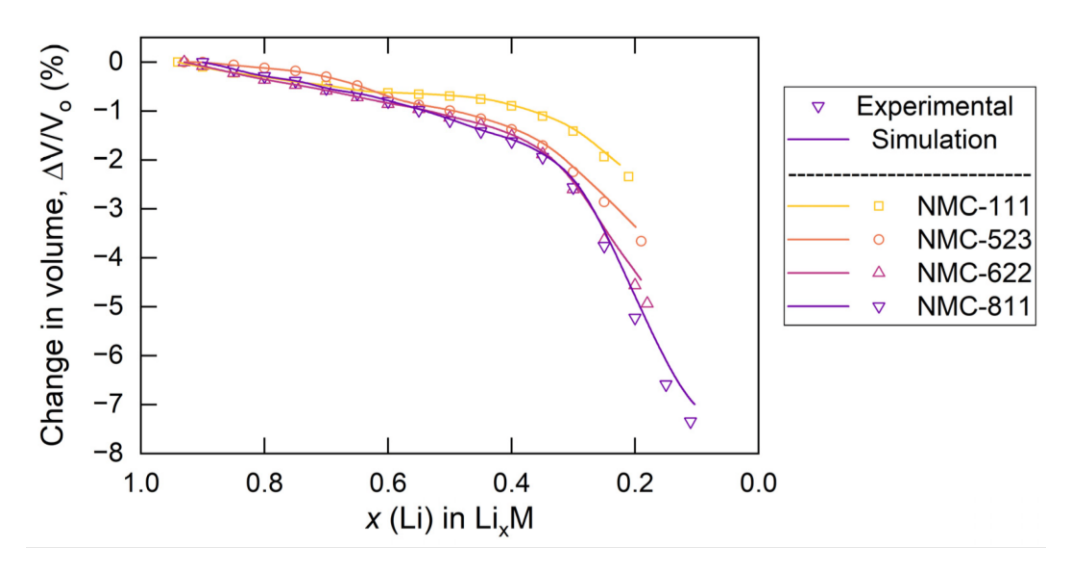


Figure 39: Volume change as a function of lithium content for various NMC chemistries from Iqbal et al. [114].

Since the porosity reduction in electrodes is caused by the expansion of the active material, it is reasonable to assume that it will have the inverted trend of the active material volume change. An example of 22% porosity decrease in a graphite anode is shown in Figure 40 below.

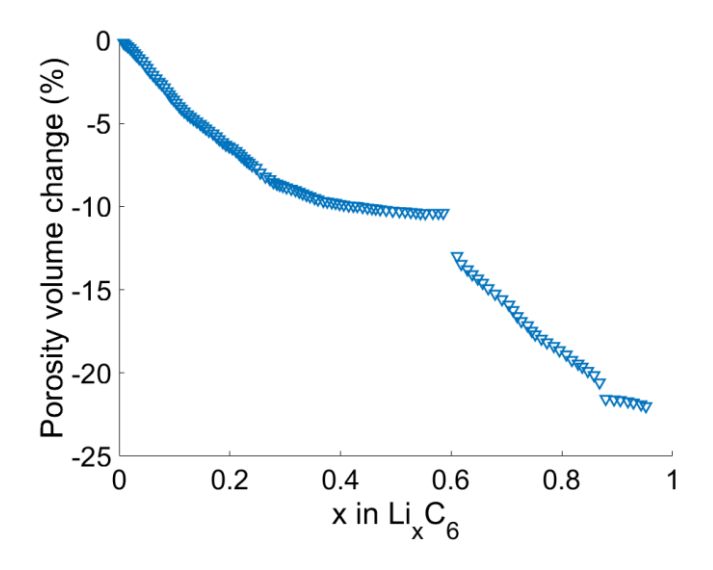


Figure 40: Assumed trend of 25% porosity reduction in a graphite anode.

The active material volume change and porosity reduction were used to calculate the total volume change of each electrode. Since the binder and CA are taken as incompressible, their volume remains the same. As an example, a graphite anode with 22% volume reduction will be

examined. The volume fractions of each of the components are given in Table 11 below.

Variable	Value	Description
Фам	0.67	Volume fraction of active material (graphite).
Фв	0.04	Volume fraction of binder (PVdF).
Фса	0.03	Volume fraction of CA.
ФР	0.26	Volume fraction of porosity/void space.
dV _{AM}	f(x)	Active material (graphite) volume change, function of lithium content (x).
dV₽	f(x)	Porosity/void space volume change, function of lithium content (x).
dV _{AM, Max}	0.13	Maximum volume change of active material (graphite).
dV _{P, Max}	0.22	Maximum volume change of porosity.

Table 11: Variables used for COMSOL simulation.

The initial volume fraction of each constituent is taken as the normalized volume. Then, the volume change of the active material and porosity is calculated as shown in Equation 68 and Equation 69 below, respectively.

$$V_{AM} = \phi_{AM} (1 + dV_{AM}(x))$$
Equation 68

$$V_P = \phi_P \big(1 - dV_P(x) \big)$$

Equation 69

The volume change of porosity (dV_P) will be dependent on the active material, which in this case is graphite.

$$dV_P(x) = dV_{AM}(x) \left(\frac{dV_{P,Max}}{dV_{AM,Max}} \right)$$

Equation 70

The volumes of all of the constituents are then added together to calculate the total volume change of the electrode. As an example, the electrode-scale volume change for the anode

studied by Nadimpalli et al. [31] is shown in Figure 41 below.

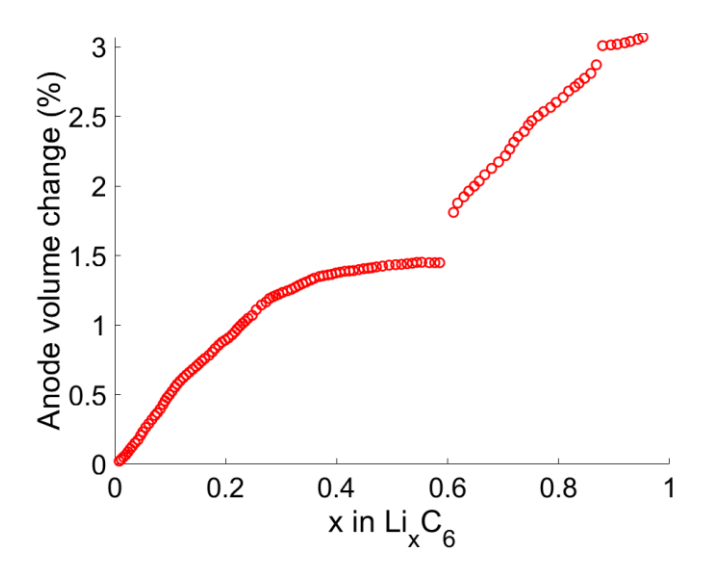


Figure 41: Volume change of a graphite anode with a 22% reduction in porosity.

A similar approach is taken with the cathode, where the initial porosity is taken with the cathode in the fully lithiated state. During delithiation, the active material of the cathode shrinks, and the porosity increases. No data could be found about the porosity change within the cathode, so a small 1% change was assumed.

4.5: COMSOL Finite Element Analysis (FEA) Setup

The COMSOL model used two physics interfaces: Lithium-Ion Battery (liion) from the Batteries and Fuel Cells module and Solid Mechanics (solid) from the Structural Mechanics module. This section will focus on the geometry and boundary conditions used for the simulations. The average state of charge of the simulated electrode(s) was used to calculate the volumetric expansion of the active material(s) based on the data shown in Figure 37-Figure 39 using Equation 68-Equation 70. For the anode with additional silicon active material, the silicon volume expansion was calculated similar to Equation 60, and the presence of silicon taken into account for porosity reduction in Equation 62. The volume change of the electrode, dV, was applied in the Solid Mechanics module to the electrode domain as a thermal strain, dL. Since the electrode is considered to behave isotropically at the macro scale, the thermal strain dL is simply one third of the volumetric change dV.

4.5.1: Half-Cell Simulations

The electrodes simulated in a half-cell configuration include NEG1, NEG3, POS1, and POS2 as listed in Table 10. The NEG1 anode was first used to evaluate the accuracy of the M-T homogenization and electrode volume change approach. The NEG3 anode represents those of the 18650 cells and is therefore of interest. A 2D axisymmetric geometry was used for all the cells to replicate the specimens used for stress measurements. The geometry shown in Figure 42 was shortened to resolve the layers visually and show the comparison of layer thicknesses. The actual cell geometry had a 1 inch radius, and the thickness dimensions are listed in Table 12 below.

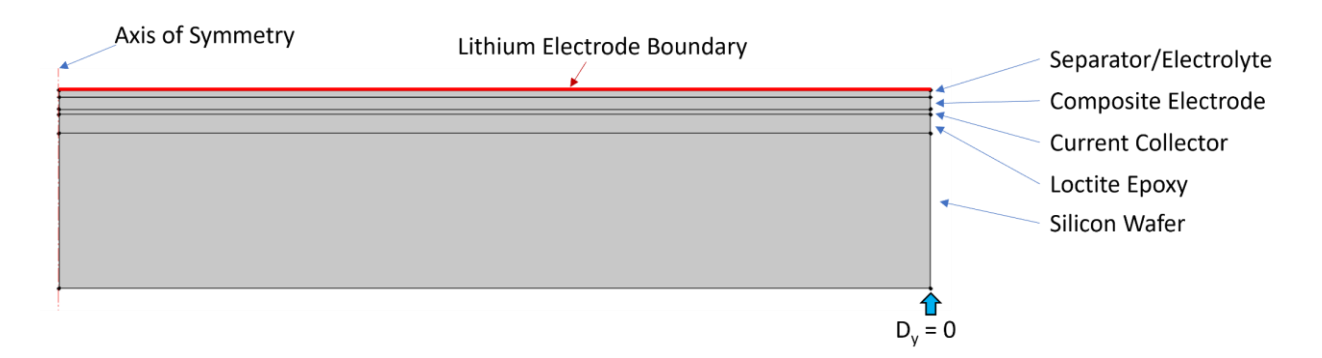


Figure 42: 2D Axissymmetric model of a half-cell.

The model consisted of a separator, composite electrode, current collector, epoxy, and silicon wafer (substrate) domains. Only the separator, composite electrode, and current collector domains participated in the electrochemistry simulation. All domains except the separator were used for the solid mechanics simulation.

For the electrochemistry simulation, the top boundary of the separator was specified as the lithium metal "electrode surface" boundary. A "separator" domain was used for the separator, defining a 40% electrolyte content. The composite electrode was modeled using the "porous electrode" domain. The volume fraction of the active material was defined as listed in Table 9. The liquid electrolyte volume fraction was the same as the porosity of each electrode. For NEG3 and NEG4 anodes, the silicon content was included using the "additional porous electrode active material" domain, with the volume fraction as specified by ϕ_{AM2} in Table 9.

	NEG1	NEG2	NEG3	NEG4	POS1	POS2
h _{separator}	20 μm					
h _{electrode}	47 μm	35 μm	95 μm	60 μm	35 μm	80 μm
h _{current collector}	18 μm	15 μm	10 μm	10 μm	15 μm	16 μm
h _{epoxy}	60 μm	55 μm	50 μm		55 μm	50 μm
h _{substrate}	450	μm	350 μm		450 μm	350µm

Table 12: Half-cell layer thicknesses.

For the solid mechanics simulation, the volumetric changes of the electrode were calculated using the "Variables" definitions during the simulation, resulting in the dL thermal strain value. All of the domains used in the simulation (composite electrode, current collector, epoxy, and silicon wafer substrate) were the "linear elastic material" domains. The analogy between lithiation-induced and thermal stress is well-established in literature [116–118] and is leveraged in this study as well. The linear elastic domain of the porous electrode was given the "Thermal Expansion" load type, where the input type was chosen to be a user-defined thermal strain of magnitude dL. Since the specimen is simply supported and allowed to curve, the outer edge of the silicon substrate was given the zero displacement boundary condition in the y direction, as shown in Figure 42.

4.5.2: Full 18650 Cell Simulations

The simulation setup for the 18650 full cell was similar to the half-cell listed above. Two combinations were simulated: graphite anode (NEG1) with NMC111 cathode (POS1) and graphite anode with 5% silicon content (NEG3) with NCA cathode (POS2). The first combination is similar to the chemistry studied by Sethuraman et al. [30] and Nadimpalli et al. [31], while the second is representative of the 18650 cells studied in this work. The cell cross section with the layer thicknesses and jellyroll details are shown in Figure 43 for the first combination. The second combination of electrodes (NEG3/POS2) is similar, with the main differences in the absence of a mandrel and the thicknesses of the electrodes, which are specified in Table 13.

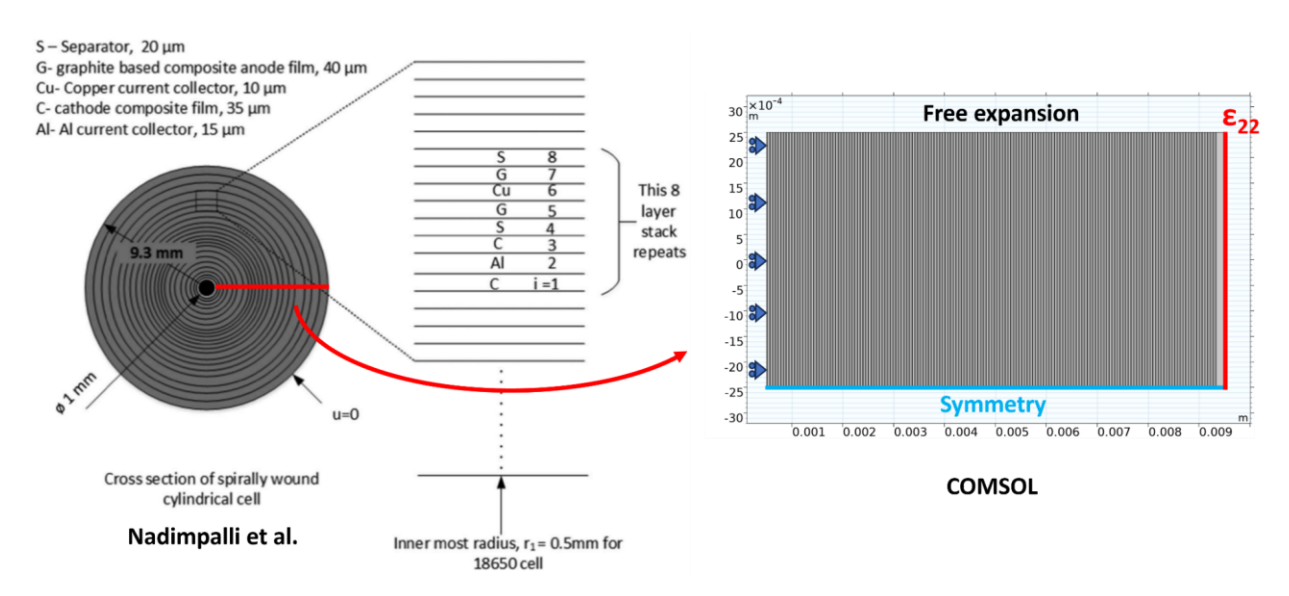


Figure 43: Cell cross section from Nadimpalli et al. [31] and 2D axisymmetric COMSOL model with a mandrel at the cell's center and steel casing on the outside of the jellyroll.

Parameter	Symbol	Value
Jellyroll inside diameter	r _i	3.2 mm
Jellyroll outside diameter	r _o	9.1 mm
Anode thickness	h _{neg}	95 μm
Cathode thickness	h _{pos}	80 μm

Table 13: Details of the tested 18650 cell parameters, as measured from the CT images.

A full height 18650 cell would take significant resources to simulate. Therefore, a "slice" of an 18650 cell was modeled. Most of the simulation setup for the 18650 slice was similar to a half cell, including use of the "porous electrode," "additional active material," "electrode," and "separator" domains. The use of "linear elastic material" model was also mostly the same, with the "Thermal Expansion" load type applied to the anode and cathode layers. The additional considerations used to model the 18650 slice are explained below.

A jellyroll consists of two current collectors, which are coated with electrode material on both sides, with a separator in between the anodes and cathodes. This stack is then wound into a spiral shape and placed into a casing. Each electrode and separator combination are simulated in a similar fashion as shown in Figure 42, with the same type of electrode contacting the current collector (anode contacting copper, and cathode contacting aluminum), and the opposite type

across the separator. The galvanostatic current was applied to the outer boundary of the copper current collector domain, similar to a half cell. The positive aluminum current collector was grounded, which is similar to how the lithium electrode boundary is treated in the half-cell configuration. The outer-most layer of the 18650 slice geometry was the steel casing, which did not participate in the physics of electrochemistry.

While the electrolyte-filled separator in a half-cell configuration does not constrain the electrode and is therefore not included in solid mechanics physics, this is not the case in a full cell. Therefore, the entire slice geometry is included in the mechanical simulation of the electrode. The Young's Modulus and Poisson's Ratio used for the separator material are 0.1 GPa and 0.3 [119]. The average SoC of active materials was used to calculate the volume change of the electrodes, which was then applied as a thermal strain to the electrode domains.

For the NEG1-POS1 simulation, the electrodes were comparatively thin, resulting in a total of 41 jellyroll layers. The center of this cell had a mandrel with a 0.5 mm radius, which was represented by a roller support on the inner surface of the jellyroll. The hoop strain, represented by ϵ_{22} , was measured using a boundary probe along the outer surface of the steel casing. The electrodes in the NEG3-POS2 combination were thicker, and the jellyroll consisted of only 19 layers. The center of this cell was hollow, as seen in Figure 7c. Therefore, the center of the jellyroll did not have constraints and was left free to expand.

4.6: Simulations Results and Comparison to Published Data

4.6.1: Half-Cell Simulation Results

The half-cell electrochemical simulation results are shown in Figure 44 below for a graphite anode (NEG1) and an NMC111 cathode (POS1). The simulation and experimental results for the anode are close, with the staging behavior under 0.2V closely matching. This is not the case with the anode results, though the comparison is not straightforward. The cathode studied by Nadimpalli et al. was Li_{1.2}Ni_{0.15}Mn_{0.55}Co_{0.1}O₂, for which mechanical properties and volumetric expansion data could not be located. Therefore, instead a LiNi_{0.33}Mn_{0.33}Co_{0.33}O₂ cathode was used for simulations. Even though the electrochemical behavior of the two is different, the overall trend is similar.

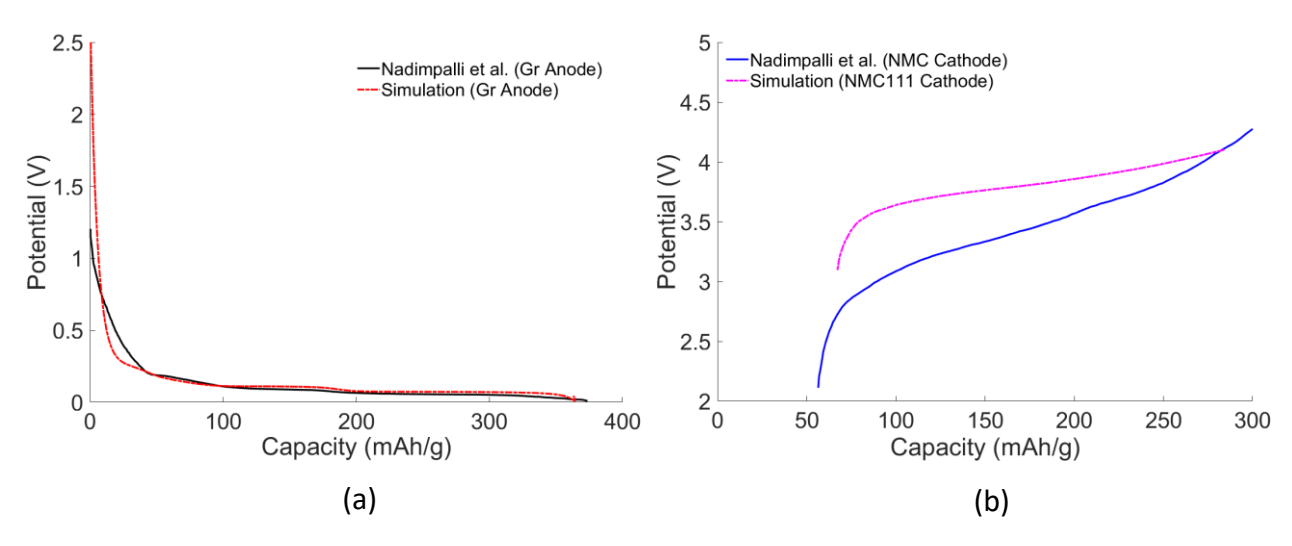


Figure 44: Experimental [31] and simulated cell potential for (a) graphite anode and (b) NMC cathode half cells.

The simulated stress due to active material volume expansion is shown in Figure 45 below for NEG1 and NEG2, as well as the published data from Sethuraman et al. [30] and Nadimpalli et al. [31]. The simulated stress for NEG1 anode is in good agreement with published data, signifying that the assumptions made for the M-T homogenization and volumetric changes are accurate. The results for NEG2 anode with 5% silicon content are shown in Figure 45. It was assumed that the expansion of the additional active material (i.e., silicon) would cause a more drastic reduction in porosity, which was therefore set to 25%. Even with the higher porosity reduction, the magnitude of the predicted stress is fairly high. Preliminary stress measurements for an anode with 5% silicon content in Figure 53 show ~17 MPa of stress during lithiation, which is lower than the ~25 MPa predicted.

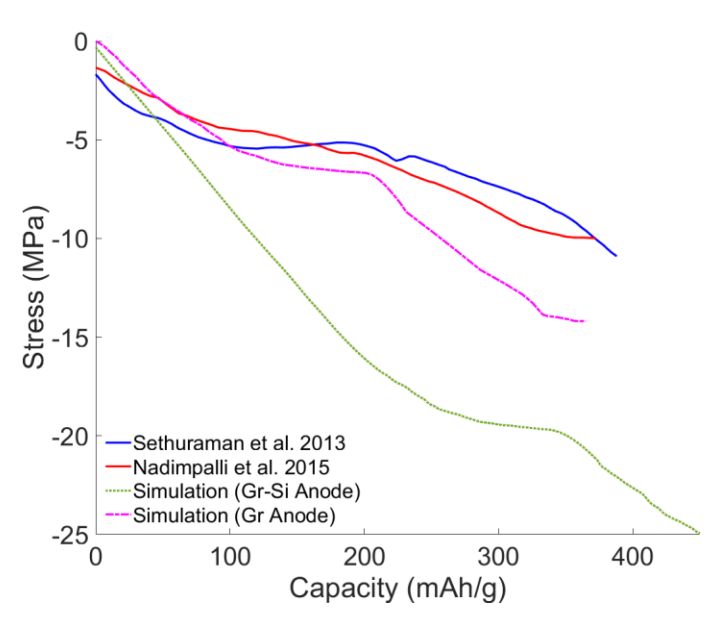


Figure 45: Experimental [30,31] and simulated anode stress response as a function of half-cell capacity.

There are three considerations which could improve the accuracy of the graphite-silicon anode. The first is the actual porosity reduction within the electrode. For the current simulations, an assumption is made within the range suggested by Qi and Harris [106]. A more rigorous way to estimate the porosity change would be to apply the relations used by Sikha et al. [105], which could improve the accuracy of predictions. The second consideration is the reference exchange current density of the silicon active material. The value used for this was 4 mA/cm², which is significantly higher than that of graphite. Based on the shape of the stress plot, the silicon material fully lithiates prior to graphite, as evidenced by the location of the change in the stress slope around 280 mAh/g in Figure 45. By comparison, this slope change occurs much earlier in the cycle during stress measurement, as shown in Figure 53. Although a change in the reference exchange current density for silicon will not affect the overall stress magnitude, it could make the shape of the stress plot more accurate by delaying the lithiation, and thereby volumetric expansion of silicon. The third consideration is the practical SoC range of the silicon active material. During the simulation, the average SoC of silicon evolves from 0% to 99%, which leads to the nearly full 370% volumetric expansion. Practically speaking, the silicon particles should have a much smaller SoC range, which would reduce the total stress magnitude.

The simulated stress profiles for POS1 and POS2 cathodes are shown below in Figure 46a and Figure 46b, respectively. Since no experimental stress measurements have been published

for NMC111 and NCA, the most relevant comparison is the electrode data published by Nadimpalli et al. [31]. Although the chemistry is not the same, the overall shape and magnitude of the volume change in Figure 46b is similar between the published and predicted cathode stress. The NCA active material experiences a higher volumetric change during cycling, which is reflected in the higher magnitude of compressive stress for the POS2 cathode. The overall shape of the stress plot is similar between the cathodes.

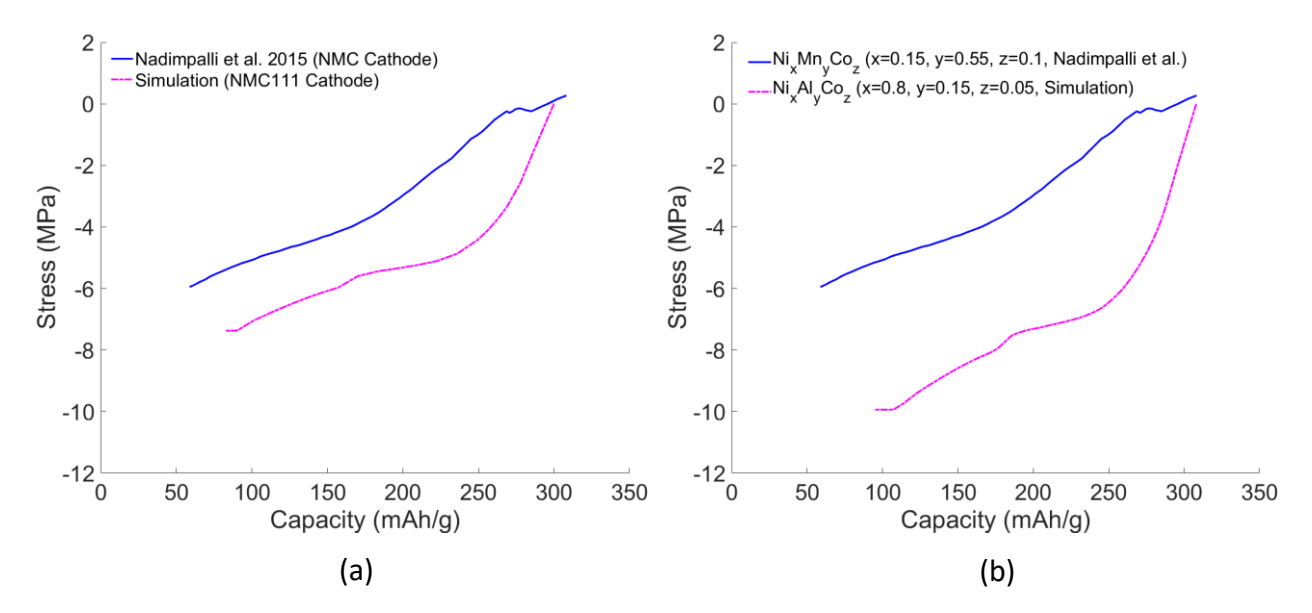


Figure 46: Experimental [31] and simulated results for published NMC cathode stress compared with simulated (a) NMC111 and (b) NCA cathode stresses.

One of the limitations of the approach used is the availability of full volumetric change data. The available volumetric change data for NMC111 was between approximately 96% and 21% SoC of the cathode. While this range is close to the practical cycling range for cathodes, the volumetric changes of a more complete SoC range would be useful. Additionally, a 1% porosity reduction was assumed for the cathodes. Further research into this area is necessary to determine whether this amount is reasonable and could be higher for electrodes with NCA and NMC811 active material.

4.6.2: Full Cell 18650 Simulation Results

The predicted strain on the surface of an 18650 cell is shown in Figure 47 below for NEG1-POS1 and NEG3-POS2 electrode combinations, along with the measured strain from one of the

18650 cells from this study. While the NEG1-POS1 combination is merely for comparison purposes, the magnitude of the predicted strain is close to the cells assessed in this study. The NEG3-POS2 chemistry is representative of the 18650 cells used, but there is some disagreement between the predicted and experimental data. As discussed previously, it is suspected that the reference exchange current density and the practical SoC range of the silicon material need refinement.

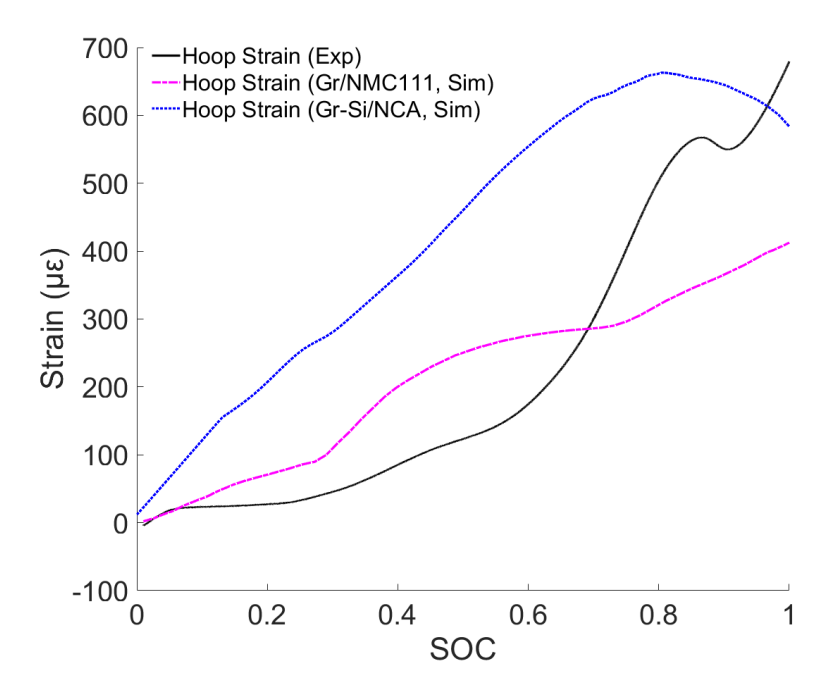


Figure 47: Predicted strain on the surface of an 18650 cell for a graphite - NMC111 and graphite/Si – NCA chemistries, compared to measured strain.

The porosity change within the cathode and SoC range of silicon have practical applications in battery design. The porosity within electrodes is necessary for transporting Li⁺ ions through the electrolyte. If the porosity within electrodes reduces significantly, either as a whole or in specific regions, the kinetics of the electrochemical reactions could be affected. If regions of the jellyroll become devoid of electrolyte, this could lead to unutilized active material, reducing a battery's capacity.

The SoC range of the silicon active material can be useful for estimating the stress the particle could experience during cycling. The critical size for a silicon particle which could cycle fully without fracture is approximately 150 nm [120], which is much smaller than the size of the particles seen by the SEM. By estimating the SoC range of the silicon accurately during cycling, a

prediction could be made for the amount of volumetric expansion these particles would experience. Such a prediction would be useful for informing design of additional active material within future electrodes, and lead to lower capacity fade.

With further refinement, this model has the potential to predict the strain at the battery level. This information would be especially useful for battery pack design, as engineers would have an estimate of battery expansion for various chemistries and cell formats. If cells are constrained and not allowed to expand, the volumetric changes could lead to buckling or kinking of the jellyroll, which could cause premature failure. Placing the cell too far apart, however, would increase the size of the battery pack and may be disadvantageous to cooling.

Predicting the surface stress accurately would also aid in the development of strain-based health monitoring for cells. While characterizing the mechanical behavior of each cell chemistry is feasible, being able to predict healthy surface strain would save designers much time and resources. As mechanical models improve, quantification of cell ageing and degradation can also be modeled, aiding in the prediction of the useful life left.

CHAPTER 5: CONCLUSION

5.1: Baseline Strain Behavior

The surface strain behavior of 18650 cylindrical cell with a Ni-rich layered oxide cathode and graphite-Si anode was measured under normal operating conditions as well as overcharge (electrical abuse) conditions. The relation between the surface strain and electrochemical behavior of the cell was thoroughly investigated. Differential capacity (dQ/dV) and strain (d ϵ /dV) analyses showed a clear correlation between the electrochemical and strain response of the cells, which was generally repeatable and reversible over multiple cells and cycles, even at increasingly higher C-rates. It is interesting to see that all differential strain (d ϵ /dV) peaks almost always preceded or coincided with those of differential capacity (dQ/dV). During normal cycling, the hoop strain reached a peak of 570±109 $\mu\epsilon$ at 80% SoC during charge process. At increasingly higher C-rates the peak strain grew in magnitude due to a rise in cell temperature and shifted towards a higher potential during charge and a lower potential during discharge. It was observed that even at higher C-rates (C/2 and 1C for discharge) the peak strain still occurred at 80% SoC. While a notional connection between strain and the discrete electrochemical reactions occurring in the anode and cathode was made in this study, future work will focus on interrogating the strain response of individual electrodes.

Despite the complex microstructure of composite electrodes, various constituents of jelly roll, and the overall construction of the cell, a clear and strong correlation between the electrochemical reactions (or cell potential and the phase changes) and the surface hoop strain of the 18650 cell was observed. The correlation between strain and electrochemical behavior of the cells shows that strain could be a useful metric for monitoring the health of a cell and electrode behavior *in operando* and introduces the possible application of strain as a method to monitor irreversible phenomenon. The reversible strain profile during normal cycling supports the feasibility of using strain measurements as a metric for a battery's physical state. This work describes a general approach which could be applied to other cathode and anode materials which will generate unique SoC dependent strain behaviors. Since almost all the active materials (both anode and cathode) experience volume changes during electrochemical reactions, it follows that their effect will be reflected in the surface strain as shown in this work.

5.2: Strain Behavior During Overcharge

Overcharge experiments also confirmed the idea, showing a large buildup of strain preceding CID activation and temperature rise. The strain level immediately before CID activation reached 2.5 times the strain at 100% SoC, of which a relatively low amount was due to temperature increase. An analytical evaluation of the cell showed that if the strain generated during over charge was solely due to gas generation, then the CID should have activated much sooner than witnessed in the experiment. Therefore, the strain increase during overcharge is only partially attributed to gas generation in the cell. Heating of overcharged cells showed repeatable events in the strain data which could be considered the precursors to thermal runaway. Currently, BMS systems cannot monitor the state of cells once the CID has been activated. In this scenario, strain measurements could provide valuable information about the internal state of cells that would otherwise be unavailable to aid in TR prediction and prevention.

The effect of repeated overcharge on the surface strain and temperature behaviors of cells was evaluated was evaluated as well. Whereas most repeated overcharge studies focus on overcharging cells to a specific voltage [52–54,57–59], the cells in this study are overcharged to a specific capacity, which is rarely seen in literature. The modes of cell degradation were determined using ICA and EIS analyses. A parameterized equivalent circuit model was used to fit the gathered EIS spectra.

Repeated overcharge to 105% of nominal capacity (5% OC) was shown to be mild, with the maximum strain and temperature increasing relatively slowly over the course of 12 cycles. The residual strain was seen to increase after the third cycle but did not increase significantly after. Repeated overcharge to 110% of nominal capacity (10% OC) was shown to cause more irreversible reactions, as evidenced by a steady and relatively substantial increase in maximum strain in temperature as well as the rapid decline of the cyclic capacity after the 3rd cycle. During repeated 10% OC samples failed after 11±2 cycles, during which the residual strain steadily increased. When modeled as a pressurized cylinder, the residual strain on the casing correlated closely to the pressure required for CID activation. While effort has been made to quantify internal cell pressure through strain measurement [121], it is primarily focused on thermal abuse of a battery. The usage of residual strain as a prediction tool for CID activation is novel and can

be extended to cells with various electrode chemistries and size formats.

Differential/incremental capacity analysis (ICA) revealed that during 10% OC abuse the electrochemical peaks do not reduce in magnitude but shift towards a higher potential. This phenomenon is usually correlated with the LLI failure mode and is mirrored by the differential/incremental strain (ISA) plots. To the best of the authors' knowledge, this relationship is a novel finding and implies that strain can be used to detect cell degradation modes similar to ICA. Furthermore, the reversible strain generated during overcharge provided insight into the mechanisms present during the abuse portion of the experiments.

Electrochemical impedance spectroscopy (EIS) was conducted every three cycles during 10% OC to evaluate the changes in electrochemical parameters in a cell. The collected spectra were fitted to a parameterized equivalent circuit model which showed growing ohmic (R2), SEI (R3), and charge transfer (R4) resistances, yet little change in the Warburg coefficient (W5). The EIS analysis results match the conclusions drawn from ICA and ISA that LoC and LLI are the main degradation modes during this type of electrical abuse, with little LAM observed. This is corroborated by the strain data collected during this study, which also aids in providing further insight into the specific degradation mechanisms present.

The results from this study support the utility of strain measurements as a diagnostic method for tracking battery state-of-health (SoH) during overcharge conditions. The capabilities of predicting CID activation and detecting electrochemical degradation modes through strain are showcased. ICA and EIS analyses correspond to the possible DM's present but cannot provide insight into the mechanical state of a cell or predict its CID activation during this type of abuse. A cell's strain signature is shown here to provide additional insight into its mechanical state, further narrow down the degradation modes, and predict a cell's failure. Though this work is done for graphite-silicon and NCA chemistry, this technique can be extended to other anode and cathode chemistries as well. Since most active materials undergo volumetric changes during electrochemical reactions, their strain signatures can be analyzed non-destructively on the surface of a battery, providing real-time information.

5.3: Battery Modeling and Simulations

This work showcases the utility of the M-T homogenization scheme with Eshelby formulation for predicting the mechanical properties of electrodes. As confirmed by mechanical characterization of electrodes using micro indentation and data published in literature, the assumptions made are accurate. When the cycling rates are fairly slow (i.e., the viscous behavior of constituents is not significant), the electrodes behave as isotropic linear elastic composites at the macro scale. This homogenization technique could allow engineers to calculate the effective mechanical properties for a variety of electrode chemistries and volume fractions of constituents.

A variety of anodes and cathodes were simulated in COMSOL Multiphysics FEA software to predict their electrochemical and mechanical behavior. By using the active material's volume change data as a function of lithium content in combination with the homogenized mechanical properties, accurate stress predictions were made. Graphite anodes with additional silicon content did not have published stress data available for comparison, but preliminary stress data from measurements described in APPENDIX A suggest that further refinement of this model is needed to capture accurate behavior. This is further supported by 18650 battery modeling results, where the magnitudes of the predicted strain are comparable to experimental data, with the strain profile needing improvement.

There are a number of changes planned for this model prior to publishing this work in a journal. The reference exchange current density and porosity reduction of electrodes need to be explored in more detail. Furthermore, there is evidence that silicon within the anode is not being fully utilized and has a limited SoC range during cycling. However, further analysis is needed before any estimates can be made. Additional refinements to this model are related to the assumptions made during the M-T homogenization development. Specifically, the mechanical properties of the electrode constituents are considered to be constant. In reality, the Young's Modulus of active materials is a function of lithium content and will be accounted for in the future. The M-T homogenization scheme will also be performed within the COMSOL environment, allowing the composite electrodes to be homogenized throughout the simulation to reflect the actual volume fractions of the constituents. These improvements are planned for the near future and are expected to improve the accuracy of simulation results.

The model developed during this research was designed to use fundamental inputs, such as the elastic material properties and active material volume change data, to predict the mechanical behavior at the battery level. This model can be a powerful tool for engineers and designers to predict the mechanical behavior of batteries with various chemistries and formats. This information can be used in battery pack design and also can aid in the development of a strain-based health monitoring and TR detection method.

5.4: Future Work

5.4.1: Strain-Based Health Monitoring and TR Detection

Throughout this work strain on the surface of 18650 cells was characterized at a variety of C-rates, overcharge, and heating to TR. One of the important parameters this work would benefit from is dependence on temperature. Li-ion batteries are known to operate in a narrow temperature range, such as 5°C to 45°C specified by the manufacturer for this cell. However, operation at these temperature extremes may cause lithium plating and accelerated cell ageing, respectively. For a thorough study of temperature effects, the baseline experiments should be repeated at varying temperatures, ideally in increments from 5°C to 45°C. The ICA and ISA analyses should be performed and changes in peaks studied. In an idea scenario, the cells would then be punctured in a closed container with a pressure sensor to determine the amount of gas built up inside, if any. The rest of the cell should be disassembled thereafter and analyzed for changes in chemical composition, surface morphology, and crystal structure.

Temperature can also be a significant factor in the overcharge experiments. Though temperature could not be controlled during any of the tests conducted, the abuse chambers were usually at approximately 30°C. Ideally, the overcharge experiments should be repeated while the cells are held at constant temperatures, also between 5°C to 45°C, to determine the effects of temperature on gas generation and degradation modes. Also, EIS should be conducted every cycle when a cell reaches a specific SoC after being discharged to 0%. This would provide a deeper understanding of the types of ageing mechanisms present during overcharge, and how mechanical measurements can aid in detecting them. This is also true with overdischarge, as the feasibility of detecting lithium plating through strain measurements was never tested.

Certain features in the strain signature were identified during heating to thermal

runaway, namely the decrease in strain magnitude and vent activation. While these events can be identified in data analysis after the tests, the feasibility of identifying them in real time still needs to be tested. Furthermore, these measurements will likely be taken in an environment where vibration, shock, and electromagnetic noise are present. The ability of a system to identify the strain features in such an environment needs to be determined as well.

Finally, this work is limited to a single cell chemistry. Logically, cells with any active materials which undergo volumetric changes during cycling should be able to benefit from this methodology and the conclusions drawn from this work, but this hypothesis still needs to be tested. Additionally, this approach may be extended to other types of secondary batteries (sodium-ion, potassium-ion, etc.) as well.

5.4.2: Battery Modeling

The battery model used in this dissertation is based on many assumptions. The preliminary results show agreement with published values for electrode mechanical properties and stress during cycling, but this model has limitations. The isotropic linear elastic assumption for the constituents of the composite electrodes may yield realistic results for small stress magnitudes and slow cycling rates but limits the model. Auto manufacturers, for example, strive to develop infrastructure and vehicles which can recharge in as little time as possible. If a vehicle's battery pack regains 75% of its capacity in 20 minutes, the cells are charging at an average C-rate of 2.25C, and actual peak C-rates seen by cells could be even higher [122]. In this scenario, the materials within electrodes may not behave in a linear elastic fashion anymore. For example, the polymeric binder may exhibit viscoelastic behavior. In relation to small magnitudes of stress, this assumption is still valid for active material with low volumetric expansion, such as LTO, but is not applicable for high capacity active materials, such as Si, which is included in many modern anode architectures. Upon full lithiation Si undergoes a 270% volumetric expansion, which can generate a significant amount of stress if not designed properly, which will lead to short cycle life of the silicon active material [99]. Furthermore, Si was found to behave in an elastic-viscoplastic manner upon lithiation [123], which may reduce the accuracy of the model's predictions if not accounted.

The coupling of electrochemistry and mechanics is currently sequential. That is, electrochemistry is solved by the P4D model and is for the most part independent of the

mechanics, except in the case of geometric changes and porosity reduction. In reality, mechanics and electrochemistry affect one another. For example, stress effects both the diffusion of Li into active materials [116,124] and the cell potential [76]. The current model does not account for either of these phenomena, which could be significant when increasingly large amounts of high volume expansion materials are utilized. The dependence of electrical and chemical properties of active materials on stress would need to be determined experimentally.

Another important point is that the presented model has only been verified for a graphite anode. The NMC comparison was not representative since the chemistries of the published data and the simulation were different. Hence, experimental data is needed to validate the model's accuracy for a cathode material. This is true as well for electrodes with more than one active material, such as the anodes in the 18650 cells analyzed in this study. The stress data for these electrodes, as well as ones with a higher silicon content, would need to be recorded experimentally to test the limits of this model.

Furthermore, the presented model is only accurate for healthy cells (i.e., near 100% SoH) and does not include cell ageing or any thermal effects. While effective thermal properties for the composite electrodes could be determined through homogenization [125,126] the effect of temperature on cell ageing is much more complex. The various active materials used in electrode designs experience degradation mechanisms (irreversible phase changes, SEI growth, etc.) at different temperatures and cell potentials, which need to be determined experimentally.

Future iterations of this model would need to take many of these limitations into account and make appropriate changes. Including the various material behaviors, material properties as a function of lithium content, and temperature effects would be beneficial to predicting accurate mechanical response of a cell. Such data could be useful for designing cells and battery packs for various cell chemistries.

BIBLIOGRAPHY

- [1] ANSYS, Common Primary Battery Chemistries, (n.d.). https://www.ansys.com/it-it/blog/common-primary-battery-chemistries (accessed August 11, 2024).
- [2] W. Xu, J. Wang, F. Ding, X. Chen, E. Nasybulin, Y. Zhang, J.G. Zhang, Lithium metal anodes for rechargeable batteries, Energy Environ. Sci. 7 (2014) 513–537. https://doi.org/10.1039/c3ee40795k.
- [3] N. Nitta, F. Wu, J.T. Lee, G. Yushin, Li-ion battery materials: present and future, Mater. Today 18 (2015) 252–264. https://doi.org/10.1016/j.mattod.2014.10.040.
- [4] J. Li, L.E. Downie, L. Ma, W. Qiu, J.R. Dahn, Study of the Failure Mechanisms of LiNi 0.8 Mn 0.1 Co 0.1 O 2 Cathode Material for Lithium Ion Batteries, J. Electrochem. Soc. 162 (2015) A1401–A1408. https://doi.org/10.1149/2.1011507jes.
- [5] R. Jung, M. Metzger, F. Maglia, C. Stinner, H.A. Gasteiger, Oxygen Release and Its Effect on the Cycling Stability of LiNi x Mn y Co z O 2 (NMC) Cathode Materials for Li-Ion Batteries, J. Electrochem. Soc. 164 (2017) A1361–A1377. https://doi.org/10.1149/2.0021707jes.
- [6] D. Goonetilleke, N. Sharma, W.K. Pang, V.K. Peterson, R. Petibon, J. Li, J.R. Dahn, Structural Evolution and High-Voltage Structural Stability of Li(Ni x Mn y Co z)O 2 Electrodes, Chem. Mater. 31 (2019) 376–386. https://doi.org/10.1021/acs.chemmater.8b03525.
- [7] J.T. Warner, Lithium-Ion Battery Chemistries: A Primer, Elsevier, 2019.
- [8] Q. Wang, P. Ping, X. Zhao, G. Chu, J. Sun, C. Chen, Thermal runaway caused fire and explosion of lithium ion battery, J. Power Sources 208 (2012) 210–224. https://doi.org/10.1016/j.jpowsour.2012.02.038.
- [9] X. Feng, M. Ouyang, X. Liu, L. Lu, Y. Xia, X. He, Thermal runaway mechanism of lithium ion battery for electric vehicles: A review, Energy Storage Mater. 10 (2018) 246–267. https://doi.org/10.1016/j.ensm.2017.05.013.
- [10] W. Li, K.R. Crompton, C. Hacker, J.K. Ostanek, Comparison of Current Interrupt Device and Vent Design for 18650 Format Lithium-ion Battery Caps, J. Energy Storage 32 (2020) 101890. https://doi.org/10.1016/j.est.2020.101890.
- [11] N.S. Spinner, K.M. Hinnant, R. Mazurick, A. Brandon, S.L. Rose-Pehrsson, S.G. Tuttle, Novel 18650 lithium-ion battery surrogate cell design with anisotropic thermophysical properties for studying failure events, J. Power Sources 312 (2016) 1–11. https://doi.org/10.1016/j.jpowsour.2016.01.107.
- [12] E. Darcy, Screening Li-ion batteries for internal shorts, J. Power Sources 174 (2007) 575–578. https://doi.org/10.1016/j.jpowsour.2007.06.245.

- [13] S. Santhanagopalan, P. Ramadass, J. (Zhengming) Zhang, Analysis of internal short-circuit in a lithium ion cell, J. Power Sources 194 (2009) 550–557. https://doi.org/10.1016/j.jpowsour.2009.05.002.
- [14] M. Pharr, K. Zhao, X. Wang, Z. Suo, J.J. Vlassak, Kinetics of Initial Lithiation of Crystalline Silicon Electrodes of Lithium-Ion Batteries, Nano Lett. 12 (2012) 5039–5047. https://doi.org/10.1021/nl302841y.
- [15] L.Y. Beaulieu, K.W. Eberman, R.L. Turner, L.J. Krause, J.R. Dahn, Colossal Reversible Volume Changes in Lithium Alloys, Electrochem. Solid-State Lett. 4 (2001) A137. https://doi.org/10.1149/1.1388178.
- [16] J.T. Frith, M.J. Lacey, U. Ulissi, A non-academic perspective on the future of lithium-based batteries, Nat. Commun. 14 (2023) 420. https://doi.org/10.1038/s41467-023-35933-2.
- [17] J.H. Lee, H.M. Lee, S. Ahn, Battery dimensional changes occurring during charge/discharge cycles—thin rectangular lithium ion and polymer cells, J. Power Sources 119–121 (2003) 833–837. https://doi.org/10.1016/S0378-7753(03)00281-7.
- [18] R. Fu, M. Xiao, S.-Y. Choe, Modeling, validation and analysis of mechanical stress generation and dimension changes of a pouch type high power Li-ion battery, J. Power Sources 224 (2013) 211–224. https://doi.org/10.1016/j.jpowsour.2012.09.096.
- [19] K.-Y. Oh, J.B. Siegel, L. Secondo, S.U. Kim, N.A. Samad, J. Qin, D. Anderson, K. Garikipati, A. Knobloch, B.I. Epureanu, C.W. Monroe, A. Stefanopoulou, Rate dependence of swelling in lithium-ion cells, J. Power Sources 267 (2014) 197–202. https://doi.org/10.1016/j.jpowsour.2014.05.039.
- [20] Z.J. Schiffer, J. Cannarella, C.B. Arnold, Strain Derivatives for Practical Charge Rate Characterization of Lithium Ion Electrodes, J. Electrochem. Soc. 163 (2016) A427–A433. https://doi.org/10.1149/2.0091603jes.
- [21] X. Wang, Y. Sone, S. Kuwajima, In Situ Investigation of the Volume Change in Li-ion Cell with Charging and Discharging, J. Electrochem. Soc. 151 (2004) A273. https://doi.org/10.1149/1.1635827.
- [22] E. Gibellini, C. Lanciotti, R. Giovanardi, M. Bononi, G. Davolio, A. Marchetti, C. Fontanesi, Dimensional Changes in Automotive Pouch Li-Ion Cells: A Combined Thermo-Mechanical/Electrochemical Study, J. Electrochem. Soc. 163 (2016) A2304–A2311. https://doi.org/10.1149/2.0831610jes.
- [23] J. Li, L.E. Downie, L. Ma, W. Qiu, J.R. Dahn, Study of the Failure Mechanisms of LiNi 0.8 Mn 0.1 Co 0.1 O 2 Cathode Material for Lithium Ion Batteries, J. Electrochem. Soc. 162 (2015) A1401–A1408. https://doi.org/10.1149/2.1011507jes.
- [24] X. Yu, Z. Feng, Y. Ren, D. Henn, Z. Wu, K. An, B. Wu, C. Fau, C. Li, S.J. Harris, Simultaneous

- Operando Measurements of the Local Temperature, State of Charge, and Strain inside a Commercial Lithium-Ion Battery Pouch Cell, J. Electrochem. Soc. 165 (2018) A1578–A1585. https://doi.org/10.1149/2.1251807jes.
- [25] L.W. Sommer, P. Kiesel, A. Ganguli, A. Lochbaum, B. Saha, J. Schwartz, C.-J. Bae, M. Alamgir, A. Raghavan, Fast and slow ion diffusion processes in lithium ion pouch cells during cycling observed with fiber optic strain sensors, J. Power Sources 296 (2015) 46–52. https://doi.org/10.1016/j.jpowsour.2015.07.025.
- [26] M. Nascimento, S. Novais, M.S. Ding, M.S. Ferreira, S. Koch, S. Passerini, J.L. Pinto, Internal strain and temperature discrimination with optical fiber hybrid sensors in Li-ion batteries, J. Power Sources 410–411 (2019) 1–9. https://doi.org/10.1016/j.jpowsour.2018.10.096.
- [27] J. Bonefacino, S. Ghashghaie, T. Zheng, C.-P. Lin, W. Zheng, L.A. Blanquer, J. Huang, C. Gervillié, H.-Y. Tam, J.-M. Tarascon, S.T. Boles, High-Fidelity Strain and Temperature Measurements of Li-Ion Batteries Using Polymer Optical Fiber Sensors, J. Electrochem. Soc. 169 (2022) 100508. https://doi.org/10.1149/1945-7111/AC957E.
- [28] J. Xi, J. Li, H. Sun, T. Ma, L. Deng, N. Liu, X. Huang, J. Zhang, In-situ monitoring of internal temperature and strain of solid-state battery based on optical fiber sensors, Sens. Actuators Phys. (2022) 113888. https://doi.org/10.1016/j.sna.2022.113888.
- [29] L.C. Matuck, P.D. Cabrita, J.L. Pinto, C.A. Marques, M.S. Nascimento, Customized Optical Fiber Birefringent Sensors to Multipoint and Simultaneous Temperature and Radial Strain Tracking of Lithium-Ion Batteries, Adv. Sens. Res. 2 (2023) 2200046. https://doi.org/10.1002/ADSR.202200046.
- [30] V.A. Sethuraman, N.V. Winkle, D.P. Abraham, A.F. Bower, P.R. Guduru, Real-time stress measurements in lithium-ion battery negative-electrodes, J. Power Sources 206 (2012) 334–342. https://doi.org/10.1016/j.jpowsour.2012.01.036.
- [31] S.P.V. Nadimpalli, V.A. Sethuraman, D.P. Abraham, A.F. Bower, P.R. Guduru, Stress Evolution in Lithium-Ion Composite Electrodes during Electrochemical Cycling and Resulting Internal Pressures on the Cell Casing, J. Electrochem. Soc. 162 (2015) A2656–A2663. https://doi.org/10.1149/2.0341514jes.
- [32] D.P. Finegan, E. Tudisco, M. Scheel, J.B. Robinson, O.O. Taiwo, D.S. Eastwood, P.D. Lee, M. Di Michiel, B. Bay, S.A. Hall, G. Hinds, D.J.L. Brett, P.R. Shearing, Quantifying Bulk Electrode Strain and Material Displacement within Lithium Batteries via High-Speed Operando Tomography and Digital Volume Correlation, Adv. Sci. 3 (2016) 1500332. https://doi.org/10.1002/advs.201500332.
- [33] Y. Zhao, F.B. Spingler, Y. Patel, G.J. Offer, A. Jossen, Localized Swelling Inhomogeneity Detection in Lithium Ion Cells Using Multi-Dimensional Laser Scanning, J. Electrochem. Soc. 166 (2019) A27–A34. https://doi.org/10.1149/2.0011902jes.

- [34] A. Sonwane, C. Yuan, J. Xu, Coupling Effect of State-of-Charge and Strain Rate on the Mechanical Behavior of Electrodes of 21700 Lithium-Ion Battery, J. Electrochem. Energy Convers. Storage 18 (2021). https://doi.org/10.1115/1.4049042.
- [35] J. Hemmerling, J. Schäfer, T. Jung, T. Kreher, M. Ströbel, C. Gassmann, J. Günther, A. Fill, K.P. Birke, Investigation of internal gas pressure and internal temperature of cylindrical Li-ion cells to study thermodynamical and mechanical properties of hard case battery cells, J. Energy Storage 59 (2023) 106444. https://doi.org/10.1016/j.est.2022.106444.
- [36] S. Mohan, Y. Kim, J.B. Siegel, N.A. Samad, A.G. Stefanopoulou, A Phenomenological Model of Bulk Force in a Li-Ion Battery Pack and Its Application to State of Charge Estimation, J. Electrochem. Soc. 161 (2014) A2222—A2231. https://doi.org/10.1149/2.0841414jes.
- [37] K.-Y. Oh, B.I. Epureanu, J.B. Siegel, A.G. Stefanopoulou, Phenomenological force and swelling models for rechargeable lithium-ion battery cells, J. Power Sources 310 (2016) 118–129. https://doi.org/10.1016/j.jpowsour.2016.01.103.
- [38] L. Wu, J. Zhang, Three-Dimensional Finite Element Study on Lithium Diffusion and Intercalation-Induced Stress in Polycrystalline LiCoO2 Using Anisotropic Material Properties, J. Electrochem. Energy Convers. Storage 16 (2019). https://doi.org/10.1115/1.4041981.
- [39] X. Wang, Y. Sone, G. Segami, H. Naito, C. Yamada, K. Kibe, Understanding Volume Change in Lithium-Ion Cells during Charging and Discharging Using In Situ Measurements, J. Electrochem. Soc. 154 (2007) A14. https://doi.org/10.1149/1.2386933.
- [40] C. Hendricks, B. Sood, M. Pecht, Lithium-Ion Battery Strain Gauge Monitoring and Depth of Discharge Estimation, J. Electrochem. Energy Convers. Storage 20 (2023) 1–18. https://doi.org/10.1115/1.4054340.
- [41] L.K. Willenberg, P. Dechent, G. Fuchs, D.U. Sauer, E. Figgemeier, High-Precision Monitoring of Volume Change of Commercial Lithium-Ion Batteries by Using Strain Gauges, Sustainability 12 (2020) 557. https://doi.org/10.3390/su12020557.
- [42] L. Willenberg, P. Dechent, G. Fuchs, M. Teuber, M. Eckert, M. Graff, N. Kürten, D.U. Sauer, E. Figgemeier, The Development of Jelly Roll Deformation in 18650 Lithium-Ion Batteries at Low State of Charge, J. Electrochem. Soc. 167 (2020) 120502. https://doi.org/10.1149/1945-7111/aba96d.
- [43] Y. Wu, S. Zhu, Z. Wang, P. Zhou, F. Xie, J. Zhou, H.-S. Chen, W.-L. Song, D. Fang, In-situ investigations of the inhomogeneous strain on the steel case of 18650 silicon/graphite lithium-ion cells, Electrochimica Acta 367 (2021) 137516. https://doi.org/10.1016/j.electacta.2020.137516.
- [44] F.A. Mier, S.M.M. Hill, J. Lamb, M.J. Hargather, Non-invasive internal pressure measurement of 18650 format lithium ion batteries during thermal runaway, J. Energy

- Storage 51 (2022) 104322. https://doi.org/10.1016/j.est.2022.104322.
- [45] R.A. Leising, M.J. Palazzo, E.S. Takeuchi, K.J. Takeuchi, A study of the overcharge reaction of lithium-ion batteries, J. Power Sources 97–98 (2001) 681–683. https://doi.org/10.1016/S0378-7753(01)00598-5.
- [46] J. Chen, C. Buhrmester, J.R. Dahn, Chemical Overcharge and Overdischarge Protection for Lithium-Ion Batteries, Electrochem. Solid-State Lett. 8 (2004) A59. https://doi.org/10.1149/1.1836119.
- [47] T. Ohsaki, T. Kishi, T. Kuboki, N. Takami, N. Shimura, Y. Sato, M. Sekino, A. Satoh, Overcharge reaction of lithium-ion batteries, J. Power Sources 146 (2005) 97–100. https://doi.org/10.1016/j.jpowsour.2005.03.105.
- [48] M. Dubarry, C. Truchot, B.Y. Liaw, Synthesize battery degradation modes via a diagnostic and prognostic model, J. Power Sources 219 (2012) 204–216. https://doi.org/10.1016/j.jpowsour.2012.07.016.
- [49] J. Vetter, P. Novák, M.R. Wagner, C. Veit, K.-C. Möller, J.O. Besenhard, M. Winter, M. Wohlfahrt-Mehrens, C. Vogler, A. Hammouche, Ageing mechanisms in lithium-ion batteries, J. Power Sources 147 (2005) 269–281. https://doi.org/10.1016/j.jpowsour.2005.01.006.
- [50] C. Pastor-Fernández, W. Dhammika Widanage, J. Marco, M.-Á. Gama-Valdez, Gael.H. Chouchelamane, Identification and quantification of ageing mechanisms in Lithium-ion batteries using the EIS technique, in: 2016 IEEE Transp. Electrification Conf. Expo ITEC, 2016: pp. 1–6. https://doi.org/10.1109/ITEC.2016.7520198.
- [51] C. Pastor-Fernández, K. Uddin, G.H. Chouchelamane, W.D. Widanage, J. Marco, A Comparison between Electrochemical Impedance Spectroscopy and Incremental Capacity-Differential Voltage as Li-ion Diagnostic Techniques to Identify and Quantify the Effects of Degradation Modes within Battery Management Systems, J. Power Sources 360 (2017) 301–318. https://doi.org/10.1016/J.JPOWSOUR.2017.03.042.
- [52] J. Liu, Q. Duan, L. Feng, M. Ma, J. Sun, Q. Wang, Capacity fading and thermal stability of LiNixCoyMnzO2/graphite battery after overcharging, J. Energy Storage 29 (2020) 101397. https://doi.org/10.1016/j.est.2020.101397.
- [53] J. Liu, Q. Duan, M. Ma, C. Zhao, J. Sun, Q. Wang, Aging mechanisms and thermal stability of aged commercial 18650 lithium ion battery induced by slight overcharging cycling, J. Power Sources 445 (2020) 227263. https://doi.org/10.1016/j.jpowsour.2019.227263.
- [54] N. Togasaki, T. Yokoshima, Y. Oguma, T. Osaka, Prediction of overcharge-induced serious capacity fading in nickel cobalt aluminum oxide lithium-ion batteries using electrochemical impedance spectroscopy, J. Power Sources 461 (2020) 228168. https://doi.org/10.1016/j.jpowsour.2020.228168.

- [55] M. Abaspour, K.R. Pattipati, B. Shahrrava, B. Balasingam, Robust Approach to Battery Equivalent-Circuit-Model Parameter Extraction Using Electrochemical Impedance Spectroscopy, (2022). https://doi.org/10.3390/en15239251.
- [56] J. Estaller, A. Kersten, M. Kuder, T. Thiringer, R. Eckerle, T. Weyh, Overview of Battery Impedance Modeling Including Detailed State-of-the-Art Cylindrical 18650 Lithium-Ion Battery Cell Comparisons, Energies 15 (2022) 3822. https://doi.org/10.3390/en15103822.
- [57] J. Liu, W. Peng, M. Yang, K. Jin, P. Liu, J. Sun, Q. Wang, Quantitative analysis of aging and detection of commercial 18650 lithium-ion battery under slight overcharging cycling, J. Clean. Prod. 340 (2022) 130756. https://doi.org/10.1016/j.jclepro.2022.130756.
- [58] L. Zhang, L. Huang, Z. Zhang, Z. Wang, D.D. Dorrell, Degradation characteristics investigation for lithium-ion cells with NCA cathode during overcharging, Appl. Energy 327 (2022) 120026. https://doi.org/10.1016/j.apenergy.2022.120026.
- [59] S. Chen, G. Fan, Y. Wang, B. Zhou, S. Ye, Y. Liu, B. Guo, C. Zhu, X. Zhang, The impact of intermittent overcharging on battery capacity and reliability: Electrochemical performance analysis and failure prediction, J. Power Sources 591 (2024) 233800. https://doi.org/10.1016/j.jpowsour.2023.233800.
- [60] I.I. Bezsonov, G.H. Waller, J. Ko, S.P.V. Nadimpalli, In operando measurement of surface strain of 18650 Li-ion cells during cycling, J. Power Sources 592 (2024) 233915. https://doi.org/10.1016/j.jpowsour.2023.233915.
- [61] M. Doyle, T.F. Fuller, J. Newman, Modeling of Galvanostatic Charge and Discharge of the Lithium/Polymer/Insertion Cell, J. Electrochem. Soc. 140 (1993) 1526. https://doi.org/10.1149/1.2221597.
- [62] M. Doyle, J. Newman, The use of mathematical modeling in the design of lithium/polymer battery systems, Electrochimica Acta 40 (1995) 2191–2196. https://doi.org/10.1016/0013-4686(95)00162-8.
- [63] M. Doyle, J. Newman, A.S. Gozdz, C.N. Schmutz, J.-M. Tarascon, Comparison of Modeling Predictions with Experimental Data from Plastic Lithium Ion Cells, J. Electrochem. Soc. 143 (1996) 1890. https://doi.org/10.1149/1.1836921.
- [64] J. Newman, W. Tiedemann, Porous-electrode theory with battery applications, AIChE J. 21 (1975) 25–41. https://doi.org/10.1002/aic.690210103.
- [65] K. West, T. Jacobsen, S. Atlung, Modeling of Porous Insertion Electrodes with Liquid Electrolyte, J. Electrochem. Soc. 129 (1982) 1480–1485. https://doi.org/10.1149/1.2124188.
- [66] J. Newman, Presented at the Electric Power Research Institute Battery Conference, Palo Alto, CA, November 30, 1983, (n.d.).

- [67] J. Lin, H.N. Chu, K. Thu, M. Wojtala, F. Gao, K.J. Chua, Novel battery thermal management via scalable dew-point evaporative cooling, Energy Convers. Manag. 283 (2023) 116948. https://doi.org/10.1016/j.enconman.2023.116948.
- [68] D.J. Pereira, J.W. Weidner, T.R. Garrick, The Effect of Volume Change on the Accessible Capacities of Porous Silicon-Graphite Composite Anodes, J. Electrochem. Soc. 166 (2019) A1251–A1256. https://doi.org/10.1149/2.1211906jes.
- [69] D.J. Pereira, A.M. Aleman, J.W. Weidner, T.R. Garrick, A Mechano-Electrochemical Battery Model that Accounts for Preferential Lithiation Inside Blended Silicon Graphite (Si/C) Anodes, J. Electrochem. Soc. 169 (2022) 020577. https://doi.org/10.1149/1945-7111/ac554f.
- [70] T.R. Garrick, M.A. Fernandez, B.J. Koch, E. Efimoff, M. Jones, R. Mollah, H. Teel, X. Du, S. Shimpalee, S.-Y. Choe, V.R. Subramanian, J.B. Siegel, Modeling Rate Dependent Volume Change in Porous Electrodes in Lithium-Ion Batteries, J. Electrochem. Soc. 171 (2024) 073507. https://doi.org/10.1149/1945-7111/ad6483.
- [71] H.-H. Ryu, K.-J. Park, C.S. Yoon, Y.-K. Sun, Capacity Fading of Ni-Rich Li[NixCoyMn1-x-y]O2 (0.6 $\le x \le 0.95$) Cathodes for High-Energy-Density Lithium-Ion Batteries: Bulk or Surface Degradation?, Chem. Mater. 30 (2018) 1155-1163. https://doi.org/10.1021/acs.chemmater.7b05269.
- [72] V.A. Sethuraman, A. Nguyen, M.J. Chon, S.P.V. Nadimpalli, H. Wang, D.P. Abraham, A.F. Bower, V.B. Shenoy, P.R. Guduru, Stress Evolution in Composite Silicon Electrodes during Lithiation/Delithiation, J. Electrochem. Soc. 160 (2013) A739–A746. https://doi.org/10.1149/2.021306jes.
- [73] A.S. Wineman, K.R. Rajagopal, Mechanical response of polymers: an introduction, Cambridge university press, 2000.
- [74] A. Santimetaneedol, R. Tripuraneni, S.A. Chester, S.P.V. Nadimpalli, Time-dependent deformation behavior of polyvinylidene fluoride binder: Implications on the mechanics of composite electrodes, J. Power Sources 332 (2016) 118–128. https://doi.org/10.1016/j.jpowsour.2016.09.102.
- [75] M. Pharr, Z. Suo, J.J. Vlassak, Variation of stress with charging rate due to strain-rate sensitivity of silicon electrodes of Li-ion batteries, (2014). https://doi.org/10.1016/j.jpowsour.2014.07.153.
- [76] V.A. Sethuraman, V. Srinivasan, A.F. Bower, P.R. Guduru, In Situ Measurements of Stress-Potential Coupling in Lithiated Silicon, J. Electrochem. Soc. 157 (2010) A1253. https://doi.org/10.1149/1.3489378.

- [77] S. Schweidler, L. de Biasi, A. Schiele, P. Hartmann, T. Brezesinski, J. Janek, Volume Changes of Graphite Anodes Revisited: A Combined Operando X-ray Diffraction and In Situ Pressure Analysis Study, J. Phys. Chem. C 122 (2018) 8829–8835. https://doi.org/10.1021/acs.jpcc.8b01873.
- [78] L.Y. Beaulieu, T.D. Hatchard, A. Bonakdarpour, M.D. Fleischauer, J.R. Dahn, Reaction of Li with Alloy Thin Films Studied by In Situ AFM, J. Electrochem. Soc. 150 (2003) A1457. https://doi.org/10.1149/1.1613668.
- [79] S. Zheng, C. Hong, X. Guan, Y. Xiang, X. Liu, G.-L. Xu, R. Liu, G. Zhong, F. Zheng, Y. Li, X. Zhang, Y. Ren, Z. Chen, K. Amine, Y. Yang, Correlation between long range and local structural changes in Ni-rich layered materials during charge and discharge process, J. Power Sources 412 (2019) 336–343. https://doi.org/10.1016/j.jpowsour.2018.11.053.
- [80] W. Li, J.N. Reimers, J.R. Dahn, In situ x-ray diffraction and electrochemical studies of Li1-xNiO2, Solid State Ion. 67 (1993) 123–130. https://doi.org/10.1016/0167-2738(93)90317-V.
- [81] R. Jung, M. Metzger, F. Maglia, C. Stinner, H.A. Gasteiger, Oxygen Release and Its Effect on the Cycling Stability of LiNi x Mn y Co z O 2 (NMC) Cathode Materials for Li-Ion Batteries, J. Electrochem. Soc. 164 (2017) A1361–A1377. https://doi.org/10.1149/2.0021707jes.
- [82] H.-J. Noh, S. Youn, C.S. Yoon, Y.-K. Sun, Comparison of the structural and electrochemical properties of layered Li[NixCoyMnz]O2 (x = 1/3, 0.5, 0.6, 0.7, 0.8 and 0.85) cathode material for lithium-ion batteries, J. Power Sources 233 (2013) 121–130. https://doi.org/10.1016/j.jpowsour.2013.01.063.
- [83] H. Li, M. Cormier, N. Zhang, J. Inglis, J. Li, J.R. Dahn, Is Cobalt Needed in Ni-Rich Positive Electrode Materials for Lithium Ion Batteries?, J. Electrochem. Soc. 166 (2019) A429. https://doi.org/10.1149/2.1381902jes.
- [84] H.-H. Ryu, N.-Y. Park, J.H. Seo, Y.-S. Yu, M. Sharma, R. Mücke, P. Kaghazchi, C.S. Yoon, Y.-K. Sun, A highly stabilized Ni-rich NCA cathode for high-energy lithium-ion batteries, Mater. Today 36 (2020) 73–82. https://doi.org/10.1016/j.mattod.2020.01.019.
- [85] L. Noerochim, S. Suwarno, N.H. Idris, H.K. Dipojono, Recent Development of Nickel-Rich and Cobalt-Free Cathode Materials for Lithium-Ion Batteries, Batteries 7 (2021) 84. https://doi.org/10.3390/batteries7040084.
- [86] N. Hamzelui, G.G. Eshetu, E. Figgemeier, Customizing Active Materials and Polymeric Binders: Stern Requirements to Realize Silicon-Graphite Anode Based Lithium-Ion Batteries., J. Energy Storage 35 (2021) 102098. https://doi.org/10.1016/j.est.2020.102098.
- [87] Z. Wang, J. Yuan, X. Zhu, H. Wang, L. Huang, Y. Wang, S. Xu, Overcharge-to-thermal-

- runaway behavior and safety assessment of commercial lithium-ion cells with different cathode materials: A comparison study, J. Energy Chem. 55 (2021) 484–498. https://doi.org/10.1016/j.jechem.2020.07.028.
- [88] W. Li, K.R. Crompton, C. Hacker, J.K. Ostanek, Comparison of Current Interrupt Device and Vent Design for 18650 Format Lithium-ion Battery Caps, J. Energy Storage 32 (2020) 101890. https://doi.org/10.1016/j.est.2020.101890.
- [89] Y. Liu, L. Qin, Y. Wu, X. Wu, W. Jin, Thermal runaway-induced current interrupt device and vent activation behaviour in an 18650 lithium-ion battery cap using the Johnson-Cook criterion, J. Energy Storage 68 (2023) 107879. https://doi.org/10.1016/j.est.2023.107879.
- [90] Inc. Measurements Group, Errors Due to Transverse Sensitivity in Strain Gages, Exp. Tech. 7 (1983) 30–35. https://doi.org/10.1111/j.1747-1567.1983.tb01667.x.
- [91] J. Hemmerling, J. Schäfer, T. Jung, T. Kreher, M. Ströbel, C. Gassmann, J. Günther, A. Fill, K.P. Birke, Investigation of internal gas pressure and internal temperature of cylindrical Li-ion cells to study thermodynamical and mechanical properties of hard case battery cells, J. Energy Storage 59 (2023) 106444. https://doi.org/10.1016/j.est.2022.106444.
- [92] H. Oka, T. Nonaka, Y. Kondo, Y. Makimura, Quantification of side reactions in lithium-ion batteries during overcharging at elevated temperatures, J. Power Sources 580 (2023) 233387. https://doi.org/10.1016/j.jpowsour.2023.233387.
- [93] S. Schweidler, L. de Biasi, A. Schiele, P. Hartmann, T. Brezesinski, J. Janek, Volume Changes of Graphite Anodes Revisited: A Combined Operando X-ray Diffraction and In Situ Pressure Analysis Study, J. Phys. Chem. C 122 (2018) 8829–8835. https://doi.org/10.1021/acs.jpcc.8b01873.
- [94] T. Mori, K. Tanaka, Average stress in matrix and average elastic energy of materials with misfitting inclusions, Acta Metall. 21 (1973) 571–574. https://doi.org/10.1016/0001-6160(73)90064-3.
- [95] A. Jokar, B. Rajabloo, M. Désilets, M. Lacroix, Review of simplified Pseudo-two-Dimensional models of lithium-ion batteries, J. Power Sources 327 (2016) 44–55. https://doi.org/10.1016/j.jpowsour.2016.07.036.
- [96] J. Eshelby, The determination of the elastic field of an ellipsoidal inclusion, and related problems | Proceedings of the Royal Society of London. Series A. Mathematical and Physical Sciences, in: Proc. R. Soc. Lond., 1957: pp. 376–396. https://doi.org/10.1098/rspa.1957.0133.
- [97] M.H. Sadd, Elasticity: Theory, Applications, and Numerics, Academic Press, 2009.
- [98] G.M. Jenkins, The effect of microporosity on the elastic modulus and yield curve of polycrystalline graphite, J. Nucl. Mater. 29 (1969) 322–328.

- https://doi.org/10.1016/0022-3115(69)90209-8.
- [99] S.P.V. Nadimpalli, V.A. Sethuraman, G. Bucci, V. Srinivasan, A.F. Bower, P.R. Guduru, On Plastic Deformation and Fracture in Si Films during Electrochemical Lithiation/Delithiation Cycling, J. Electrochem. Soc. 160 (2013) A1885–A1893. https://doi.org/10.1149/2.098310jes.
- [100] M.E. Spahr, D. Goers, A. Leone, S. Stallone, E. Grivei, Development of carbon conductive additives for advanced lithium ion batteries, J. Power Sources 196 (2011) 3404–3413. https://doi.org/10.1016/j.jpowsour.2010.07.002.
- [101] Y. Lu, Y. Zhang, Q. Zhang, F. Cheng, J. Chen, Recent advances in Ni-rich layered oxide particle materials for lithium-ion batteries, Particuology 53 (2020) 1–11. https://doi.org/10.1016/j.partic.2020.09.004.
- [102] K.-J. Park, H.-G. Jung, L.-Y. Kuo, P. Kaghazchi, C.S. Yoon, Y.-K. Sun, Improved Cycling Stability of Li[Ni0.90Co0.05Mn0.05]O2 Through Microstructure Modification by Boron Doping for Li-lon Batteries, Adv. Energy Mater. 8 (2018) 1801202. https://doi.org/10.1002/aenm.201801202.
- [103] Y. Qi, H. Guo, L.G. Hector, A. Timmons, Threefold Increase in the Young's Modulus of Graphite Negative Electrode during Lithium Intercalation, J. Electrochem. Soc. 157 (2010) A558. https://doi.org/10.1149/1.3327913.
- [104] V.A. Sethuraman, M.J. Chon, M. Shimshak, N.V. Winkle, P.R. Guduru, In situ measurement of biaxial modulus of Si anode for Li-ion batteries, Electrochem. Commun. 12 (2010) 1614–1617. https://doi.org/10.1016/j.elecom.2010.09.008.
- [105] G. Sikha, B.N. Popov, R.E. White, Effect of Porosity on the Capacity Fade of a Lithium-Ion Battery: Theory, J. Electrochem. Soc. 151 (2004) A1104. https://doi.org/10.1149/1.1759972.
- [106] Y. Qi, S.J. Harris, In Situ Observation of Strains during Lithiation of a Graphite Electrode, J. Electrochem. Soc. 157 (2010) A741. https://doi.org/10.1149/1.3377130.
- [107] C.P. Aiken, N. Kowalski, R.C. Fitzner, S. Trussler, J.E. Harlow, E.J. Butler, J.R. Dahn, Tracking Electrolyte Motion in Cylindrical Li-ion Cells Using Moment of Inertia Measurements, J. Electrochem. Soc. 170 (2023) 040529. https://doi.org/10.1149/1945-7111/acce72.
- [108] L.B. Freund, S. Suresh, Thin Film Materials: Stress, Defect Formation and Surface Evolution, Cambridge University Press, 2004.
- [109] Y. Pei, X.C. Zeng, Elastic properties of poly(vinyldene fluoride) (PVDF) crystals: A density functional theory study, J. Appl. Phys. 109 (2011) 093514. https://doi.org/10.1063/1.3574653.

- [110] E.J. Cheng, K. Hong, N.J. Taylor, H. Choe, J. Wolfenstine, J. Sakamoto, Mechanical and physical properties of LiNi0.33Mn0.33Co0.33O2 (NMC), J. Eur. Ceram. Soc. 37 (2017) 3213–3217. https://doi.org/10.1016/j.jeurceramsoc.2017.03.048.
- [111] L. Xiao, Mechanical properties modeling of cathode materials for lithium-ion batteries based on bond valence model, Mater. Today Commun. 39 (2024) 108852. https://doi.org/10.1016/j.mtcomm.2024.108852.
- [112] L. Wang, S. Yin, C. Zhang, Y. Huan, J. Xu, Mechanical characterization and modeling for anodes and cathodes in lithium-ion batteries, J. Power Sources 392 (2018) 265–273. https://doi.org/10.1016/j.jpowsour.2018.05.007.
- [113] R. Robert, C. Bünzli, E.J. Berg, P. Novák, Activation Mechanism of LiNi0.80Co0.15Al0.05O2: Surface and Bulk Operando Electrochemical, Differential Electrochemical Mass Spectrometry, and X-ray Diffraction Analyses, Chem. Mater. 27 (2015) 526–536. https://doi.org/10.1021/cm503833b.
- [114] N. Iqbal, J. Choi, C. Lee, H.M.U. Ayub, J. Kim, M. Kim, Y. Kim, D. Moon, S. Lee, Effects of Diffusion-Induced Nonlinear Local Volume Change on the Structural Stability of NMC Cathode Materials of Lithium-Ion Batteries, Mathematics 10 (2022) 4697. https://doi.org/10.3390/math10244697.
- [115] V.A. Sethuraman, M.J. Chon, M. Shimshak, V. Srinivasan, P.R. Guduru, In situ measurements of stress evolution in silicon thin films during electrochemical lithiation and delithiation, J. Power Sources 195 (2010) 5062–5066. https://doi.org/10.1016/j.jpowsour.2010.02.013.
- [116] F. Yang, Interaction between diffusion and chemical stresses, Mater. Sci. Eng. A 409 (2005) 153–159. https://doi.org/10.1016/j.msea.2005.05.117.
- [117] X. Zhang, W. Shyy, A.M. Sastry, Numerical Simulation of Intercalation-Induced Stress in Lilon Battery Electrode Particles, J. Electrochem. Soc. 154 (2007) A910. https://doi.org/10.1149/1.2759840.
- [118] K.-Y. Oh, B.I. Epureanu, Characterization and modeling of the thermal mechanics of lithium-ion battery cells, Appl. Energy 178 (2016) 633–646. https://doi.org/10.1016/j.apenergy.2016.06.069.
- [119] X. Wen, Q. Zeng, J. Guan, W. Wen, P. Chen, Z. Li, Y. Liu, A. Chen, X. Liu, W. Liu, S. Chen, L. Zhang, 3D structural lithium alginate-based gel polymer electrolytes with superior high-rate long cycling performance for high-energy lithium metal batteries, J. Mater. Chem. A 10 (2022) 707–718. https://doi.org/10.1039/D1TA07252H.
- [120] X.H. Liu, L. Zhong, S. Huang, S.X. Mao, T. Zhu, J.Y. Huang, Size-Dependent Fracture of Silicon Nanoparticles During Lithiation, ACS Nano 6 (2012) 1522–1531. https://doi.org/10.1021/nn204476h.

- [121] F.A. Mier, S.M.M. Hill, J. Lamb, M.J. Hargather, Non-invasive internal pressure measurement of 18650 format lithium ion batteries during thermal runaway, J. Energy Storage 51 (2022) 104322. https://doi.org/10.1016/j.est.2022.104322.
- [122] Tesla's 250-kW Supercharger Only Saved Us 2 Minutes vs. a 150-kW Charger, Car Driv. (2020). https://www.caranddriver.com/news/a32132062/tesla-250-kw-vs-150-kw-supercharger-tested/ (accessed August 12, 2024).
- [123] L.A. Berla, S.W. Lee, Y. Cui, W.D. Nix, Mechanical behavior of electrochemically lithiated silicon, J. Power Sources 273 (2015) 41–51. https://doi.org/10.1016/j.jpowsour.2014.09.073.
- [124] R. Tripuraneni, S. Rakshit, S.P.V. Nadimpalli, In Situ Measurement of the Effect of Stress on the Chemical Diffusion Coefficient of Li in High-Energy-Density Electrodes, J. Electrochem. Soc. 165 (2018) A2194—A2202. https://doi.org/10.1149/2.0641810jes.
- [125] T. Wu, İ. Temizer, P. Wriggers, Computational thermal homogenization of concrete, Cem. Concr. Compos. 35 (2013) 59–70. https://doi.org/10.1016/j.cemconcomp.2012.08.026.
- [126] H. Shin, S. Yang, S. Chang, S. Yu, M. Cho, Multiscale homogenization modeling for thermal transport properties of polymer nanocomposites with Kapitza thermal resistance, Polymer 54 (2013) 1543–1554. https://doi.org/10.1016/j.polymer.2013.01.020.
- [127] M.M. Loghavi, A. Nahvibayani, M.H. Moghim, M. Babaiee, S. Baktashian, R. Eqra, Electrochemical evaluation of LiNi0.5Mn0.3Co0.2O2, LiNi0.6Mn0.2Co0.2O2, and LiNi0.8Mn0.1Co0.1O2 cathode materials for lithium-ion batteries: from half-coin cell to pouch cell, Monatshefte Für Chem. Chem. Mon. 153 (2022) 1197–1212. https://doi.org/10.1007/s00706-022-02995-9.

APPENDIX A: ELECTRODE STRESS MEASUREMENTS

A.1: Experimental Setup for Electrode Stress Measurements

The stress in the anode and cathode during lithiation and delithiation was measured using a substrate curvature method. The samples were prepared by bonding electrode sheets (composite active material coating on a metal current collector, purchased from NEI Corp.) to a reflective substrate using a Loctite Stycast two-part epoxy. The schematic of a stress measurement sample is shown in Figure 48 below.

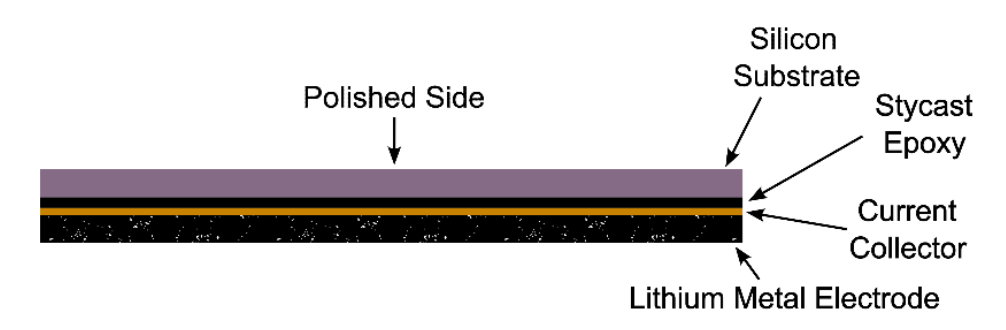


Figure 48: Electrode stress measurement sample.

Some electrode material was harvested from 18650 cells but yielded limited success due to delamination issues from the current collector – specifically for the anode. For this reason, fresh electrodes representative of cell chemistry were ordered from NEI Corp. for the experiments. The substrates chosen were single side polished silicon wafers, two inches in diameter and grown in the <111> orientation, coated with 5,000Å of wet thermal oxide (SiO₂). The polished side was used for the curvature measurements, while the non-polished side provided a high surface area for epoxy bonding. The <111> orientation wafers were specifically chosen due to the isotropic bending of the wafer, as wafers grown in the <100> and <110> crystal orientations experience different bending in the X and Y directions. The oxide coating on the silicon was necessary to prevent lithiation of the substrate.

The Stycast epoxy was chosen because it is known to be chemically resistant to the solvents used in lithium-ion battery electrolyte. The epoxy was applied to the non-polished side of the wafer using a spin-coater to achieve a uniform thickness across the wafer's surface. The wafer with the epoxy was subjected to a vacuum to eliminate the bubbles due to mixing of the epoxy, after which the wafer was placed on the current collector side of the electrode. Weight (5

lb.) was placed on top of the wafer, and the epoxy was given at least 24 hours to cure at room temperature. The excess current collector and cathode coating was cut around the silicon wafer, leaving a current collector to allow electrical connection to the potentiostat. A fully prepared specimen (with the electrode coating facing up) is shown in Figure 49a below. A photo was taken of each sample to determine the exact area using ImageJ software, which was multiplied by the areal loading of the electrodes to determine the sample's capacity. The layers of the specimen are shown in Figure 49b. The parameters *M* and *h* are the bi-axial moduli and thicknesses of the materials, respectively, which are used for the stress calculations.

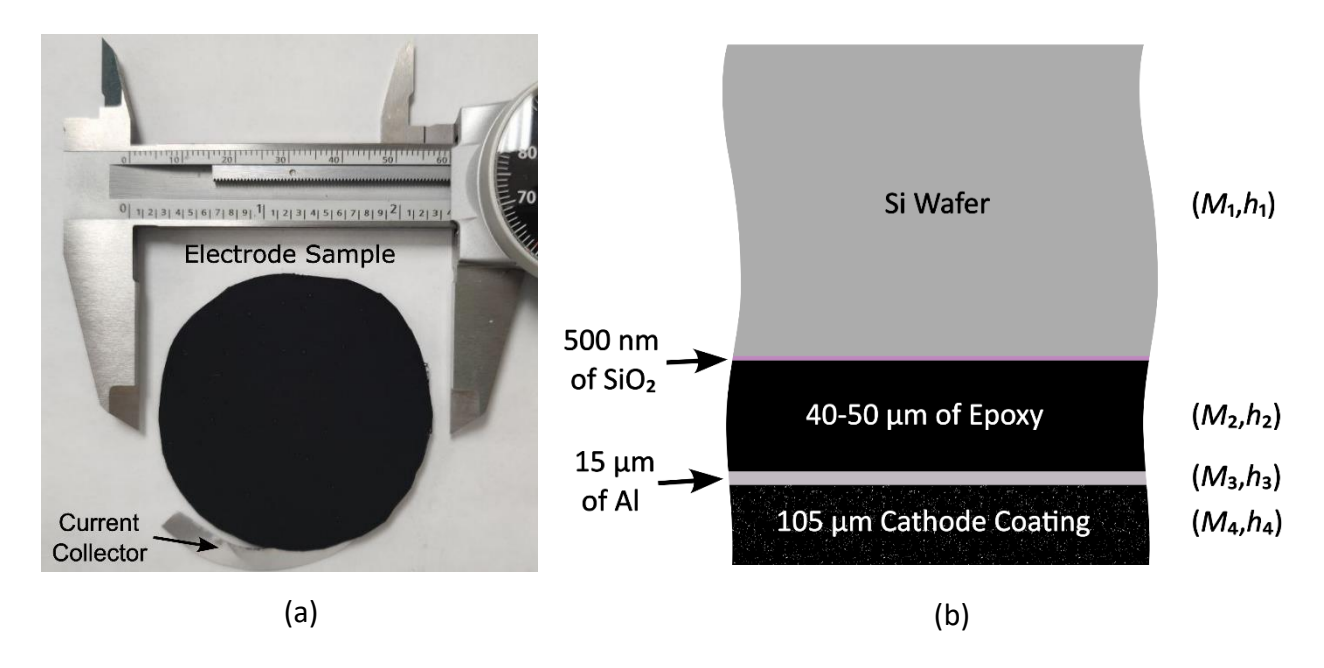


Figure 49: (a) Prepared cathode specimen with a current collector for electrical connection. (b) Schematic of the cathode specimen layers.

The electrode sample was then vacuum baked at 80°C for a minimum of 24 hours (to ensure it was completely dry) and assembled into an electrochemical half-cell versus a lithium metal electrode inside an argon-filled glovebox. The container used, named "beaker cell" due to its cylindrical open-top shape, was made of Teflon due to its chemical resistance. The design for the beaker cell is shown by the CAD model in Figure 50 below. The lid was machined from stainless steel, and the glass window was bonded to it using Loctite Stycast epoxy. A rubber gasket was placed between the Teflon base and the stainless steel lid. Six bolts and nuts were used to achieve an air-tight seal to prevent electrolyte evaporation during the experiment.

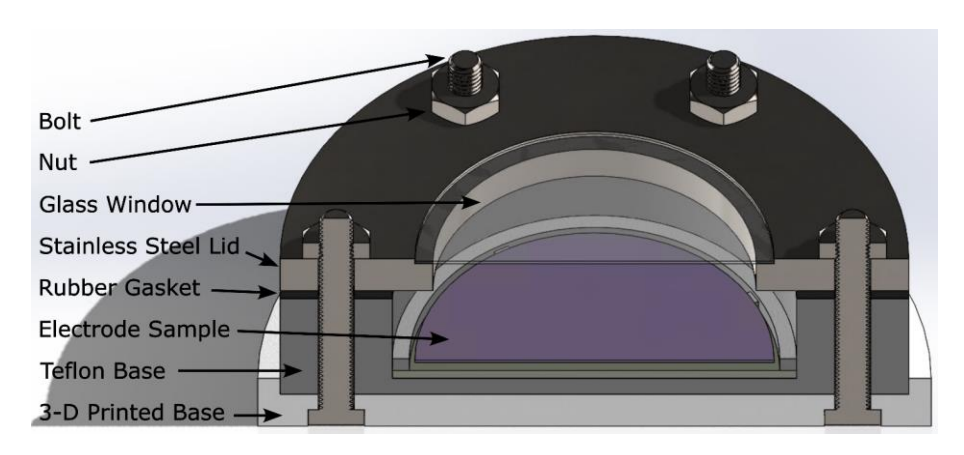


Figure 50: Beaker cell CAD model with cutaway.

A piece of lithium foil was cut into a circular shape, slightly larger than the electrode sample in diameter. A copper wire was then embedded into the lithium electrode, with the contact resistance between the electrode and the wire and electrode being less than 1Ω , as measured by a multimeter. The lithium metal electrode was placed on the bottom of the Teflon beaker cell, followed by a Celgard separator cut to the diameter of the beaker cell. The separators were prepared ahead of time and soaked in lithium-ion electrolyte ($1M \ LiPF_6$ of dissolved in equal parts EC:DC:DMC, purchased from Sigma Aldrich) to minimize the presence of gas bubbles during cell assembly. More electrolyte was then added to the top, to completely soak the separator and the lithium metal electrode below. Finally, the electrode sample was placed, active material-side down, onto the separator. More electrolyte was carefully added to the cell, avoiding the reflective top of the substrate, to ensure that there was adequate ionic conductivity.

The prepared cell was then moved to a stage with adjustable roll, pitch, and yaw for the curvature measurements. The tool utilized for these measurements was the kSA Multibeam Optical Sensor, or MOS. This tool is primarily used to determine the stress in a thin film deposited onto a substrate during sputtering or evaporation deposition by measuring the substrate's curvature before and after deposition. The equation used to determine the stress state based on the substrate's curvature is the Stoney Equation, as shown below in Equation 71. This version was modified to account for the current collector and epoxy between the film and the substrate.

$$\sigma=\frac{M_1h_1^2\kappa}{6h_4f(h_i,M_i)}; \qquad \qquad \kappa=\frac{\cos\varphi}{2L}\Big\{\frac{D_0-D}{D_0}\Big\}$$
 Equation 71

The stress within the coating is represented by σ . The bi-axial modulus and thickness of the silicon wafer are M_1 and h_1 , respectively. The curvature of the substrate, κ , is calculated using the initial laser spot spacing, D_0 , and the instantaneous spot spacing D, which changes during the experiment. The thickness of the composite electrode coating is denoted by h_4 , and $f(h_i, M_i)$ is a function of the thicknesses and moduli of all layers [30].

The schematic for curvature measurements is shown in Figure 51 below, where an array of lasers reflects from the polished side of the substrate and are captured as spots. The vertical and horizontal distances between the pots are measured to calculate the curvature in the x and y directions. The $\cos\phi/2L$ term in Equation 71, sometimes denoted as A_m , is a mirror constant which represents the optical path of the lasers. This quantity is determined internally by the MOS during a calibration procedure.

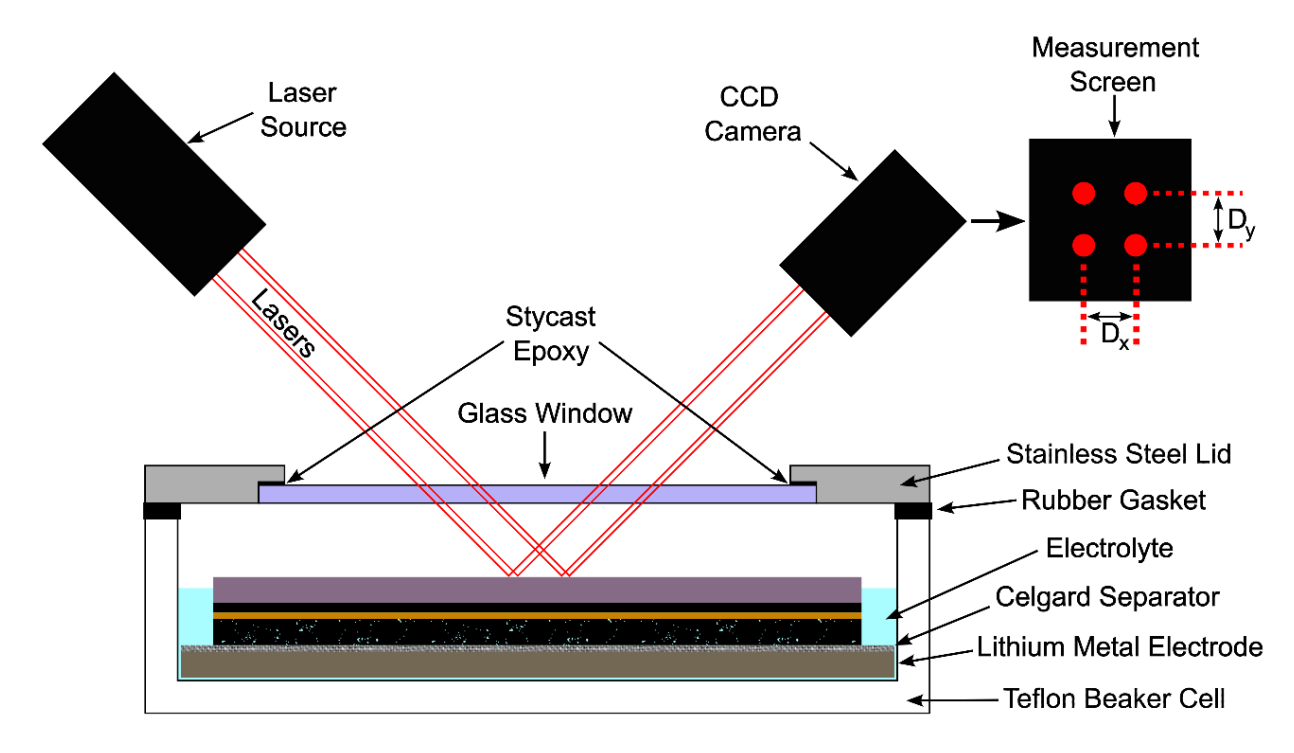


Figure 51: Curvature measurement schematic with laser dot spacing.

Once assembled, a reference measurement was taken of the sample setting the initial spacings in the x and y directions to zero. Then the cell was given 12 hours at OCP for the electrolyte to permeate the electrode and all components, initial SEI to form on the active material, and the cell potential to equilibrate. The cells were then lithiated and delithiated at a C/10 rate, as determined by the capacities calculated earlier for a total number of 3 cycles. MATLAB code was written to process the output of the MOS – that is, the D_x and D_y spacings during the experiment. Most of the material properties used to calculate stress in the film are already known for the components used in these samples [31]. The thicknesses of the layers were measured – either with the use of a micrometer or a scanning electron microscope (SEM). The moduli of the anode and cathode coatings were verified using a KLA micro indenter. The values used for stress calculations are written in Table 14 below.

Parameter	Definition	Value	Comments
Si (111) Wafer			
E ₁	Young's Modulus	169 GPa	
V_1	Poisson's Ratio	0.26	
h_1	Thickness	315 μm	Measured
M_1	Biaxial Modulus	228.3 GPa	Calculated
Epoxy Layer			
E ₂	Young's Modulus	4.3 GPa	[30]
V ₂	Poisson's Ratio	0.36	[30]
h_2	Thickness	45 μm	Measured
M ₂	Biaxial Modulus	6.72 GPa	Calculated
Al Current Collecto	or		
E3	Young's Modulus	70 GPa	
<i>V</i> 3	Poisson's Ratio	0.334	
h ₃	Thickness	15 μm	Measured
M ₃	Biaxial Modulus	105 GPa	Calculated
Composite Cathod	le Coating		
E4	Young's Modulus	40 GPa	[31]
V4	Poisson's Ratio	0.2	[31]
h_4	Thickness	105 μm	Measured
M ₄	Biaxial Modulus	50 GPa	Calculated
Cu Current Collect	or		
E ₃	Young's Modulus	117 GPa	
<i>V</i> ₃	Poisson's Ratio	0.347	
h ₃	Thickness	10 μm	Measured
<i>M</i> ₃	Biaxial Modulus	179 GPa	Calculated
Composite Anode	Coating		
E4	Young's Modulus	6.36 GPa	[30]
V ₄	Poisson's Ratio	0.2086	[30]
h ₄	Thickness	160 μm	Measured
M ₄	Biaxial Modulus	8.04 GPa	Calculated
Other Parameters			
cosφ/2L	Mirror constant	1.55	Measured
d_f	Diameter of specimen	50.8 mm	Measured

Table 14: Material properties and thicknesses of battery electrode samples.

A.2: Experimentally Measures Stress in Electrodes

The experiments to capture repeatable stress behavior of the individual electrodes have proved to be challenging. While a complete set of repeatable data (from at least 3 electrode samples) could not be obtained, preliminary data was collected. As mentioned previously, electrodes harvested from a fresh 18650 cell experienced significant mechanical degradation, even during the first cycle. Commercial electrodes from MTI and NEI Corp were obtained and tested instead.

A.2.1: Anode Stress Response

The most prominent issue is the delamination of the anode active material from the current collector during specimen fabrication. Anode sheets purchased from NEI and MTI are able to survive the handling during epoxy bonding and half-cell assembly, but do not provide consistent stress results. Inspection of the NEI samples after three CC-CV cycles at a C/10 rate shows delamination of the active material. Another issue is the high curvature of the substrates during the experiments, which causes the laser dots to go out of range – stopping the data measurement. The spot spacing and stress calculated using the parameters in Table 14 are shown in Figure 52a and Figure 52b, respectively. The linear slope between 6 and 18 hours is due to the laser spots leaving the camera range, with no spacing data being recorded during that period. During the rest of the experiment the minimum stress value does not settle on a particular magnitude. Inspection of these samples showed delaminated active material and dried out beaker cells, which is consistent with the changing electrode behavior.

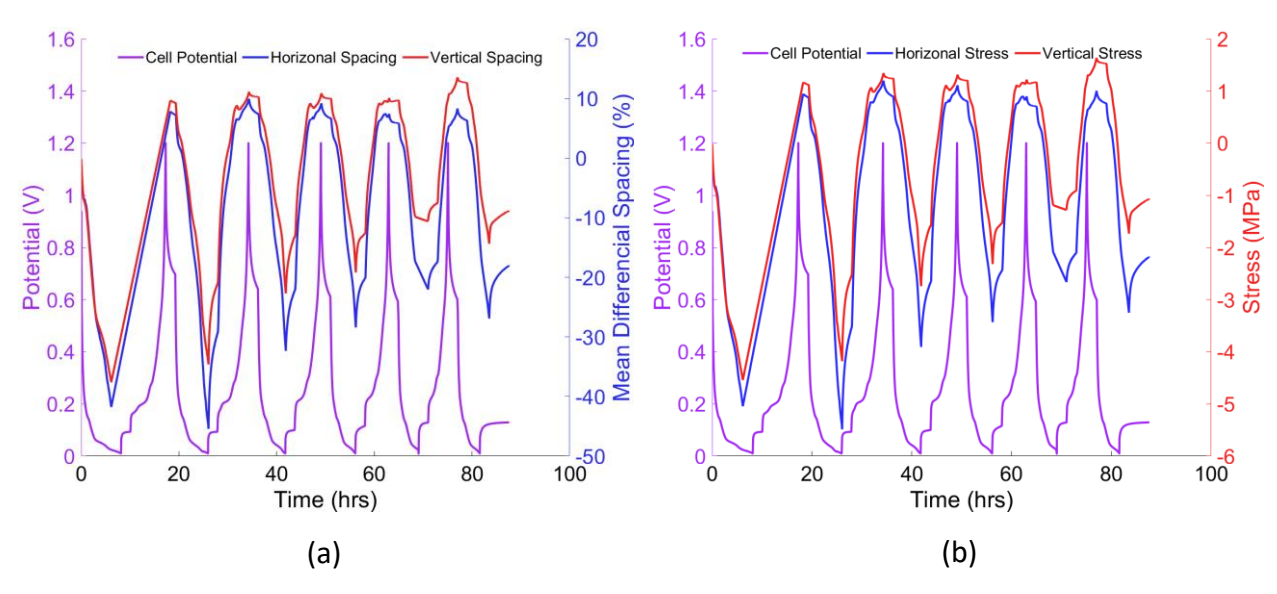


Figure 52: (a) Spot spacing and potential vs. time and (b) calculated stress and potential vs. time for graphite-silicon anodes from NEI.

The electrodes from MTI have so far provided the best results, as shown in Figure 53. The data collected is from a single cycle, but the curvature/stress values reached a similar minimum value both times. The stress values reported previously for an anode were in the range of -10 to 4 MPa, which is close to the data collected from the MTI electrodes. There are key differences between these electrodes and those used in the 18650 cells studied (and ordered from NEI). The 16850 cells have anodes which are double the thickness of the MTI ones, contain 5 wt.% silicon, and use CMC/SBR binder compared to the PVdF in the MTI electrodes. The higher thickness and silicon content should generate a higher curvature — and therefore, higher stress — in the 18650/NEI electrode samples, but the opposite is seen in Figure 53.

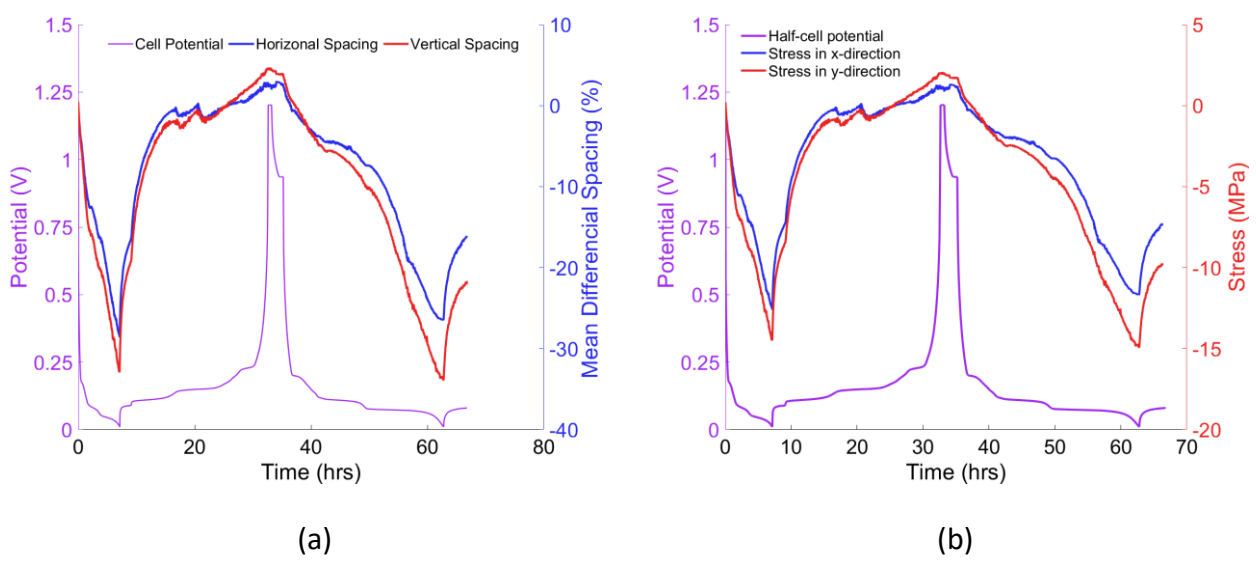


Figure 53: (a) Spot spacing and potential vs. time and (b) calculated stress and potential vs. time for graphite-silicon (5 wt.%) anodes from NEI.

The stress measurements were repeated with a thinner composite anode which measured 60 μ m in thickness. The active material did not delaminate from the current collector, but another issue surfaced. It was discovered that the solvents in the electrolyte degraded the epoxy used to bind the current collector to the silicon wafer. Careful experiments were run to expose only the composite coating to the electrolyte, and two samples yielded repeatable stress data. Since the data set is small, only preliminary conclusions can be drawn.

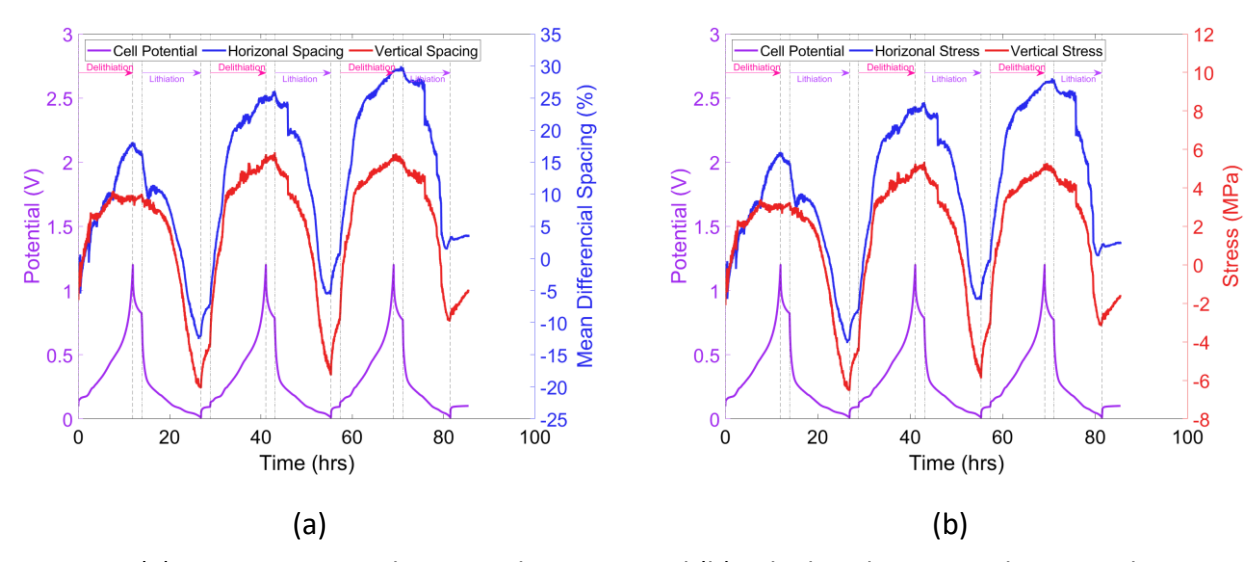


Figure 54: (a) Spot spacing and potential vs. time and (b) calculated stress and potential vs. time for graphite-silicon (20 wt.%) anodes from MTI.

A.2.2: Cathode Stress Response

Most of the cathode material harvested from the 18650 cells was used in the optimization of the stress measurement setup. Fresh NMC811 cathode sheets were ordered from NEI, which were used for the stress measurements. The cathode samples got "stuck" as certain potentials during galvanostatic cycling, so a CV was performed to collect the stress data instead. As shown in Figure 55, the behavior of the cathode is fairly consistent, reaching a peak compressive stress of -6 MPa. This range is similar to electrodes which use Li_{1.2}Ni_{0.15}Mn_{0.55}CO_{0.1}O₂, as reported by Nadimpalli et. al. [31]. It should be noted that the NMC811 cathode sheets were ordered due to an error in the early characterization of the electrode material. The active material was characterized correctly as NCA during the summer of 2023 using EDS analysis. Various studies [4,5,127] have reported similar dQ/dV peaks for NMC811/graphite cells to those derived during baseline cycling. This is due to nickel being the primary component which interacts with lithium in both NMC811 and NCA. Stress measurements were attempted for NCA cathode, but no consistent data could be collected. The best results obtained from an NCA sample are shown in Figure 56.

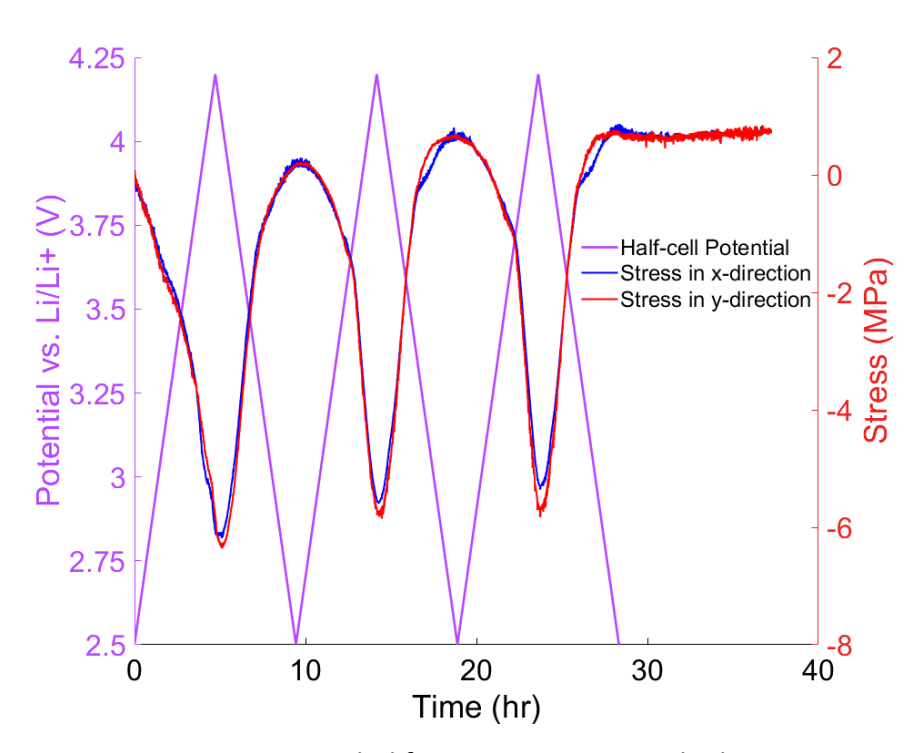


Figure 55: Stress recorded for an NMC811 sample during a CV.

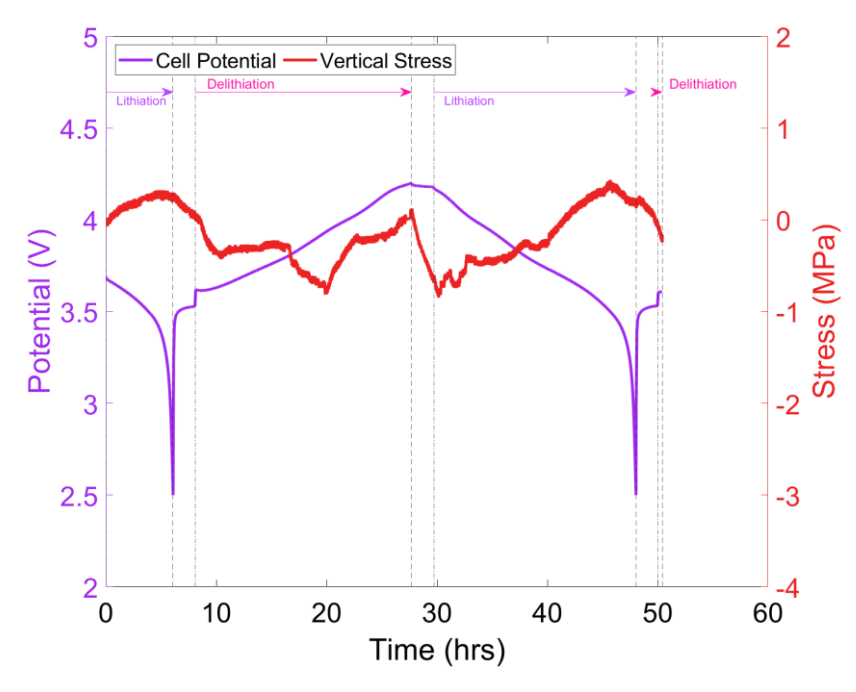


Figure 56: Stress recorded for an NCA sample during galvanostatic cycling.

APPENDIX B: ANALYTICAL MODELING EFFORTS

B.1: Analytical Model from Nadimpalli et al. [31]

Based on the CT analysis, the cell can be modeled as a steel cylinder with concentric rings representing the jelly roll structure. This theoretical approximation is shown in Figure 57 below, where a set of rings consists of 8 layers, which repeat across the jellyroll structure. There inside of the cell contains a hollow space 3.2 mm in diameter, as measured from the CT scan. The outer diameter of 9.1 mm extends from the center of the cell to the inside of the steel cell casing. The thicknesses of the current collectors and composite electrodes were measured from electrodes harvested from a fresh 18650 cell. In this analytic approach the effects of temperature and changes in internal cell pressure due to electrode expansion are currently neglected. The main consideration here is that the volumetric changes in the jelly roll – which act like an internal pressure – are responsible for the stress in the cell casing.

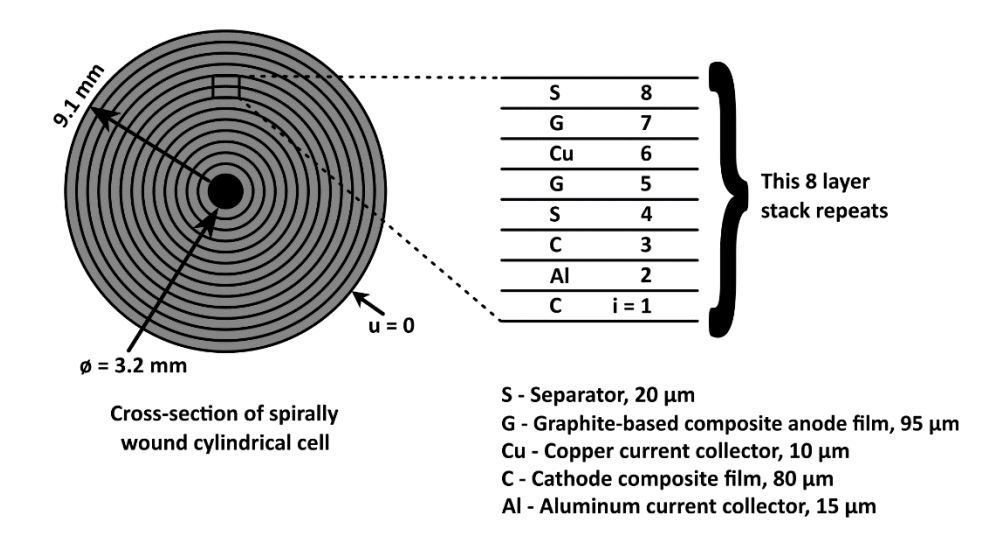


Figure 57: Schematic showing internal layers of a hollow 18650 cell, with electrodes approximated as concentric rings.

To solve for the stress on the surface of the cell casing, the stress on the inside surface must first be calculated. The volumetric changes of the electrodes due to lithium concentration are similar to those due to temperature. Hence, the equations for the displacement and stress due to thermal apply here. The displacement u and stress in the radial direction σ_r are calculated using the axisymmetric temperature distribution in a long cylinder with the plane strain

approximation, as shown using Equation 72 and Equation 73 below.

$$u = \frac{1+\nu}{1-\nu} \alpha \frac{1}{r} \int_{r_i}^{r} T(r) r dr + C_1 r + \frac{C_2}{r}$$

Equation 72

$$\sigma_r = -\frac{\alpha E}{1 - \nu} \frac{1}{r^2} \int_{r_i}^{r} T(r) r dr + \frac{E}{1 + \nu} \left(\frac{C_1}{1 - 2\nu} - \frac{C_2}{r} \right)$$

Equation 73

Young's modulus, Poisson's ratio, and the coefficient of thermal expansion are given by E, v, and α . The radial temperature distribution is given by T(r), and C_1 and C_2 are constants based on boundary conditions on the inner and outer surfaces of the cylinder. The inner radius of the jelly roll is denoted by r_i . The equations for thermally induced displacement and stress can be converted to those induced by lithium concentration in the forms below.

$$u = \frac{1+\nu}{1-\nu} \frac{\varepsilon^*}{r} \int_{r}^{r} r dr + C_1 r + \frac{C_2}{r}$$

Equation 74

$$\sigma_r = -\frac{E}{1-\nu} \frac{\varepsilon^*}{r^2} \int_{r}^{r} r \, dr + \frac{E}{1+\nu} \left(\frac{C_1}{1-2\nu} - \frac{C_2}{r} \right)$$

Equation 75

Here the thermal strain α T(r) is replaced by ε^* , which represents the eigenstrain due to uniform lithium concentration in the electrode. An assumption is made here that the lithium concentration is uniform throughout the entire thickness of one electrode layer. The eigenstrain ε^* in an electrode at a given capacity is calculated using Equation 76 below.

$$\varepsilon^* = \frac{\sigma(1-\nu)}{E}$$

Equation 76

The stress measured in the electrode coatings during galvanostatic lithiation and delithiation using the MOS are denoted by σ . The Young's modulus and Poisson's ratio of the coatings are represented by E and v. It is important to note that Equation 73 is only valid for linear elastic material behavior. Also, the mechanical properties of the electrodes are given as constants, signifying that they are assumed to be isotropic and independent of the lithium concentration (i.e., state of charge) within the electrodes. While, realistically speaking, this may not be the case, these approximations are accurate enough for an initial model.

The boundary conditions for the presented model are $\sigma_r=0$ at $r=r_i$ and u=0 at $r=r_0$. That is, the strain in the radial direction is zero at the hollow center of the cell where $r=r_i$, and the cell casing is considered rigid, reducing displacement to zero at the inner surface of the cell casing $(r=r_0)$. Additionally, since the layers in this analytic model share an interface, it follows that the radial stress and displacement at those interfaces are equal between layers L=1 and L+1 for L=1, ..., n-1, where n is the number of total layers in the model. This consideration is shown by Equation 77 and Equation 78 below.

$$\sigma_r^L = \sigma_r^{L+1}$$

Equation 77

$$u^L = u^{L+1}$$

Equation 78

This formulation results in a system of linear equations, which are solved for C_1 and C_2 at each layer for a given capacity. The pressure exerted by the jelly roll on the internal wall of the cell casing is calculated by solving for σ_r at $r=r_0$ at a given capacity. Since all material properties and thicknesses are assumed to be constant in this formulation, the pressure exerted by the jelly roll depends only on the eigen strain in the electrodes, which are calculated directly from the MOS measurements.

B.2: Preliminary Results from Analytical Model

Since repeatable stress data could not be collected from the electrodes, the analytical modeling effort was not fully utilized. The maximum stress ranges from the graphite anode and

NMC811 cathode, in combination with the mechanical properties listed in Table 14, predicted a hoop strain of 536 $\mu\epsilon$. As shown in Figure 58, this result is close to the maximum strain measured for an average cell.

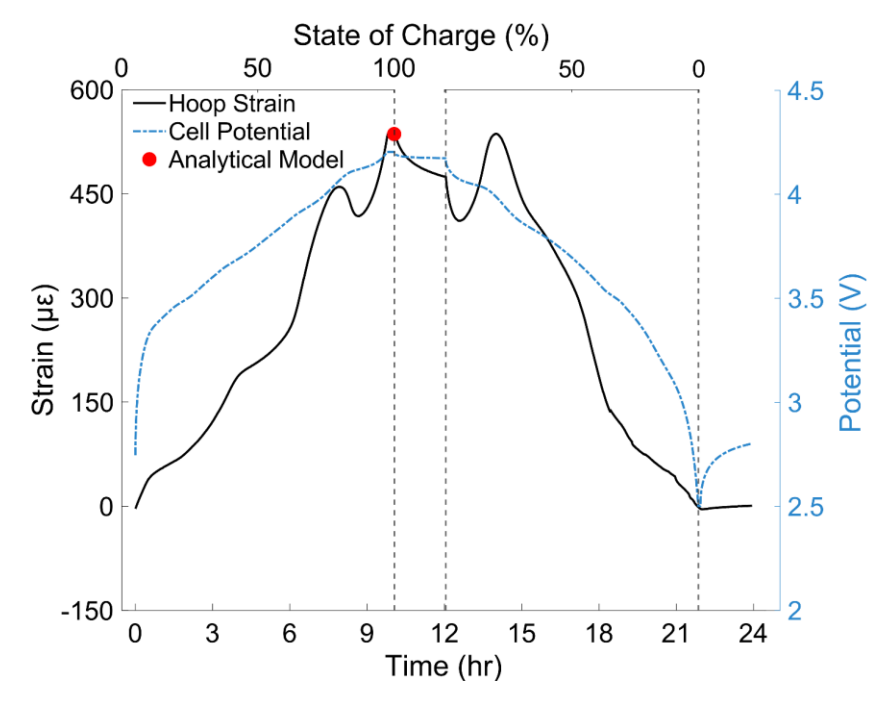


Figure 58: Strain and potential vs. time during a usual C/10 cycle showing that the analytical model could predict an accurate stress response with stress data.